

High Energy Emission from the Galactic Center

Andrea Goldwurm

*Université Paris Cité, CNRS, CEA,
Astroparticule et Cosmologie, F-75013 Paris,
France **

Maïca Clavel

*Université Grenoble Alpes, CNRS,
IPAG, 38000 Grenoble,
France*

Stefano Gabici and Régis Terrier

*Université Paris Cité, CNRS,
Astroparticule et Cosmologie, F-75013 Paris,
France*

(Dated: 15 Feb 2026; Accepted 19 Dec 2025 by Rev.Mod.Phys.; Exp. Vol.98 Iss.2 Apr-Jun 2026; doi:10.1103/9nww-fclb)

The center of the Galaxy is a prominent source in X-rays and gamma-rays. The study of its high-energy (HE) emission is crucial in understanding the physical phenomena taking place in this dense and extreme environment, where the closest supermassive black hole (SMBH) to us, Sgr A*, is lurking nearly invisible, today, in most of the energy spectrum. These phenomena are probably common to other galactic nuclei and may explain the feedback processes between nuclear regions and galaxies, so important for the overall evolution of the Universe. The Galactic center HE emission is very complex and consists of both thermal and non thermal radiation produced by compact and extended sources, surrounded by more diffuse components. All these objects and media are interacting with each other in the narrow and dense Central Molecular Zone (CMZ). Some of them also show relevant extensions towards the Galactic poles, indicating energetic outflows that seem to link the center to the recently observed large Galactic polar structures. In spite of the fundamental advances obtained in the last twenty five years with the most sensitive X-ray and gamma-ray observatories, several questions remain open to investigations. We review here the main observational results and the open issues on the high-energy diagnostics of the Galactic nuclear activity, focusing on processes that take place in the CMZ, and in particular discussing the role of the present and past SMBH activities in powering this region and possibly the whole Galaxy.

CONTENTS

I. The multi-wavelength view of the Galactic center	2	C. Hard X-rays and gamma-rays GC surveys	14
A. The center of our Galaxy	3	D. Recent and future instruments	14
B. The Galactic bar potential and matter inflow	4	III. Sgr A* and its close environment at high energies	15
C. The nuclear bulge: the CMZ and the NSD	4	A. Sgr A* quiescent emission and central hot plasma	15
1. Molecular material and diffuse thermal sources	4	1. Sgr A* quiescent emission and accretion flow	15
2. Non-thermal sources, magnetic field and outflows	6	2. Surrounding hot plasma and influence on the	
3. Massive star clusters and the nuclear stellar disc	6	accretion flow	16
D. The Nucleus: the Nuclear Star Cluster and Sgr A	7	B. Sgr A* flaring activity	17
1. The stellar content and the Young Nuclear		1. High-energy properties of Sgr A* flares	17
2. The Sagittarius A complex and the central cavity	7	2. NIR flares and multi-wavelength campaigns	18
E. The central 0.1 pc and Sagittarius A*	8	3. Constraints from multi-wavelength spectral	
1. The S-cluster and the G objects	8	analyses	19
2. Sagittarius A*, the Galactic black hole	9	4. Summary and possible origins of the events	20
3. Sgr A* black hole shadow and NIR emission	10	C. X-rays and hard X-rays from the central 20 pc	21
II. Searches for the High-Energy Emission from the GC	11	1. Discrete X-ray sources	21
A. Early X/gamma-ray observations	11	2. Sgr A East X-ray emission	21
B. X-ray telescope observations of the GC	12	3. The central hard X-ray sources	22
IV. X-ray source populations and discrete structures in the		IV. X-ray source populations and discrete structures in the	
CMZ		CMZ	23
A. The CMZ populations of point-like X-ray sources		A. The CMZ populations of point-like X-ray sources	23
1. Magnetic cataclysmic variables		1. Magnetic cataclysmic variables	23
2. Low mass X-ray binaries		2. Low mass X-ray binaries	24
3. More elusive pulsar populations		3. More elusive pulsar populations	24
B. Filaments and pulsar wind nebulae		B. Filaments and pulsar wind nebulae	25
C. Massive stars and star clusters		C. Massive stars and star clusters	26

* Also at CEA Paris-Saclay, IRFU/Département d'Astrophysique, 91191 Gif-sur-Yvette, France; andrea.goldwurm@cea.fr

V. Diffuse X-ray emission from the CMZ and beyond	26
A. The hard diffuse component: very hot plasma or unresolved point sources?	27
1. Populations of unresolved point sources	27
2. Constraints on the contribution from a hot plasma	27
B. The soft plasma component: hot plasma bubbles, loops and chimneys	28
1. A ring-like superbubble southwest of Sgr A*	29
2. The Radio Arc bubble	29
3. G359.41–0.12 and the Sgr C-chimney	29
4. The GC bipolar outflows	30
5. The X-ray chimneys	31
C. Non-thermal emission by molecular clouds: past activity of Sgr A*	32
1. Properties of the bright non-thermal emission	32
2. X-ray echoes and past activity of Sgr A*	34
3. Fading signals and constraints on what remains	36
D. Ionization and non-thermal emission from cosmic rays	36
1. A very large cosmic ray ionisation rate in the CMZ revealed by molecular lines	36
2. Problems with the interpretation of the ionisation rate measurements	38
3. Implications for high-energy observations: nuclear gamma-ray lines and 6.4 keV Fe K α line	38
VI. Gamma-ray emission and cosmic rays in CMZ and beyond	39
A. The central gamma-ray source	39
1. Observational results	39
2. Interpretation	41
B. GC HE and VHE gamma-ray discrete sources	43
1. G0.9+0.1 and its pulsar wind nebula	43
2. Radio Arc gamma-ray source	43
3. HESS J1745–303 and 4FGL J1745.8–3028e	44
C. Diffuse HE and VHE gamma-ray emission from the CMZ	45
1. An excess of multi-TeV cosmic rays in the CMZ	45
2. Origin of the diffuse emission: impulsive cosmic-ray source?	45
3. The morphology of the emission is best explained by a continuous cosmic-ray source at the GC	46
4. A cosmic-ray PeVatron at the GC?	47
5. What is the nature of the accelerator?	48
D. Gamma-ray emission from the Galactic bulge	49
1. The <i>Fermi</i> GeV excess	49
2. The 511 keV emission line	49
VII. Conclusions and perspectives	51
A. Summary and open questions	51
B. Future observations of the GC region	52
C. Link to the Galaxy: SMBH activity or Star Formation?	53
A. Abbreviations, acronyms and conventions	54
Acknowledgments	54
References	54

I. THE MULTI-WAVELENGTH VIEW OF THE GALACTIC CENTER

This review is dedicated to the high-energy emission from the Galactic Center and associated physical phenomena. For Galactic Center (GC), we consider here the sky area of about 2° radius centered on the compact source Sagittarius A* (Sgr A*), which is considered the electromagnetic counterpart of the Supermassive Black Hole (SMBH) located at the dynamical center of the Galaxy. For a distance of 8 kpc assumed throughout the paper (see § I.A), this region corresponds to the central volume of the Galaxy of about 300 pc radius (Fig. 1). For high-energy (HE) emission we mean electromagnetic radiation of photon energy larger than 0.1 keV. While the scope of the work is to present an observational view of the GC in this part of the spectrum, the related physical phenomena cannot be discussed without considering results obtained at other wavelengths. Therefore references to relevant measurements at low-energies, from radio to ultraviolet (UV) frequencies, will be mentioned all along the paper and more specifically in this introduction, where we present an overview of the region.

The GC appears very similar to the majority of the galactic nuclei (GN) in the Universe, in particular the local ones. Only about 10% of the GN are currently active and named for this as AGN, including different classes such as quasars, blazars and Seyfert galaxies. The bulk of AGN is located far away, in the past, and the weakest ones, most commonly found in nearby galaxies, are named low-luminosity AGN (Ho, 2008). In this respect, even if presently rather quiet compared to other GN, or even, probably, to other periods of the Galaxy history itself, overall the GC is the most dense, active and complex region of the Milky Way. It allows us to study peculiar phenomena and physical processes in condition rarely found elsewhere, except in objects far away. Being about 100 times closer than the nearest comparable GN and 10^5 times closer than the closest quasar, the region has been largely observed and studied at all wavelengths.

The SMBH at the very center of the region represents the closest specimen of such an extreme object, providing exquisite details on its properties, on its relation with its environment, and with the rest of the Galaxy. The set of very high precision infrared results on Sgr A* environment (see § I.E) makes it the best probe of the black hole solution of the Einstein's General Relativity (GR) theory, and has been rewarded with the Nobel prize of Physics in 2020 to Reinhard Genzel and Andrea Ghez (Genzel, 2021; Ghez, 2021), along with Roger Penrose for his theoretical contributions to the subject.

We now know that most, if not all GN contain SMBHs and that their interaction with the host bulges shapes and influences the evolution of the galaxies in the universe (Kormendy & Ho, 2013) even if the underlying processes and mechanisms are still not understood. Fi-

nally, as shown below, investigation of the GC features has provided evidence of past intense activity in the region, which can shed light on these feedback processes.

For all these reasons the GC is considered a real laboratory for the study of fundamental astrophysical processes and particularly for processes at work in GN, the most violent of which generally produce HE emission and can be studied through X and gamma-ray observations.

We will first provide a general description of the region, mainly based on non-HE measurements. This chapter (§ I) provides a general overview on an extended region around the GC, going from the Galactic disk to the very center of the Milky Way. It is based on previous reviews, in particular those by Genzel et al. (2010); Melia & Falcke (2001); Morris & Serabyn (1996) and the more recent ones by Bryant & Krabbe (2021); Ciurlo & Morris (2026); Henshaw et al. (2023); Morris (2022), to which we refer the reader for a more complete description and bibliography on the GC. Only a few of the most recent publications are cited here. In the following chapter (§ II) we describe the historical development of the HE observations of the GC and the characteristics of the observatories used to survey the region in the last 25 years, including current ones and mentioning those planned for the future. Then, the different components of the GC HE emission will be discussed: Sgr A* and the central 20-pc emission (§ III), the X-ray point-source populations and discrete thermal and non-thermal features (§ IV), the different components of the X-ray diffuse emission including the role of Cosmic Rays (CR, § V) and finally the gamma-ray emission (§ VI).

In the conclusions (§ VII) we present a finding chart of the GC structures and sources discussed in the previous sections, we recall the main established results and open questions and we list the perspectives for future observation programs based on new HE instruments. Finally, we mention the possible links between some of the HE GC components and their polar extensions, with the large Galactic polar structures of emission, the *Fermi* gamma-ray and *eROSITA* X-ray bubbles, that clearly indicate the presence of energetic outflows emanating from the central region of the Galaxy.

A. The center of our Galaxy

Our Galaxy is a barred spiral (Bbc - SBbc type), composed by a Galactic disk (GD), a central Galactic bulge (GB) and an extended halo. The thin GD has a radius of 13–15 kpc and scale height of few hundred parsecs. It contains a large fraction (0.6–0.7) of the stars of the Galaxy, which are estimated to be about $1\text{--}4 \times 10^{11}$ in total, for a mass of about $5 \times 10^{10} M_{\odot}$. It also includes most of the Galactic interstellar matter (ISM), estimated at 10–15% of the star mass, in the form of diffuse gas and dust. Stars, particularly the young ones,

and ISM show important concentrations along four main spiral arms surrounding the GD center. The Sun is in the close periphery of the disk, in the inner edge of the Orion-Cygnus (or Local) Arm, moving with a velocity of 220 km s^{-1} along a circular Galactic orbit with period of 210 Myr, at an estimated distance of 8 kpc from the Galaxy dynamical center¹. From Earth, the Galaxy is therefore seen edge-on and from inside the rotating GD, whose glowing in the sky produces the bright lane appearance of the Milky Way (MW).

Towards the disk center, a central peanut-shaped Bulge, mainly composed of old stars, sticks out from the Galactic plane, in the projected central $40^{\circ}\text{--}60^{\circ}$ of the MW, showing slight asymmetry, with a more prominent side towards positive longitudes. This view is actually due to a central stellar bar, composed by a fat ellipsoidal structure, stretching 2–5 kpc out from the center on both sides (Bryant & Krabbe, 2021, see also their Fig. 1 for a comprehensive view of the MW) seen from the Sun with a tilt of its major axis of $\approx 20\text{--}30^{\circ}$ from the line of sight (LoS) towards positive longitudes. The total bulge and bar stellar mass is estimated to be $2 \times 10^{10} M_{\odot}$. Even if these estimations and interpretations may still evolve with future surveys and refined modellings, it is clear that the bar is the main component of the observed GB and its gravitational potential dominates the stellar and ISM dynamics in the central regions. In fact its presence allows relevant inflow of matter from the GD to the center which otherwise will be hampered by the large angular momenta. An extended spherical halo containing very old stellar populations, globular clusters and dark matter (DM) envelops the disk and bulge. Including the halo, the total mass of the MW was recently revised by *Gaia* down to $2 \times 10^{11} M_{\odot}$ with a ratio of DM to baryonic mass of 3 (Jiao et al., 2023).

Since, from the Sun, the GC is seen through the whole GD, the dust of the ISM absorbs the radiation with an extinction of ≈ 30 mag in A_V which totally blocks visible and UV light. Thus, the GC region can only be observed from radio to infrared (IR) frequencies and again at HE. However the peculiar location of the GC was in-fact remarked already in the 1920s, well before radio, IR or HE astronomy developed, based on stellar distributions and motions. It remained not well positioned until the detection of the radio source Sgr A and its association in the 1950s–1960s with the GC, which also led to the redefinition of the Galactic coordinates, with the longitude $l = 0$ and latitude $b = 0$ now at $\approx 4'$ from Sgr A*.

¹ Current Sun-GC distance measures are in the range 7.9–8.2 kpc (Do et al., 2019a; GRAVITY Collaboration et al., 2019). We adopt here, for simplicity, the value of 8 kpc, which defines the scaling relation between measured angles in the sky and linear sizes at the GC throughout the paper: $1'' \approx 0.04 \text{ pc}$, $1' \approx 2.33 \text{ pc}$, $1^{\circ} \approx 140 \text{ pc}$.

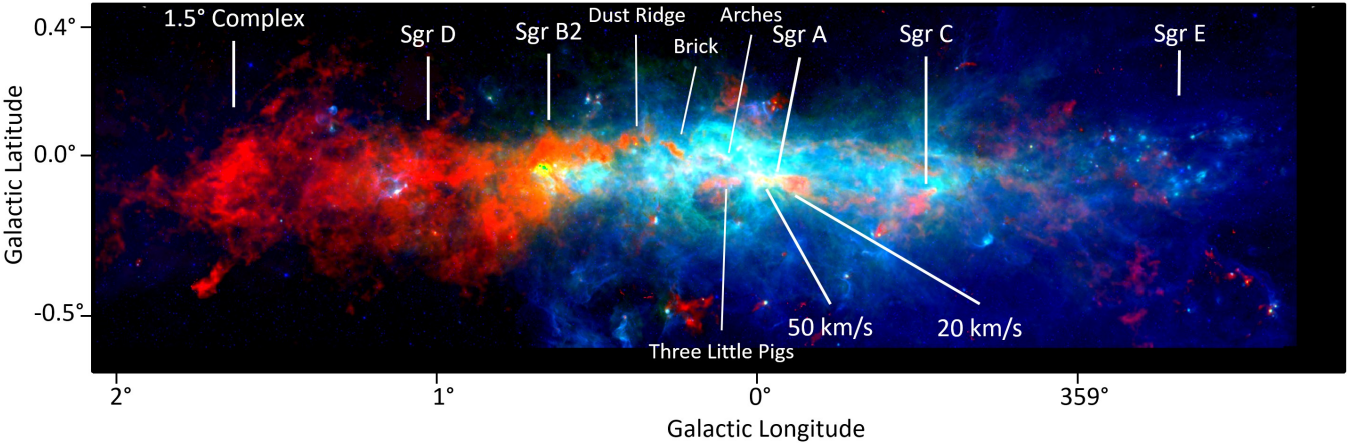


FIG. 1 The molecular and thermal content of the Central Molecular Zone of the Galaxy shown by the superposition of sub-mm to mid-IR (MIR) images: red and green show $350\ \mu\text{m}$ and $70\ \mu\text{m}$ emission (from *Herschel*) and blue shows $8\ \mu\text{m}$ emission (from *Spitzer*). The main molecular structures are indicated. Note the longitude asymmetry between sub-mm-emitting cool diffuse dust associated with the dense gas (red), mainly distributed at positive longitudes, and the MIR warm dust heated by recently formed high-mass stars (blue), at negative ones. Figure adapted from Battersby et al. (2025).

B. The Galactic bar potential and matter inflow

The MW spiral structure is interrupted inwards by the bulge, at a galactocentric radius R of about 3 kpc (20°).

The ISM distribution shows a density increase from the outskirts of the GD toward the center and reaches a maximum at $R \approx 4$ kpc, forming the so called 4-kpc molecular ring. For smaller galactocentric distances the gas density decreases rapidly to low values creating the region of ISM avoidance (3–1.5 kpc) where the stellar bar potential does not allow for stable orbits. The tri-axial bar potential indeed forces matter to follow the so-called x1 and x2 closed orbits which are related to the specific resonance points of the underlying potential (see also Fig. 2). The x1 are nested, very elliptical orbits around the bar major axis while the x2 are more oval trajectories aligned to the bar minor axis perpendicular to and within the x1 orbits. The x2 orbit sizes are somehow linked to the potential orbital resonances and even though what determines their actual dimensions is still under intense study, they broadly seem to correspond to the rings of the central molecular zone. The accepted picture is that ISM of the GD inner edge is rapidly set into x1 orbits closer and closer to the bar axis, get shocked at the cusps of the inner orbits (where the trajectories intersect) and is funnelled inwards along the very inner, nearly radial, x1 orbits, forming the so-called bar (or dust) lanes, reaching the outer x2 orbits. Shocks lead to the setting of material on the x2 orbits, allowing the inflow of matter from the disk to reach this central region (Fig. 2, left). Data and simulations show that, considering loss processes, about $0.2\text{--}1.4\ M_\odot\ \text{yr}^{-1}$ of matter is conveyed in this way from the GD edge to the GC through the bar lanes (Bryant & Krabbe, 2021; Henshaw et al., 2023; Su et al., 2024).

This overall picture accounts for most of the non-circular gas kinematic features observed in the radial velocity – longitude ($V_R - l$) diagrams of molecular lines like those of the CO within 20° from the center, it does not require the presence of expanding rings to explain these non-circular motions, and it is now an accepted model, even if various items are still object of intense research.

The region delimited by the x2 orbits ($R < 300$ pc) contains the Nuclear Bulge (NB), made of the Nuclear Stellar Disc (NSD) and its inner Nuclear Stellar Cluster (NSC), and the Central Molecular Zone (CMZ) of ISM.

C. The nuclear bulge: the CMZ and the NSD

1. Molecular material and diffuse thermal sources

The Central Molecular Zone (Bryant & Krabbe, 2021; Henshaw et al., 2023; Morris & Serabyn, 1996) is the $4^\circ \times 2^\circ$ narrow strip of the sky, corresponding to the central $600\ \text{pc} \times 300\ \text{pc}$ region which contains the large reservoir of ISM in the form of neutral, mostly molecular, and ionized gas, along with the associated dust, that can be observed at different wavelengths from radio to MIR (Fig. 1). In the CMZ clouds the average density ($\approx 10^{3\text{--}4}\ \text{cm}^{-3}$) is up to two orders of magnitude above the one observed in molecular clouds (MC) of the GD (Bryant & Krabbe, 2021). Temperatures are also higher ($\gtrsim 40\ \text{K}$ compared with the typical $< 20\ \text{K}$ in the GD MC), as well as the turbulence and the magnetic pressure. The total mass of molecular gas amounts to $\approx 2\text{--}6 \times 10^7\ M_\odot$ (Battersby et al., 2025; Henshaw et al., 2023), i.e. 3–10% of the total molecular content of the Galaxy, and appears organized in structures distributed around the nucleus. An inner, low velocity ($< 100\ \text{km s}^{-1}$),

component of these structures is located within 100 pc from the center, is composed by the denser clouds and represents the dominant part of the CMZ mass, the so-called 100-pc molecular ring. As shown in Fig. 1 the overall matter distribution appears asymmetric with a large fraction (from three quarters to two thirds) of gas material at positive Galactic longitudes while the indicators of star formations, specifically the tracers of massive young stars and compact H II regions, appear concentrated to negative longitudes.

Given our vantage point and the lack of LoS distance indicators, the actual 3D spatial distribution and dynamics of the gas within the CMZ are however unknown. Several models, supported by various observations, simulations and theoretical studies, have been proposed (Fig. 2, right): from spiral arms around the nucleus (Sofue, 1995) to a twisted, elongated closed ring not centered on Sgr A* (Molinari et al., 2011) and to gas streams following open orbits (Kruijssen et al., 2015). Large observational efforts (Yan et al., 2017), including recent comprehensive work combining IR data from *Herschel* and *Spitzer* and 3D modelling (Battersby et al., 2025) and the ALMA CMZ Exploratory Survey program (Sofue et al., 2025), have not allowed yet to identify the most realistic of these pictures (e.g., Lipman et al., 2025; Walker et al., 2025).

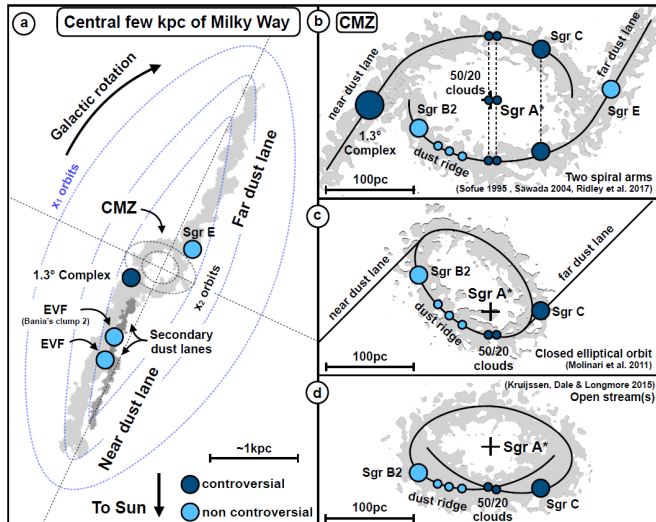


FIG. 2 Top view sketches of the matter inflow along the x_1 and x_2 orbits of the stellar bar potential (left) and of the different models of molecular matter distribution in the CMZ (right), with controversial locations of individual MCs (from Henshaw et al., 2023).

Within the large structures the gas is highly non-uniform and the densest concentrations form the Giant Molecular Clouds (GMC), with densities that can reach 10^{5-6} cm^{-3} , temperatures 70–100 K, large inner velocities and enhanced turbulence, and which are threaded by strong ($\approx \text{mG}$) magnetic fields. The main GMCs of the CMZ, for density and volume, are the complexes corre-

sponding to the bright extended radio sources known as Sgr A, Sgr B2, Sgr C, Sgr D, and Sgr E (Fig. 1, 3), even if some are actually composed of several clumps, close in projection but possibly at different LoS distances because they display different V_R .

The most massive cloud, Sgr B2, contains $\approx 0.5-1 \times 10^7 M_\odot$, roughly 10% of the CMZ gas, and is one of the most massive star-forming clouds in the entire Galaxy. Located at $l \approx 0.66^\circ$ (100 pc in projection) from Sgr A*, in the northern part of the large Sgr B complex which also includes the bright H II region Sgr B1 in the south, Sgr B2 is a luminous radio and IR source. It is composed of an extended envelope ($n_{H_2} = 10^4 \text{ cm}^{-3}$, 20-pc radius) and an inner high density cloud ($n_{H_2} = 10^{5-6} \text{ cm}^{-3}$, 5-pc radius), which contains sites of massive star formation, with ultra-compact H II regions, proto-stars and molecular masers. Using masers, the LoS position of Sgr B2 was estimated to be about 130 pc in front of the sky plane defined by Sgr A* but this estimate relies on kinematic assumptions. Sgr C is instead located on the Galactic west side of the GC (Fig. 1) also at about 100 pc in projection from Sgr A* and, even if considerably less massive ($\approx 5 \times 10^5 M_\odot$) than Sgr B2, it is a site of intense star formation. Extended over 40 pc and composed by several clumps, possibly not all physically connected, its structure is complex, presenting other superposed diffuse sources: a SNR that seems interacting with the molecular material, an H II region and structures of hot gas extending north, the Sgr C Chimney. Further out at negative longitudes the GMC Sgr E extends from $l \approx -1^\circ$ to -1.4° and hosts a substantial number of compact H II regions and other star formation indicators. Its large negative radial velocities indicate that it is approaching and is probably located at the interaction point of the far dust lane with the CMZ rings of the external x_2 orbits. In a nearly symmetric position to the center, at $l \approx 1.2^\circ$, is located another GMC, Sgr D, which also presents a complex structure including a very bright H II region, a radio-bright shell SNR more to the south, and another SNR detected in X-rays, all these superposed to extended radio line emission of the cloud molecular material that appears receding at $50-70 \text{ km s}^{-1}$. Further out there is the large $l=1.5^\circ$ -complex (or 1.3° -complex) showing extreme velocity features in the $V_R - l$ diagram, which is probably out of the 100-pc ring and linked to either the x_2 orbit, the bar lane or their intersection. The central Sgr A radio complex is a highly composite source, including the GMC M-0.02-0.07 (also known as the 50 km s^{-1} cloud) and M-0.13-0.08 (the 20 km s^{-1} cloud), located east and south, respectively, of the Sgr A core, which also contains a massive molecular nuclear disk (see § I.D.2).

In addition to the massive complexes, other smaller features, filaments and medium-size clumps of molecular gas are present in the CMZ, in particular between Sgr A and Sgr B (Battersby et al., 2025, Fig. 1 and 18). Within $4'$ and $14'$ on the Galactic East from Sgr A*, roughly be-

tween the 50 km s^{-1} cloud and the Radio Arc, lies a set of clouds, which we refer to as the Sgr A molecular complex (to avoid confusion with Sgr A). This region includes important features that are known under different names in the literature. It is the case of G0.068–0.075 (the Stone) and G0.106–0.082 (the Sticks), two of the MC set known as the Three Little Pigs, that we will refer to as the Bridge in this review, as well as of the MC G0.11–0.11, just south of the Bridge. The Sgr A molecular complex has been studied in great detail due to its bright variable non-thermal X-ray emission (§ V). Another set, not visible in X-rays, includes the very dense IR-dark Brick cloud and the clumps of the Dust Ridge between the Brick and Sgr B2, which are thought to trace part of the 100 pc ring. As already remarked, if the MC 2D distribution on the sky and radial velocity are well known, their 3D distribution and actual motion are not (Fig. 2).

A diffuse, warm ($T \approx 200 \text{ K}$) molecular gas of low density ($\approx 50 \text{ cm}^{-3}$) permeating the CMZ with high volume filling factor, was put in evidence at the end of the 1990s by near-infrared (NIR) observations of the H_3^+ lines in the GC (see § V.D). This component appears not-rotating but rather expanding radially and represents a low fraction of the CMZ molecular content.

2. Non-thermal sources, magnetic field and outflows

In addition to neutral and ionized gas, traced by the thermal features, the CMZ contains a remarkable number of non-thermal radio sources as shown by the extraordinary MeerKAT composite GC images (Heywood et al., 2022, Fig. 3). These are either shell supernova remnants (SNRs), pulsar wind nebulae (PWNe) or radio non-thermal filaments (NTFs). They demonstrate the importance of star formation (SF) in the region and the presence of magnetic fields (Morris, 2015) and particle acceleration processes. The most spectacular feature is the Radio Arc located at about 30–50 pc on the Galactic East from Sgr A* and extending over about 50–100 pc nearly perpendicularly to the Galactic plane and over about 10 pc in latitude. It is composed by tens of nearly aligned bright arched and narrow filaments with non-thermal spectra which are produced by synchrotron emission of relativistic electrons in a poloidal magnetic field. Several hundreds other NTF have now been identified in the GC, in particular with MeerKAT (Yusef-Zadeh et al., 2022). The brightest and longest of them are also generally oriented towards the Galactic poles, demonstrating that, out of the GMC and particularly above the plane, the GC magnetic field lines are overall poloidal (but see Yusef-Zadeh et al., 2023, for the orientation of the short filaments).

Within the intermediate-density clouds of the CMZ, instead, field lines appear, from IR polarization measure-

ments of warm dust, largely toroidal and seem to remain so also in the inter-cloud regions close to the plane, which prompted a modelling where the overall GC vertical magnetic field is dragged into a planar configuration by the shear of the 100-pc ring gas circular motion (Morris, 2015). This scenario is also supported by the recent results from the large CMZ FIR survey provided by SOFIA (Paré et al., 2025), that confirm the presence of a pervasive vertical magnetic field also outside the NTFs and fields lines aligned with the density structures in the dense MCs.

The field strength was estimated at a few mGauss for the Radio Arc and in several other locations, but lower values ($100\text{--}400 \mu\text{G}$) have been derived recently using MeerKAT data of detected NTFs (Yusef-Zadeh et al., 2022). The overall field strength is still controversial with estimates that range from $10\text{--}50 \mu\text{G}$ to few mG (Crocker et al., 2010; Morris, 2015), but, despite the lack of consensus, it is clear that the GC magnetic field is stronger than in the GD and it plays an important role in the dynamics and physical processes in the CMZ.

Other large-scale features and bubbles in radio/IR, extending above and below the Galactic plane, probably produced by large outflows and outbursts, demonstrate the extraordinary activity of the region (see § V.B).

3. Massive star clusters and the nuclear stellar disc

The large quantity of gas in the CMZ implies a large star formation rate (SFR). The GC SFR, estimated roughly constant and equal to $0.07^{+0.08}_{-0.02} \text{ M}_\odot \text{ yr}^{-1}$ over the last 5 Myr (Henshaw et al., 2023), is much smaller than that in the GD, in terms of per unit of mass, but is very large if one considers the very small volume within which it has been estimated. The low SFR per unit of mass is probably connected to the large turbulence and other dynamical phenomena of the region, or even to the large CR pressure and ionization. Indeed, as mentioned above, some of the GMCs host on-going intense star formation sites (Sgr B2, Sgr A, Sgr C, also associated to young H II regions) while others do not (Sgr B1, the Brick, 1.5° -complex).

The GC contains three prominent young star clusters, amongst the most massive of the MW: the Arches, the Quintuplet and the Young Nuclear Cluster surrounding the GC nucleus. The Arches is located 26 pc East of Sgr A* in projection, with a stellar mass of $\approx 10^4 \text{ M}_\odot$ concentrated within a radius of 1 pc. It is mostly composed of massive Wolf-Rayet (WR) and O stars with ages between 2.5 and 3.5 Myr, which excite the gas thermal emission observed in the nearby radio-bright Arched filaments. The Quintuplet cluster is at 30 pc in projection from Sgr A*, east of the Arches and is surrounded by the nearby thermal Sickle filament which it likely powers. Of similar mass and dimension than the Arches,

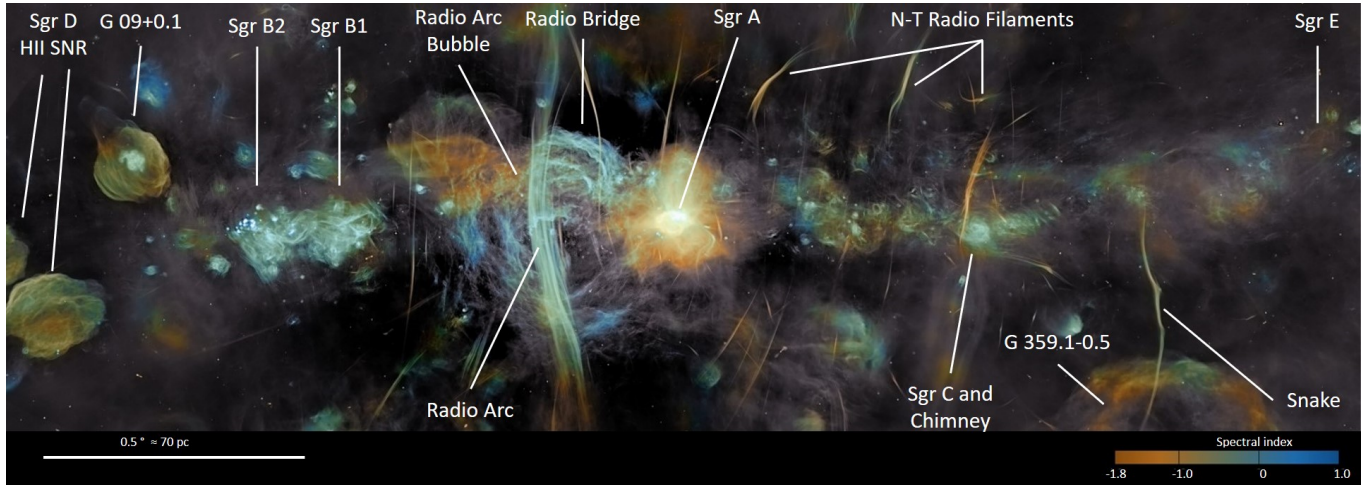


FIG. 3 MeerKAT radio composite image of the GC in Galactic coordinates, showing both the thermal and non-thermal radio sources of the CMZ, with the color code giving the power-law spectral index. Figure adapted from Heywood et al. (2022), original image credit I. Heywood, SARA; color processing J.C. Muñoz-Mateos, ESO.

it appears slightly older (4–5 Myr), making it unclear whether the two clusters were born from the same formation event or not. However, they probably evolved from similar scenarios, caused by gas over-density regions at the intersections of x_1 and x_2 orbits. The overall stellar content corresponding to the CMZ region is the so-called Nuclear Stellar Disk (NSD), a high-density stellar structure clearly connected to, but different from, the central part of the Galactic bulge/bar, and which forms an axis-symmetric rotating disk, of radius ≈ 230 pc and scale height ≈ 45 pc, made of old (10 Gyr) and middle-aged (1 Gyr) stars probably born in the dense environment of the CMZ. Stars rotate in the same direction as the MW, their density increases towards the center, making a total mass of the NSD of $10^9 M_\odot$, which dominates the gravitational potential for $R \approx 30$ –300 pc.

D. The Nucleus: the Nuclear Star Cluster and Sgr A

1. The stellar content and the Young Nuclear Cluster

Within the inner $R = 30$ pc (12.5') and down to about 1–3 pc from where the SMBH dominates, the gravitational potential is driven by another stellar component, the Nuclear Stellar Cluster (NSC). Discovered at the end of the 1960s as a central prominent emission in IR, the NSC is a very dense and massive star cluster, quite similar to those observed in the centers of other spiral galaxies. The NSC is more spherical than the NSD, it is very dense and compact, with a huge central stellar density of $10^{6-7} M_\odot \text{ pc}^{-3}$ in the core, and an effective radius of 5 pc. It contains $\approx 3 \times 10^7 M_\odot$ of stars mainly cold, old and of middle age (> 5 Gyr). Stellar density increases towards the center and recent studies have shown that the derived 3D density profile within the influence radius

of the SMBH nearly matches the predicted distribution expected for a relaxed star cluster with a central BH. This cusp has been searched for several years and seems now a well established feature of the NSC.

In addition to the NSC old stars, the central parsec ($R < 0.5$ pc, 12.5'') contains a remarkable cluster of about 100–200 luminous, hot, early-type stars of ages 2–8 Myr, of total mass $10^4 M_\odot$: the Young Nuclear Cluster (YNC). Mostly composed by post-main sequence blue O/B giant, super-giant, main sequence and WR stars, the majority of these stars have orbital motion opposite to the MW and to the underlying NSC stars. A significant fraction of them (20–30%) shows a pattern of clockwise rotation and appears to lay in a rotating disk, between 1'' and 5'' (0.04–0.2 pc) from Sgr A*. The most striking concentrations of such stars were identified initially as individual IR sources: IRS16, IRS13 and IRS7. The YNC hot stars produce $2 \times 10^7 L_\odot$ of UV radiation which ionizes the gas of the central pc creating the central thermal source, Sgr A West, and heating the dust. The ≈ 30 massive post-main-sequence WR or helium emission-line stars of the cluster are also powerful emitters of stellar winds, with typical mass losses of 10^{-5} – $10^{-4} M_\odot \text{ yr}^{-1}$ and terminal velocities of 500–2000 km s $^{-1}$. Their collective momentum and radiation pressure clear the gas out of the region, likely creating the central cavity.

2. The Sagittarius A complex and the central cavity

The ISM component within the central $R = 15$ pc (6.3'), spatially superposed upon, and interacting with, the stellar content described above, is the Sgr A radio and molecular complex. Ferrière (2012, recently updated by Bryant & Krabbe, 2021) reviewed the wealth of published data on Sgr A, and provided a detailed descrip-

tion of its structure and properties, with a global picture presently largely accepted, apart from the location of the two GMC of the complex. In this picture, the external belt of GMC that, in projection, surrounds Sgr A core on the East (50 km s⁻¹ cloud) and South (20 km s⁻¹ cloud, see also Fig. 1) are part of the complex, the first one slightly behind and the other in front of Sgr A*. However, in other CMZ matter distribution models these two clouds are sometimes far away from Sgr A* and part of the CMZ 100-pc ring (Fig. 2). Their masses are both of $2 \times 10^5 M_{\odot}$, with densities of $2 \times 10^4 \text{ cm}^{-3}$ and temperatures around 60 K. Other molecular streams and ridges are seen to extend from the GMCs toward the inner region connecting them to, and probably feeding, the Circum-Nuclear Disk (CND) or Ring, an asymmetrical, clumpy, annular structure of very dense molecular gas and dust within $\approx 1.2\text{--}5$ pc from the center, with a total mass about one order of magnitude lower than those of the close-by GMC, from recent estimates, and rotating rapidly, at ≈ 100 km s⁻¹, around Sgr A* (Fig. 4).

Superposed, in projection, on part of the molecular structures is Sgr A East, a distinct non-thermal radio source composed of a halo of diffuse emission with a triangular shape and an inner oval shell ($3' \times 4'$, or 7 pc \times 9 pc) centered about 50" (2 pc) east of Sgr A* (Fig. 12, left). Sgr A East is also bright in X-rays and is considered a mixed-morphology SNR where the observed radio synchrotron shell of the external shock sweeps out the inner cavity which contains hot ionized gas from both stellar ejecta and shocked ISM.

Within the CND ($R < 1.5$ pc) there is a central cavity, of much lower neutral gas density, carved by the powerful stellar winds of the YNC, (but see Blank et al., 2016, for the effect of stellar winds on the CND) and which hosts the H II region Sgr A West, a thermal nebula ionized by the UV radiation of the young stars, especially those of the IRS16 concentration. The dense part of the ionized gas takes the form of a mini-spiral composed of three arms and a bar (Fig. 4), also rotating around the SMBH. Part of the arms, particularly the western one, join the inner side of the CND ring, and show similar circular movement, while the east and north arms show inward motion towards the bar and the center of the cavity. The contrasting processes of the SN event and the SMBH mass accretion certainly play a role in shaping the inner 20 pc of the MW (Ferrière, 2012), and an overall picture on how matter inflow takes place has now emerged from the data (Bryant & Krabbe, 2021). The inflow from the GMC of the CMZ into the CND seems mediated by the molecular streamers and then, through the mini-spiral and central cavity, the material is conveyed to the very center of the NSC, giving rise, in spite of the tidal stresses of the SMBH, to episodic in-situ formation of stars, explaining the presence of the YNC in the central parsec.

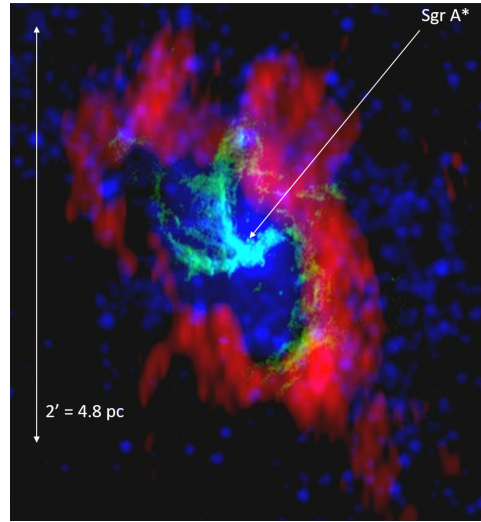


FIG. 4 The molecular CND and the Sgr A West mini-spiral of ionized gas shown by a composite image of the 3.4 mm HCN line emission (red, BIMA) and the 3.6 cm radio continuum (green, VLA) from warm ionized gas, along with the star's IR emission (blue, *Spitzer*). The image is in equatorial projection centered on Sgr A* (indicated by a white arrow) with North to the top, East to the left and scale given by the double-sided arrow. From NRAO archives (<https://www.nrao.edu/archives/items/show/33428>).

E. The central 0.1 pc and Sagittarius A*

The central parsec of the Galactic Nucleus is dynamically fully dominated by the SMBH since the NSC enclosed mass is lower than the SMBH mass already at $R = 3$ pc (1.25'). Deep inside the YNC inner disk all objects move at extreme velocities apart from one single point-like source that appears totally steady: Sgr A*.

1. The S-cluster and the G objects

At distances $R < 1''$ (0.04 pc), there is another different group of young stars: the central, or S, or Sgr A* cluster, composed of at least 50 main sequence dwarf B stars, less massive ($8\text{--}20 M_{\odot}$) and not as young (< 15 Myr) as the O/WR ones seen further out. The S stars show elliptical orbits around the same focus but distributed isotropically, therefore indicating a different formation process than the YNC, without the intervention of a disk. These few tens of stars, have allowed the most precise estimations of the parameters of the SMBH. Indeed, over the last 30 years, NIR high-resolution observations conducted at the NTT, VLTI and Keck telescopes with an increasingly sophisticated instrumentation, culminated with the upgraded Keck/NIRC2 and VLTI/GRAVITY instruments, have led to extremely precise measurements of their orbit parameters (Do et al., 2019a; Genzel et al., 2010; GRAVITY Collaboration et al., 2022). In particu-

lar, one of the brightest stars of the S-cluster, S2 or S0-2, could be followed twice over its entire 16-yr orbit and particularly at its periapse passages, in 2002 and 2018, when it transited with a velocity excursion of 8000 km s^{-1} at only 120 AU from the SMBH. The exceptional data of the S2 proper motion have not only led to the determination of the mass and distance of the SMBH but also revealed clear GR effects.

Such NIR observations in the central 0.1 pc have also revealed the presence of several objects of gas/dust appearance showing rapid movement along elliptic Keplerian orbits around the SMBH. The first and most famous one is the G2 object, detected in 2012 (Gillessen et al., 2012), that was first interpreted as a $10^{-3} M_{\odot}$ compact ionized gas clump and which passed at periastron in 2013, showing clear tidal effects on its structure, even if not a total disruption (Gillessen et al., 2013). After this first discovery several other G objects have been identified and are now regularly monitored (Ciruló et al., 2020). The presence of such a population of dusty objects in the same region of the S-cluster has further challenged the pure dust interpretation, as the hypothesis of young low-mass stars with distended gaseous-dusty envelopes or even binary systems seem also compatible with the data.

2. Sagittarius A*, the Galactic black hole

At the very center of Sgr A West is located the remarkable source Sgr A* (Fig. 4, see e.g. Melia & Falcke, 2001; Morris, 2022, and references therein) detected from about 0.5 m wavelength to hard X-rays, apart from the $1 \mu\text{m}$ to 1 nm range affected by extinction. Discovered 50 years ago (Balick & Brown, 1974), as a distinct point-like component of Sgr A, this bright, compact, variable and non-thermal radio source was quickly associated to the putative SMBH of the Galaxy predicted by Lynden-Bell & Rees (1971) just few years before. The inverted non-thermal radio spectrum did not quite resemble the spectra of quasars and the luminosity was rather low, but it pointed to a compact object of large brightness without prominent counterpart at the very center of the MW.

Proper motion measurements of the source over 18 yr with VLBA found no intrinsic motion down to $< 1 \text{ km s}^{-1}$ (Reid & Brunthaler, 2020). In the inner region where everything moves very fast, this allows, under reasonable assumptions, to set severe lower limits on its mass. However the best parameters of the source are given by the NIR measurements of the motion of the S-cluster stars. In fact the location of Sgr A* is fully compatible, within 1 mas (8 AU), with the location of the focus of their orbits and the source is identified with the object that drives the star motions. The estimated enclosed mass, within the S2 periapse distance, is of $(4.1 \pm 0.1) \times 10^6 M_{\odot}$ at a distance of $8.1 \pm 0.1 \text{ kpc}$, where, following Morris (2022), these values (and errors)

are actually the average (and range) between the Keck and VLTI results that differs by 5 and 2.5% in mass and distance, respectively. Such a large mass compressed in such a small volume implies a minimum density of $5 \times 10^{15} M_{\odot} \text{ pc}^{-3}$ and cannot be stable for long, it must collapse into a SMBH (see Genzel et al., 2010, for discussion on alternative models). The gravitational redshift (Do et al., 2019a; GRAVITY Collaboration et al., 2018a) and the Schwarzschild precession of the S2 orbit (GRAVITY Collaboration et al., 2020b) have already been detected in particular by GRAVITY, while higher-order GR effects, like the Lense-Thirring one which may provide information on the BH spin, need the detection of closer (and fainter) stars with future instrumentation.

Such a SMBH has a Schwarzschild radius $R_S = 1.2 \times 10^{12} \text{ cm}$, an Eddington Luminosity of $L_E = 5 \times 10^{44} \text{ erg s}^{-1}$, and it is expected to accrete any stellar or gaseous object that would venture too close to its horizon, such as a fraction of the stellar-wind gas of the YNC. The accretion process in Sgr A* should produce a large amount of radiation while the source is clearly underluminous all over the electromagnetic spectrum. From observations and detailed simulations the accretion rate from the stellar wind is estimated at $10^{-6}\text{--}10^{-5} M_{\odot} \text{ yr}^{-1}$ (Baganoff et al., 2003; Quataert, 2002) at a Bondi radius of $\approx 0.12\text{--}0.2 \text{ pc}$ ($3''\text{--}5''$) giving a significant accretion power of $L_A \approx 3 \times 10^{39\text{--}40} \text{ erg s}^{-1}$ (assuming an efficiency of 10%), with important variations induced by wind clumps, turbulence and shocks (see Calderón et al., 2025, 2020, for the latest studies). The radio and sub-mm Sgr A* fluxes (of about 1 Jy) translate into a total luminosity of less than $10^{36} \text{ erg s}^{-1}$, some 10^{-9} less than the L_E and 10^{-4} less than the estimated L_A from stellar winds. In the quiescent state, the radio to sub-mm spectrum is described by a power law with a positive index of $4/3$ (in νF_{ν}) with a sub-mm bump that peaks at $350 \mu\text{m}$. It is consistent with a self-absorbed thermal synchrotron emission of electrons at temperatures $\approx 10^{11} \text{ K}$, with densities of the order of 10^6 cm^{-3} , in a magnetic field of $10\text{--}50 \text{ G}$ (Falcke & Markoff, 2000; Yuan et al., 2002). It becomes optically thin above $\approx 100\text{--}300 \text{ GHz}$ and then decreases steeply, becoming undetectable in the far-mid IR regimes where diffuse dust emission completely dominates measurements.

The quiescent Sgr A* spectral energy distribution (SED) is represented in Fig. 5 and it was modeled with advection dominated accretion flow (ADAF) or radiatively inefficient accretion flow (RIAF) models, the latter ones including outflows or convection in addition to advection. They predict three peaks of emission: the inner thermal synchrotron one mentioned above, an undetected inverse Compton bump in the optical/UV range and a thermal bremsstrahlung emission in X-rays from the hot electrons of the entire flow. The ADAF/RIAF models (see Narayan & Quataert, 2023; Yuan & Narayan, 2014, and references therein) were developed in the 1990s

when it appeared clear that, at low accretion rates, the matter falling into BHs does not behave as predicted by the standard optically thick and geometrically thin disks of Shakura & Sunyaev (1973), but rather sets in a two temperature flow with ions and electron thermally decoupled (with ions much hotter than electrons). Subsequent GR magneto-hydrodynamic (MHD) simulations have confirmed these semi-analytical models but also revealed a large complexity of situations. In particular, outflows may play a major role and solutions depend whether the magnetic energy is dominant over the gas pressure, giving rise to the so-called Magnetically Arrested Disk (MAD) models, or not, as in Standard and Normal Evolution (SANE) models (see EHT Collaboration et al., 2022c; Narayan & Quataert, 2023, for definitions, reviews and references). Most GRMHD simulations also predict, in certain cases, the emergence of collimated relativistic jets. Jet models, first proposed by Falcke & Markoff (2000) and Markoff et al. (2001), for which the base of the jet gives rise to the sub-mm bump and its extension to the low-frequency spectrum, are still compatible with the data. Indeed, at cm wavelengths the spectrum sticks out with flatter slope compared to the extension of the sub-mm bump (Fig. 5). It seems dominated by an external non-thermal component, possibly a dark jet that displays most of its power in kinetic, rather than radiative, energy.

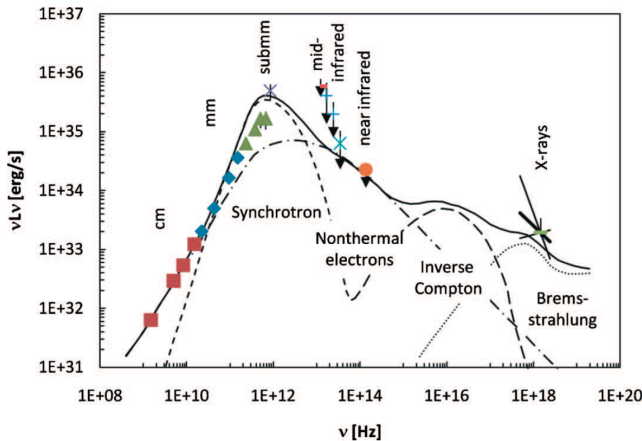


FIG. 5 Sketch of the SED of the Sgr A* quiescent emission, from Genzel et al. (2010). Compiled data in different bands are fitted with a RIAF model (broken and dotted lines), plus a non-thermal electron component (broken-dotted line) (Yuan et al., 2003). For the most recent and complete Sgr A* SED data compilation see EHT Collaboration et al. (2022b).

In addition the effective accretion rate reaching the BH horizon has been estimated to be only 10^{-9} – $10^{-7} M_{\odot} \text{ yr}^{-1}$ through measurements of linear polarization of Sgr A* millimeter emission, which implies limits on the Faraday depolarization and therefore on the plasma density around the source (Aitken et al., 2000; Marrone et al., 2007). Such a low accretion rate implies

somehow that the stellar-wind material captured at the Bondi radius does not reach the horizon and it is rather stored in the system or expelled in outflows.

3. Sgr A* black hole shadow and NIR emission

Since the high-frequency radio/sub-mm emission must come from the very inner region close to the BH horizon, VLBI measurements have been performed during the last decades (at increasingly higher radio frequencies where interstellar scattering is lower) to determine the size of Sgr A*. These observations have recently led to the detection of the BH shadow with the Event Horizon Telescope (EHT). This world global interferometric array of radio-telescopes capable to attain resolutions of the order of tens of μas , performed, in 2017, accurate measurements of Sgr A* at $\lambda = 1.3 \text{ mm}$, and resolved the compact source emission in a thick ring of $51.8 \pm 2.3 \mu\text{as}$ diameter (0.42 AU) with a distinct central depression, providing, for the first time, a reconstructed image of the SMBH shadow (see EHT Collaboration et al., 2022a,b, and ref. therein). These results are consistent with the GR predictions of the appearance of a Kerr BH at the GC, with the estimated mass of Sgr A* and a prograde accretion disk viewed at low inclination ($i < 50^\circ$). The BH derived parameters are fully compatible with the averages of the NIR measurements of the S-star orbits without being able to resolve the inconsistencies between the Keck and the VLT measurements.

Sgr A* has been detected as a flaring source of NIR light (Genzel et al., 2003) soon after the discovery of Sgr A* X-ray flares (§ III). The wealth of observations conducted since then show that Sgr A* NIR emission is continuously varying but likely presents two states: a quiescent one characterized by red-noise variability described by a log-normal process with a well-defined median flux density of $1.1 \pm 0.3 \text{ mJy}$, and a flaring state produced by sporadic flares that create the observed power-law extension of the flux distribution (Dodds-Eden et al., 2011; GRAVITY Collaboration et al., 2020a), even though a single, but right-skewed or broken, distribution can fit the data (Witzel et al., 2018, 2021). A larger flaring activity, in 2019 after the pericenter passage of both S2 and G2 was reported with Keck (Do et al., 2019b) and VLT/GRAVITY (GRAVITY Collaboration et al., 2020a) but without changes in persistent emission. The NIR flares are more frequent (3–4 per day) than X-ray ones, show variabilities on minute scales, present steep (red) power-law energy spectra and are linearly polarized, pointing to thin synchrotron emission of transiently accelerated electrons very close to the BH. Spectral changes (flares redder when dim, e.g. during rise and fall) were detected with the VLT, confirmed recently with Keck and recently measured during a bright NIR flare observed with VLT/GRAVITY and *Spitzer* in 2019. A

quasi-periodicity in the light-curve of the first detected flare in 2003 was not confirmed by later flare observations, but in 2018 VLTI/GRAVITY could measure the movement of a flare emission centroid, showing that it follows a nearly circular clockwise orbit with a period of ≈ 40 min and displaying polarimetric properties varying with a similar periodicity (GRAVITY Collaboration et al., 2023, 2018b). The data are interpreted as emission from a hot spot moving in an accretion disk at a distance of $3\text{--}5 R_S$ from the black hole, viewed at low inclination angle (nearly face on), with a period of 33–65 min, i.e., close to the innermost stable circular orbit period of a non-rotating $4 \times 10^6 M_\odot$ BH. The derived flare orbit orientations are close to the one of the YNC clockwise stellar disk, suggesting the accretion flow is fueled by their winds, in agreement with recent simulations (Ressler et al., 2020). A deepest analysis of the EHT ALMA observation of Sgr A*, performed after a prominent X-ray flare, led to the detection of mm polarization periodic variations, also consistent with the hot spot model at $5 R_S$ viewed at low inclination angle as found with GRAVITY (Wielgus et al., 2022). Very recent EHT polarization measurements of the persistent mm emission on the event horizon scale (EHT Collaboration et al., 2024) favour a clockwise rotating MAD around a very rapidly prograde spinning BH seen at very low inclinations. These recent data do not exclude the possibility of a jet, but, today, it is believed that the outflow from Sgr A* takes rather the form of a weak wind than the one of a focused jet (Ciurlo & Morris, 2026).

Another recent result from ALMA is the detection of a sub-mm H30 α hydrogen recombination line displaying a broad (2200 km s^{-1}) double-peaked profile arising within $0.3''$ of the source (Murchikova et al., 2019), interpreted as emission from a cold ($\approx 10^4 \text{ K}$) disk around Sgr A*. However, the lack of detection of associated H Brackett- γ line (Ciurlo et al., 2021) implies that the H30 α line must be amplified by a maser, which is problematic in a non-compact source like such an extended disk. The HD models of the YNC stellar winds in the central cavity, some now including matter accretion from the CND (Solanki et al., 2023), do allow the formation of such a disk, compatible with the sub-mm/IR measurements (Calderón et al., 2025), but the results critically depend on the model parameters and the topic is still debated.

Some of the main features discussed in this section are reported in the summary finding chart (Fig. 25–26) presented in the conclusion section (§ VII).

II. SEARCHES FOR THE HIGH-ENERGY EMISSION FROM THE GC

The GC view presented above and based on low-frequency measurements has been progressively enriched,

starting from the 1960s, by high-energy observations of the region. We summarize the historical developments of these measurements until the end of the last century in § II.A, and then present the instruments that have been used to observe it in X-rays (§ II.B) and at higher energies (§ II.C) over the last 25 years. Most of them are still in operation and regularly monitor the region, while new telescopes have also started to explore the GC and are mentioned along with planned future missions (§ II.D).

A. Early X/gamma-ray observations

The detection of high-energy emission from the GC dates back to the 1960s, at the very beginning of X-ray astronomy, when, using data of a 1964 Aerobee rocket flight, Bowyer et al. (1965) reported the discovery of an X-ray source in Sagittarius. Other measurements by sounding rocket experiments followed (Bradt et al., 1968; Clark et al., 1965; Fisher et al., 1966; Gursky et al., 1967) showing that most of the newly discovered X-ray sources, later classified as X-ray binaries (XRB), were clustering around the GC. In the 1970s, the region was monitored by the first X-ray satellites, *Uhuru*, *Ariel 5* and *HEAO 1*. The central source (4U 1743–29) detected by *Uhuru* appeared extended over $\approx 2^\circ$, either due to the combination of at least three point-like sources or to diffuse emission (Kellogg et al., 1971), while *Ariel 5* (Eyles et al., 1975) and other experiments (Cruddace et al., 1978) revealed, with large position errors, the presence of other bright, variable, or even transient objects (e.g. A 1742–294 and A 1742–289) and the occurrence of several X-ray bursts. At the end of the 1970s, it was already clear that, although the GC appeared quite active, and dominated by bright and variable XRBs, the X-ray luminosity of the nucleus itself was much lower than the one inferred for AGN (Proctor et al., 1978).

With the launch of the *Einstein* Observatory in 1978 it was possible, for the first time, to implement, at low energies, the grazing-incidence X-ray mirrors coupled to position sensitive detectors to image the sky with resolutions of $\approx 1'$. Watson et al. (1981) obtained the first X-ray images of the GC at these resolutions and showed that the central $20'$ of the Galaxy at $< 4 \text{ keV}$ were dominated by diffuse emission and a dozen of point-like sources, one of which coincident with Sgr A West and including Sgr A*. This source was then resolved into 3 weak objects with *ROSAT* more than 10 years later (Predehl & Truemper, 1994), leading to a measurement of a soft X-ray luminosity of only $10^{34} \text{ erg s}^{-1}$ for the one coincident within $10''$ with the nucleus.

Important results were also obtained on the GC X-ray diffuse emission, in particular by the *Ginga* satellite, that discovered a prominent 6.7 keV iron line diffuse emission from a region encompassing the whole CMZ (Koyama et al., 1989). This component resembled the diffuse

Galactic ridge emission (GRXE), distributed along the Galactic plane and characterized by a thin hot thermal plasma spectrum, with temperatures of 7–10 keV, which was discovered in the early 1980s with *HEAO 1* and *EXOSAT* missions (Warwick et al., 1985; Worrall et al., 1982). The possibility that the GC hosted such a large hot plasma cloud raised the question of its origin and source power, considering that, not being gravitationally confined, it needed to be refilled on rather short time scales (§ V.A). In the early 1990s the *Granat*/ART-P instrument discovered a harder (> 10 keV) diffuse emission associated with the molecular clouds of the region. This prompted speculation on whether this component could be due to Compton diffusion of X-rays emitted in the past by some very bright source (Sunyaev et al., 1993), possibly Sgr A* itself, leading to the prediction of Fe K α fluorescent line emission associated with the clouds. In 1994, the *ASCA* satellite was the first to separate the diffuse 6.7 keV line emission of ionized iron from the 6.4 keV one of neutral Fe atoms and showed that the distribution of the latter, unlike the one of the 6.7 keV line, was correlated with the molecular material (Koyama et al., 1996). The hypothesis of a past outburst from Sgr A* illuminating the clouds was then explicitly formulated (§ V.C).

While soft X-ray data revealed faint emissions from the GC, hard X-ray observations above 5–10 keV showed bright emissions in the direction of the GC. Early observations from 30 keV to few MeV detected a hard continuum and emission lines (Haymes et al., 1969, 1975), in particular at 511 keV (Lingenfelter & Ramaty, 1989) (§ VI.D.2), from the GC but with a localization uncertainty of a few degrees. These results were seen as evidence of the presence of a massive BH at the GC (Genzel & Townes, 1987), before coded mask imaging instruments, flown onboard satellites in the 1990s, increased the angular resolution of hard X-ray telescopes to better than 30' (Goldwurm & Gros, 2022). Observations in the 3–30 keV range with *SpaceLab2* (Skinner et al., 1987) and ART-P (Pavlinsky et al., 1994), as well as in hard X/soft γ -rays (30–1000 keV) with *Granat*/SIGMA (Goldwurm et al., 1994), then showed that the GC emission in these bands was rather due to the powerful hard XRBs in the area. The brightest is 1E 1740.7–2942, an *Einstein* source at 40' from Sgr A*, rather trivial in soft X-rays but with such a large hardness ratio and high variability in hard X-rays that it was quickly suspected to host a stellar-mass BH. The SIGMA results, including the detection of variable emission around 500 keV from the source (Bouchet et al., 1991), possibly explaining previous detections attributed to the GC nucleus (even if later measurements have not confirmed such a feature), prompted radio observations which led to the discovery of its extended radio jets and its classification as the first microquasar (Mirabel et al., 1992). The SIGMA derived upper limits for Sgr A* implied a very low luminosity ($< 10^{36-37}$ erg s $^{-1}$) even at energies larger than

30 keV (Goldwurm et al., 1994), difficult to reconcile with the BH accretion models and the expected accretion rates from the YNC winds (Melia & Falcke, 2001), questioning the very existence of the GC SMBH. This prompted the development of the ADAF models in order to explain the very low radiative efficiency of the central SMBH (Narayan et al., 1995) (§ I.E.2). In those years the OSSE instrument on *CGRO*, proved that the bulk of the 511 keV line emission was not variable, but rather diffuse and extended over the GB (Purcell et al., 1997), not confirming a direct link with Sgr A* (but see § VI.D.2).

Meanwhile, high energy (HE) γ -rays (50 MeV to 100 GeV) from the Galactic plane, with an increasingly significant concentration in the spiral arms and in the inner Galaxy (Bignami et al., 1975), were progressively detected since the 1960s by the satellites *EXPLORER XI*, *OSO-3*, *SAS-2* and *COS B*, that exploited the pair production process to detect photons at these energies. Interpreted as the result of cosmic-ray interaction with the ISM of the Galaxy, whose density increases towards the center, the measured gamma-ray emission by *COS B* seemed to imply an under-density of the CRs in the GC with respect to the local values (Blitz et al., 1985). However, later, Mayer-Hasselwander et al. (1998), using EGRET on *CGRO*, detected at the GC a source sticking out from the expected emission, also arguing that *COS B* data were compatible with their new results. The source (3EG J1746–2851) was positioned slightly away from the nucleus ($\sim 0.2^\circ$) but it could still be linked to Sgr A* given the large localization error (Hartman et al., 1999).

At very high energies (VHE, > 100 GeV), the technique based on detection of atmospheric Cherenkov light produced by particles generated by such gamma-rays was progressively implemented and refined in ground based observatories, until significant detection from the GC was claimed by Tsuchiya et al. (2004) with Cangaroo-II and by Kosack et al. (2004) with Whipple (see § VI.A for details on the HE/VHE gamma-ray GC source).

At the turn of the century, a new era of HE astronomy has been opened with the launch of the *Chandra*, *XMM-Newton* (1999) and *Suzaku* (2005) X-ray observatories; with the launch of the hard X-ray/low-energy gamma-ray missions *INTEGRAL*, *Swift* and *NuSTAR* and of the HE gamma-ray one *Fermi* (2002–2012), and with the start of operations (2003–2007) of more sensitive VHE gamma-ray telescopes (H.E.S.S., MAGIC, VERITAS).

B. X-ray telescope observations of the GC

NASA's *Chandra* X-ray Observatory (CXO, Weisskopf et al., 2002), equipped with the most powerful grazing incidence X-ray mirrors ever, reaches a still unequaled angular resolution of 0.5'' full width half maximum (FWHM) in a 17' \times 17' field of view (FoV) over 0.1–10 keV, thanks to the set of four 10 m focal mir-

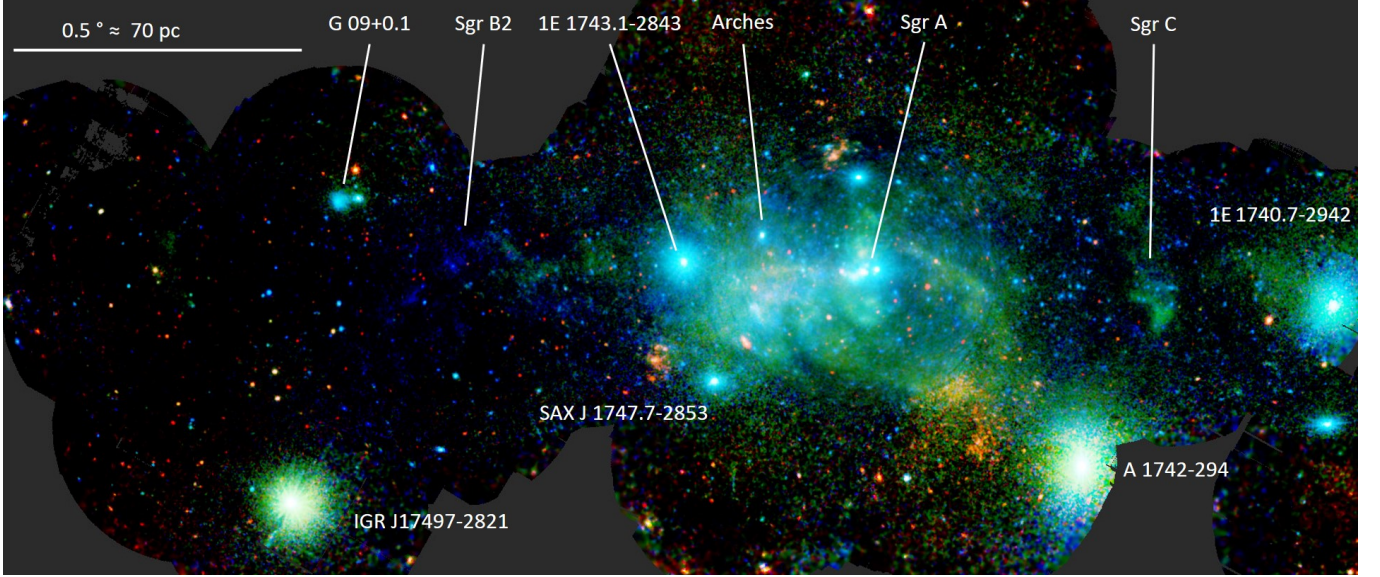


FIG. 6 The *XMM-Newton* GC Survey. Mosaic image of all *XMM-Newton* observations performed until 2015 within one degree of Sgr A* where in red, green and blue are showing the emissions in the 0.5–2, 2–4.5 and 4.5–12 keV energy bands, which include X-ray radiation from X-ray binaries, star clusters, supernova remnants, bubbles and superbubbles, H II regions, PWNe, non-thermal filaments, nearby X-ray active stars, Sgr A complex and other features (adapted from Ponti et al., 2015b, original image credit ESA/XMM-Newton/G. Ponti).

rors associated to the Advanced Charge-Coupled Device (CCD) Imaging Spectrometer camera disposed for imaging (ACIS-I). While the spectral resolution of the CCD remains moderate (100–200 eV, FWHM), high spectral resolution (power 100–500) can be obtained using dispersive grating systems, the one working at > 2 keV being the High Energy Transmission Grating spectrometer (HETG) coupled to a CCD set disposed for the use (ACIS-S). Launched in July 1999 *Chandra* started observing the GC in the fall, which led to the first solid detection of Sgr A* in X-rays (Baganoff et al., 2001) and since then accumulated several millions of seconds (Ms) of exposure on the source, in particular with a dedicated X-ray Visionary Project (XVP) of 3 Ms in 2012 with HETG/ACIS-S, and few large surveys of the CMZ and other regions (e.g. Munoz et al., 2009) (Fig. 17, right).

XMM-Newton (Jansen et al., 2001), the European Space Agency (ESA) X-ray Observatory, was launched a few months after *Chandra*. Hosting three sets of 58 nested mirrors with three different European Photon Imaging Cameras (EPIC), 2 CCD MOS and 1 CCD pn, at their 7.5-m focal planes, offers a lower angular resolution, $\approx 15''$ half energy width (HEW), than *Chandra* but with three times larger (≈ 1000 cm 2) effective area over a 30' diameter FoV and better spectral resolution along a broader range (0.1–12 keV). The numerous individual observations with the EPICs, three major surveys of the CMZ in 2000–2001, 2012 and again in 2020, and two large projects to explore the GC polar regions allowed the early detection of Sgr A* flares, the full mapping of the region (Fig. 6, 16, 17 left) (see e.g. Ponti et al., 2019,

2015b) with several discoveries and studies, also of variable features (e.g. Terrier et al., 2018) and the collection of a very large set of high-quality data.

The JAXA observatory *Suzaku* (Mitsuda et al., 2007), carrying four X-ray mirrors coupled to CDD detectors, was characterized by low background and good spectral resolution, features that allowed several important studies in particular of the diffuse emission. Several surveys of the GC were performed using the XIS instrument working in the range 0.1–10 keV, with angular resolution of $\approx 2'$ (HEW) in a FoV of 17' and effective area of 4×200 cm 2 , particularly to the study the iron lines distribution in the region (e.g. Koyama, 2018; Uchiyama et al., 2011). *Suzaku* stopped operations in 2015.

NASA's Neil Gehrels *Swift* Observatory (Gehrels et al., 2004) instead was used to monitor GC X-ray transients and flaring activity of Sgr A* using its X-Ray Telescope (XRT), composed by a mirror set coupled to an EPIC/MOS CCD detector, to image sky areas of 23' size in 0.2–10 keV with effective area of ≈ 120 cm 2 and angular resolution of $\approx 20''$ HEW. A program to regularly monitor the central 25' of the Galaxy started in 2006, one year after the launch, with short (1 ks) snapshots every 1–4 days during the target visibility periods. It provided until 2014 some 1200 observations for a total exposure of 1.3 Ms (Degenaar et al., 2015) and it is still on-going.

C. Hard X-rays and gamma-rays GC surveys

After the *Granat* mission, the coded mask technique was refined and largely applied to image the sky in the hard X-ray range (20–300 keV) and in low-energy gamma-rays (300 keV to 10 MeV). The ESA International Gamma-ray Astrophysics Laboratory (*INTEGRAL*), was launched in 2002, carrying three coded mask instruments, JEM-X, IBIS and SPI to cover a broad energy range from 3 keV to 10 MeV (Winkler et al., 2003, and references therein) in FoVs that span between 13° and 45° sides. The large FoV of such instruments and the very regular *INTEGRAL* surveys of the GC until the end of the mission early 2025 have provided, fine images of the CMZ and surrounding region in hard X-rays (Bélanger et al., 2006a), thanks, in particular, to the Imager on Board the *INTEGRAL* Satellite (IBIS), and its unprecedented angular resolution of 12' in 20–1000 keV over a 30° wide FoV. *INTEGRAL* revealed a peculiar central excess (Bélanger et al., 2004), monitored the variable sources that dominate the GC hard X-ray emission, discovered the hard emission of Sgr B2 (Revnivtsev et al., 2004) and its monotonic decrease over years (Terrier et al., 2010). The Spectrometer on *INTEGRAL* (SPI), with its high spectral resolution (power ≈ 250), provided by Germanium detectors cooled to low temperatures, and moderate imaging capabilities ($\approx 2.7^\circ$ FWHM) has been used to more precisely map the 511 keV line emission of the Galaxy and study its spectral shape (Knöldlseder et al., 2005; Siegert et al., 2016).

A real revolution in imaging the low-energy part of the hard X-ray range has been accomplished 10 yr later with *NuSTAR*, a NASA mission launched in 2012, carrying a set of mirrors with a multi-layer coating able to reflect 3–80 keV X-rays to solid state detectors placed at 10 m focal length, thanks to an extendable mast (Harrison et al., 2013). This telescope features 1' HEW resolution in a 12' side FoV with an effective area comparable, at 6 keV, to the *XMM-Newton* EPIC/pn one. Large GC surveys have been carried out with *NuSTAR* (Hong et al., 2016; Mori et al., 2015), along with a number of observations of localized regions. These have allowed to detect the Sgr A* flares at more than 20 keV, to resolve the complex hard X-ray emission of the central 20 pc and to study of a number of hard sources of the CMZ.

Above 20 MeV, gamma-ray observatories rely on the pair creation process, directly observed in space in the high-energy range and through the atmospheric cascade it creates for ground-based instruments in the very high energy range (above 100 GeV). Launched in 2008, the *Fermi*/LAT is able to operate from few tens of MeV up to few hundred GeV thanks to its precision tracker, its thick calorimeter and its segmented anti-coincidence shield which permits a very efficient background rejection (Atwood et al., 2009). With its very large field of view and its scanning observation mode, *Fermi*/LAT observa-

tions cover the full sky in a few orbits and provide a very uniform sky survey. Besides a collection of more than 6000 sources (Abdollahi et al., 2020), the *Fermi*/LAT discovered large-scale structures connected to the GC: the *Fermi* bubbles (Su et al., 2010) and the Galactic center GeV excess (see e.g. Ackermann et al., 2017). While the angular resolution is rather modest below the GeV range ($\geq 1^\circ$) making source confusion a major issue to study the inner degree, the good performances at higher energies ($\leq 0.1^\circ$ above 30 GeV) allow for more precise measurements (Cafardo et al., 2021).

Above ~ 100 GeV, Imaging Atmospheric Cherenkov Telescopes (IACT) observe the Cherenkov radiation produced in the atmosphere by the cascade of secondary charged particles induced by incident cosmic particles (see e.g. de Naurois & Mazin, 2015). This technique offers a very large collection area, essential in the VHE range where photons are very scarce. Modern instruments, such as H.E.S.S., MAGIC or VERITAS rely on stereoscopic observations of air showers which provide good angular resolution (around or below 0.1°) and a satisfactory background rejection. MAGIC is a system of two 17m diameter IACTs located on the island of La Palma, with a threshold of ~ 50 GeV (Aleksić et al., 2016). VERITAS is an array of four 12 m IACTs located in southern Arizona (Adams et al., 2021). H.E.S.S. is an array of four 12m telescopes (Aharonian et al., 2006a), plus a large 28m telescope added in 2012 at the center of the array (H.E.S.S. Collaboration et al., 2018c). It is located in Namibia, which is more suited to observe the inner Galaxy compared with northern hemisphere locations, where the region can only be observed at relatively low elevation, increasing the energy threshold of detectable gamma-rays. Deep surveys of the GC have been conducted by the three experiments and revealed several sources and diffuse emission in the inner degrees.

Finally, particle sampling arrays, such as HAWC (Abeysekara et al., 2023) and LHAASO WCDA or KM2A arrays (Cao et al., 2024), directly measure secondary shower particles and can probe up to ultra-high energy (UHE) gamma-rays from several tens of TeV up to the PeV range with an angular resolution of about 0.3°. Both observatories are located in the northern hemisphere and can only observe the GC at very low elevations.

D. Recent and future instruments

Amongst the recent HE instruments that observed the GC, *eROSITA* (Predehl et al., 2021), launched in 2019 on board the Russian-German *SRG* mission, has a range, an effective area and an angular resolution comparable to *XMM-Newton*, but larger FoV (1.3°), and it was designed to carry out deep all-sky X-ray surveys. One of its major results is the discovery of two gigantic polar bubbles

extending to 80° above and below the GC, enveloping the gamma-ray *Fermi* bubbles (Predehl et al., 2020) and it also provided results on the emission reflected by the CMZ clouds (Khabibullin et al., 2022). *eROSITA*, despite being fully efficient, suspended operations in 2022 following geopolitical events².

The other new facility used to explore the GC is *IXPE* (Weisskopf et al., 2022), the first observatory dedicated to imaging X-ray polarimetry, launched in 2021 and which carries three X-ray mirror telescopes with polarization sensitive detectors, for an angular resolution of $\approx 30''$ and a FoV of $17'$. The main objective of the *IXPE* GC observations was to search for polarization of the reflected emission from the molecular clouds (Marin et al., 2023).

Great expectations for the study of the GC are placed on the new generation of X-ray observatories equipped with non-dispersive high spectral resolution spectro-imagers based on X-ray calorimeters. The recently launched (2024) *XRISM* observatory (Tashiro et al., 2021) is the first of such missions to be operating. It carries a micro-calorimeter that provides data with an unprecedented energy resolution of 5 eV (FWHM) over a $3'$ FoV with the angular resolution of $\approx 1'$ (HEW), and is already providing interesting results on the GC (XRISM Collaboration et al., 2025). The future *NewAthena* X-ray observatory, expected for the late 2030s, will carry the X-ray Integral Field Unit, a spectral-imager with an exceptional resolution of 4 eV, angular resolutions of $8''$ – $10''$ and an effective area of 1.4 m^2 , over a FoV of $4'$ diameter in the 0.2–12 keV range (Peille et al., 2025), greatly improving the performances with respect to *XRISM*.

For the low-energy gamma-ray band, 300 keV–10 MeV, called the MeV Gap because the least explored part of the electromagnetic spectrum, several experiments have been proposed in recent years, and at the moment the Compton telescope *COSI* (Tomsick et al., 2024) is the one planned to fly soon. The expected sensitivity, over a very large FoV (1/4 of the sky) with an angular resolution of 4° – 2° , is several times better than SPI at 0.5–2 MeV. The design of future MeV missions of superior sensitivity is currently debated in the community for operation in the next decades (Siegert et al., 2022).

Important advances on the GC gamma-ray properties are also expected from the Cherenkov Telescope Array Observatory (CTAO). It consists of two hybrid arrays of large, medium and small size telescopes covering a broad energy range with sensitivity improved by a factor of up to ten compared with current IACTs. The southern part of the observatory will be deployed in Chile and will be fully operational at the end of the decade. A deep GC survey is foreseen among the observatory key science programs (CTA Consortium et al., 2019). It will allow the

exploration of the region in the 20 GeV to 100 TeV range with an angular resolution of a few arcmin and much larger sensitivity than the present IACTs. In addition, particle samplers in the southern hemisphere such as the Southern Wide-Field Gamma-ray Observatory (SWGO), project currently in the study phase, will open the window of the UHE gamma-rays at the GC.

III. SGR A* AND ITS CLOSE ENVIRONMENT AT HIGH ENERGIES

While the main goal of the early GC HE observations was to detect emission from the SMBH, only *Chandra* has in fact the resolution needed to disentangle the complex X-ray morphology of the central few parsecs. *Chandra* detected the persistent X-ray counterpart of Sgr A* (§ III.A) soon after its launch and discovered one year later also its peculiar flares (§ III.B). We are certain that this source is associated with the SMBH because its flares are simultaneous to NIR ones, which can be positioned at μas precision on Sgr A* with GRAVITY. The SMBH is surrounded and fed by hot gas produced by massive star winds (§ III.A) and by several peculiar X-ray sources in the inner 20 pc (§ III.C).

A. Sgr A* quiescent emission and central hot plasma

1. Sgr A* quiescent emission and accretion flow

From the very first GC observations in 1999, *Chandra* resolved the central *ROSAT* source associated with Sgr A into several components (Fig. 7, left) and in particular detected, at $< 0.27''$ from Sgr A*, a very weak and steady source displaying a 2–10 keV luminosity of only $(2\text{--}3) \times 10^{33} \text{ erg s}^{-1}$ at the GC and showing an extended morphology (Baganoff et al., 2003). The source intrinsic size ($1.4''$ FWHM) is comparable to the estimated Bondi radius of the accretion flow of Sgr A*, and later studies showed that the morphology appears elongated and oriented in a similar way than the clockwise disk of the YNC, even if the significance of this feature has not been quantified (Wang et al., 2013). Between 4 and 20% (depending on the analysis) of the quiescent emission can be attributed to a central inner point-like component (Neilsen et al., 2013; Nowak et al., 2012; Wang et al., 2013), possibly including undetected weak flares, and the overall emission appears steady, even after the pericenter passage of S2 and G objects in their orbits around the SMBH (Yuan & Wang, 2016).

Building upon previous spectral studies (Baganoff et al., 2003; Xu et al., 2006), detailed analyses of a very large *Chandra* data set, including the high energy resolution ones from the XVP, and implementing proper treatment for contaminating sources, pileup and dust scattering, have provided high-quality spectra of the Sgr A*

² See <https://www.mpe.mpg.de/7856215/news20220303?c=450698>

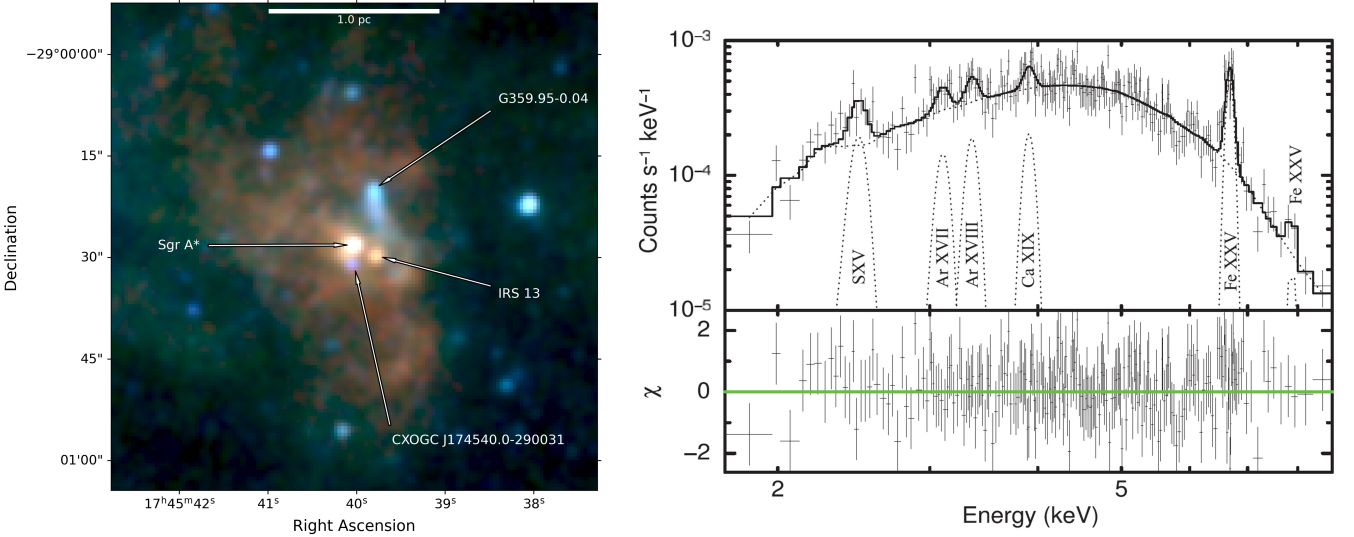


FIG. 7 Sgr A* X-ray quiescent emission and surrounding sources. Left: *Chandra* 3-color X-ray image of the central 1.2' (2.8 pc) (red: 1.5–2.6 keV, green: 2.6–4.5 keV and blue 4–5–7.5 keV). It shows the source associated with Sgr A* at the center, the diffuse hot gas emission visible in red, the cometary-shaped PWN (G359.95–0.04), the massive stellar cluster IRS 13 as well as other point-like sources in the field. Right: *Chandra* HETG absorbed count spectrum of the Sgr A* quiescent emission, within 1.5'' and out of flare periods, modeled with a thermal spectrum and Gaussian lines (from Wang et al., 2013).

X-ray quiescent emission (Fig. 7, right), allowing for the detection and characterization of several plasma emission lines (Corrales et al., 2020; Wang et al., 2013). The spectrum, within $R = 1.5''$ after excluding flaring periods, could be modelled with a thin thermal plasma at 3.5 keV temperature in collisional ionization equilibrium with the clear presence of a prominent, 700 eV equivalent width (EW), K α emission line of the He-like ionized iron (Fe xxv) complex at 6.67 keV and K α lines of several other species (He- and H-like ions of Ar, S and Ca), in particular the 3.1 keV line of Ar xvii (200 eV EW), as well as of He-like Fe K β .

The Sgr A* steady X-ray emission is generally interpreted as thermal emission produced by the captured gas at the Bondi radius. Possibly after a thermalizing shock, this gas is accreted onto the BH, heating up along its fall to virial temperatures. The density, velocity and temperature profiles are driven by the physical characteristics of the accretion flow and by the initial conditions. Precise line emission diagnostics can differentiate the possible type of accretion flow models (Narayan & Raymond, 1999; Xu et al., 2006; Yuan et al., 2003, see also § I.E.2) and the *Chandra* data appear, within uncertainties, compatible with most of the radiatively inefficient ones, except those without outflows, which predict too steep density profiles, i.e., pure Bondi or pure ADAF models (Corrales et al., 2020). The spectrum could be well fit by an absorbed thin thermal model that includes density and temperature distributions predicted by a RIAF with outflows, with an equivalent hydrogen absorption column density $N_{\text{H}} = 1.38 \times 10^{23} \text{ cm}^{-2}$ and abundances of about 1.5 solar, both compatible with expected values at the

GC. In a recent and detailed analysis of the XVP data, Balakrishnan et al. (2024) obtained similar results, with a best-fit for the Sgr A* quiescent spectrum by a RIAF model with nearly as much outflow as inflow of matter, and with shallow variation of temperature, but with best-fit iron abundances below solar.

Incidentally the derived upper limits on the 6.4 keV line of neutral iron in this emission (Wang et al., 2013) are excluding an important contribution from coronal emission of low-mass stars in the NSC cusp which had been suggested by Sazonov et al. (2012). The *Chandra* Sgr A* quiescent emission slope is reported in the overall average SED represented in Fig. 5, where it is compared to the model of Yuan et al. (2003), a RIAF including outflows with a subdominant population of non-thermal electrons explaining the low-frequency radio data and the seed from which the non-thermal flares can start, and where the bulk of the X-rays are attributed to thermal bremsstrahlung.

2. Surrounding hot plasma and influence on the accretion flow

Chandra also detected an X-ray diffuse emission in the central cavity, surrounding Sgr A*, within $\approx 10\text{--}15''$ (0.4–0.6 pc) from it (Fig. 7, left). It is also characterized by a thermal spectrum but with an iron line centered at lower energies than the Fe xxv complex, indicative of a non ionization equilibrium state. This hot plasma with a patchy morphology is slightly peaked towards Sgr A*, has a mean electron density of 26 cm^{-3} , a temperature $kT = 1.3 \text{ keV}$ and an estimated total mass of $0.1 M_{\odot}$

(Baganoff et al., 2003). It has been explained as the gas of the powerful stellar winds from massive stars in the nearby YNC, heated by the shocks produced by their mutual collisions that efficiently converts the wind kinetic energy into gas internal energy (Rockefeller et al., 2004). This is supported by detailed hydro-dynamical (HD) simulations of the YNC stellar winds interactions that take into account the spatial and velocity of the stars as well as the confining effect of the surrounding CND. They reproduce the X-ray plasma properties observed with *Chandra* (Calderón et al., 2020; Cuadra et al., 2008) as well as its morphology (Ressler et al., 2018). The equilibrium state is reached in only a few thousand years from the onset of stellar-wind ejection, excluding a long-term impact by the Sgr A East SNR shell passing-by or by putative ancient powerful BH outflows. However, recent simulations have incorporated continuous and outburst BH outflows occurring 100–300 yr ago and indicate that they may still influence the plasma properties (Russell et al., 2017, see also § V.C).

This gas also provides the bulk of the material accreting onto the SMBH, and from its X-ray measured properties, it is possible to establish the initial conditions of the flow. The SMBH Bondi radius for this material is then estimated at $2.8''$ (0.1 pc), compatible with the Sgr A* quiescent source size, and the mass accretion rate at this radius at $10^{-6} M_\odot \text{ yr}^{-1}$, also compatible with the HD simulations. The most recent 3D simulations, attempt to follow the gas fate all the way down to the inner regions of the accretion flow, incorporating radiation cooling and circularization of the flow in a disk, equatorial and polar outflows and GRMHD processes at play, establishing the conditions in the inner few tens of R_S . They seem to show that the initial conditions are indeed crucial also to understand the very inner ($< 100 R_S$) properties of the flow, in particular that the accretion disk, possibly generating the signal observed with the EHT (sub-mm quiescent emission) or GRAVITY (non-thermal flares), may retain the initial orientation of the disk distribution of the stellar-wind-emitting stars (Ressler et al., 2020). These results are still preliminary, in a very active area of investigation, where large efforts are devoted to improve these simulations and further constrain the models (e.g., Calderón et al., 2025).

B. Sgr A* flaring activity

One major result of the GC surveys with the new generation of X-ray telescopes was the discovery of the Sgr A* X-ray flares (Fig. 8). They were first observed with *Chandra* in 2000 (Baganoff et al., 2001), confirmed soon after by *XMM-Newton* (Goldwurm et al., 2003), and then also detected in NIR in 2003 (Genzel et al., 2003; Ghez et al., 2004, see § I.E.2). Given that these events allow us to explore the very inner region of the SMBH,

they have been searched for and studied with most HE observatories (Bélanger et al., 2005; Nowak et al., 2012; Porquet et al., 2003b; Trap et al., 2010) including instruments in hard X-rays and gamma-rays (Aharonian et al., 2008a; Trap et al., 2011), and finally detected also with *Swift/XRT* (Degenaar et al., 2013) and *NuSTAR* (Barrière et al., 2014).

1. High-energy properties of Sgr A* flares

During these flares, the source X-ray luminosity increases by up to 1–2 orders of magnitude, with the brightest events reaching peak values of $L_X \sim 5 \times 10^{35} \text{ erg s}^{-1}$ in the 2–10 keV band (Haggard et al., 2019; Nowak et al., 2012). Spectra are featureless and can be described by absorbed power-laws with $N_H \approx 10^{23} \text{ cm}^{-2}$ (placing them at the GC) and photon indexes of $\Gamma \approx 2.3$, harder than the quiescent emission ($\Gamma \approx 3$) and extending up to $> 40 \text{ keV}$ (Barrière et al., 2014)³.

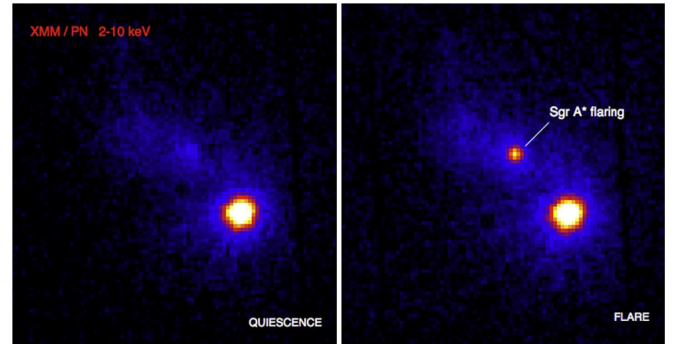


FIG. 8 Bright Sgr A* X-ray flare observed with *XMM-Newton* in 2007: the 2–10 keV image of the GC inner 15-pc region before (left) and during (right) the flare (from Trap et al., 2010). The bright source in the lower-right side is AX J1745.6–2901, a transient XRB particularly active in 2007 at about $1.45'$ from the SMBH.

They occur randomly (Fig. 9), last from few tens of minutes to 3 hours, with light curves that appear roughly symmetrical around their centroid (Fig. 10, bottom) but that show short time-scale variations down to 100 s, which indicates that the emission is produced in regions as compact as $10 R_S$.

Neilsen et al. (2015, 2013), using the 3 Ms XVP *Chandra* program, established that the flaring rate is constant at $1.1_{-0.3}^{+0.2}$ per day and that the X-ray flux cumulative distribution function (CDF) is fitted, above the quiescent emission described by a Poissonian process, with an inverted power-law of slope $1.92_{-0.02}^{+0.03}$. This is reminiscent of the description of the NIR CDF with two laws

³ First measurements found very hard spectra ($\Gamma \approx 1$) that were later attributed to pile-up and scattering effects that had not been fully accounted for (see Nowak et al., 2012).

respectively for the quiescent and flaring states (Dodds-Eden et al., 2011; GRAVITY Collaboration et al., 2020a), which is still a controversial topic though. The power spectral densities measured during flares show the presence of red-noise, which makes the detection of significant periodicity quite tricky. In fact no significant detections of quasi periodicities are found in the X-ray (and NIR) light curves of flares, in spite of early claims of a signal around 20–30 min (Bélanger et al., 2006b, and references therein), thus, as for NIR, if the orbital motion detected with VLT/GRAVITY is a characteristic of all flares, the process does not last enough to produce a significant coherent (quasi) periodicity signal in the emission. Ponti et al. (2015a), from a re-analysis of all flares measured with *Chandra* and *XMM-Newton* until 2015, found that the rate of bright and very bright events significantly increased starting from summer 2014, and tentatively attributed the effect to the G2 2014 periastron passage. While this result was confirmed by Mossoux & Grossi (2017), Bouffard et al. (2019), based on a longer *Chandra* data set, claimed no variation of the X-ray rate, while Andrés et al. (2022), using *Swift*, did measure significant flaring activity increases in 2006–2007 and 2017–2019 periods, compared to the years 2008–2012.

The average flare X-ray spectra have been studied deeply for several bright flares. Today the accepted best-fit X-ray spectral model is an absorbed inverted power law, with index $\Gamma = 2.20 \pm 0.15$ and $N_{\text{H}} = (1.60 \pm 0.15) \times 10^{23} \text{ cm}^{-2}$, where uncertainties are mainly due to the large absorption that has a strong effect on the slope determination (e.g. Ponti et al., 2017, and references therein). In spite of early claims, there is no significant change of slope from one flare to the other, so it does not seem to depend on their strength or duration. *NuSTAR* stacked spectra show that emission extends up to 79 keV with the same slope without significant spectral break (Zhang et al., 2017). The absorption is similar to that observed in close-by objects (e.g. the central magnetar and other transients) and is considered to be entirely due to intervening ISM along the LoS rather than local, and is therefore assumed to be constant.

2. NIR flares and multi-wavelength campaigns

Since the detection in the NIR, several large multi-wavelength campaigns (MWCs) have been organized in order to study the simultaneous properties of the flares at all frequencies. Given the random nature of the phenomenon, the presence of nearby transients, and the difficulty of coordinating ground and space observatories, not all MWCs were successful or complete. Their results were sometimes controversial, and some still are. However they have clearly shown that all X-ray events have correlated NIR counterparts, while the contrary is not true: IR flares show higher rates (≈ 3 –4 per day on av-

erage) than X-rays, longer durations and some of them, even if bright, do not show correlated X-ray events.

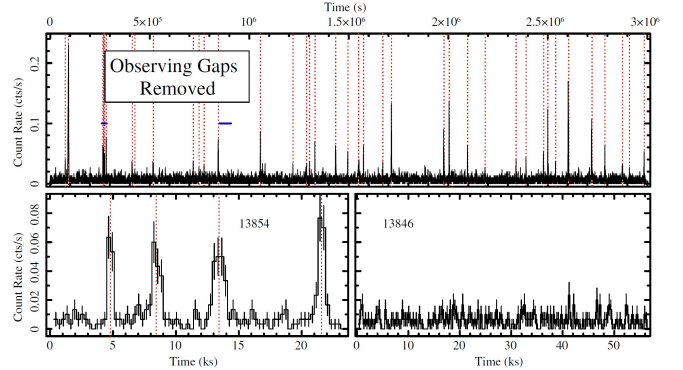


FIG. 9 X-ray light curves of Sgr A* showing the flares detected by *Chandra* during the XVP observations (data gaps excluded) performed in 2012. Lower panels show a zoom of the curve during observations with several flares (left) and without any (right). From Neilsen et al. (2013).

Initial claims of X-rays delayed by up to 10 min with respect to NIR ones (Yusef-Zadeh et al., 2012) that would suggest an external inverse Compton (EIC) mechanism for the origin of X-rays, were not confirmed (see also Fig. 10). Instead, recent detailed works based on *Spitzer* and *Chandra* simultaneous observations, along with archival data, concluded that no lags are significantly detected (Boyce et al., 2022, 2019). This rather supports synchrotron (SYN) or Synchrotron Self Compton (SSC) processes for the origin of X-rays (as first proposed by Liu & Melia (2002); Markoff et al. (2001)) instead of EIC (see § III.B.3). Even if they peak at the same time, NIR flares generally start before and end after X-ray ones and also appear more structured (Fig. 10).

Search for significant time delays have been carried out also on sub-mm and radio variability compared to IR or X-rays, but, up to now, no fully compelling detection is reported. At these frequencies the variability is much lower, at level of 10–40%, and a solid identification of flares (and in particular their association to NIR or X-ray ones) is much more complicated. Delays of peaks between low frequency bands were claimed in several occasions, and interpreted as due to a synchrotron plasmoid adiabatic expansion, where the self-absorbed synchrotron peak moves to low energies as the plasma absorption decreases due to expansion. In spite of the suggestive physical process, and the diagnostic power of the model (van der Laan, 1966), in several occasions it was shown that the predicted flux ratios, when considering delays with respect to X-ray peaks, do not fit expectations (Marrone et al., 2008; Trap et al., 2011) and most of the claimed lags are not significant and/or the association of peaks at different bands not fully convincing. In a recent work on Sgr A* variability in different frequency bands, Witzel et al. (2021) claim an overall 30 min delay of the sub-

mm variability with respect to the NIR one, and discuss this in the frame of the plasma cloud adiabatic expansion process, while additional results on the 2019 MWC (Michail et al., 2024) seem also to revive the interest in this process.

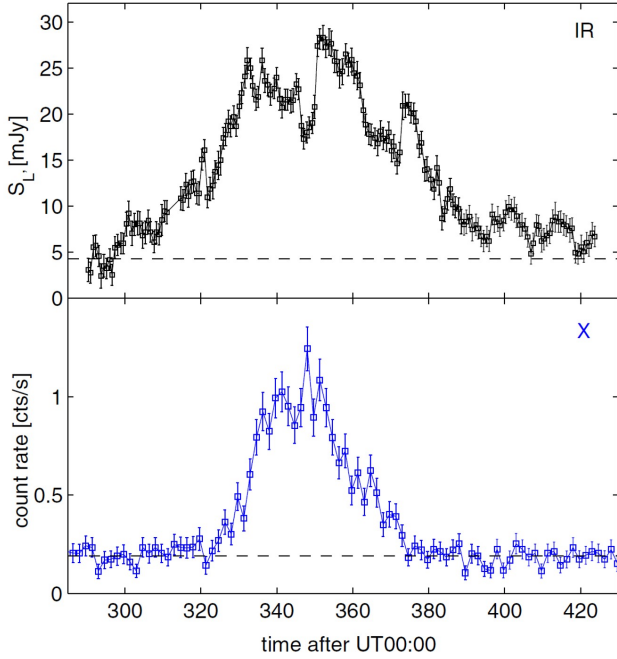


FIG. 10 Sgr A* flare light curves obtained during a MWC: X-ray count rate in 2–10 keV (lower panel) and fluxes in the NIR L band (upper panel) versus time (minutes) of the bright 2007 Sgr A* flare observed with *XMM-Newton* and VLT/NACO (adapted from Dodds-Eden et al., 2009).

3. Constraints from multi-wavelength spectral analyses

Spectral properties over a broad range of frequencies are essential to establish the radiation mechanisms at work. NIR and X-ray average spectra have different slopes. In the νF_ν units, the average IR slopes are rising with frequency ($\beta \approx 0.3$) while the X-ray ones are decreasing ($\beta \approx -0.2$)⁴.

However the average spectra are not enough to draw firm conclusions and the simultaneous measurements of spectral slope and variability in NIR and X-ray obtained

in MWC are necessary to properly constrain the radiative models. Little doubt exists for the mechanism responsible for the IR light. Linear polarization and non-thermal slope indicate that it consists of thin synchrotron emission produced by a transiently accelerated population of non-thermal (or hot thermal) relativistic (≈ 1 GeV i.e. $\gamma \approx 10^{2-3}$) electrons, at few R_S from the BH, in the magnetic field (10–50 G) of the accretion flow or of the jet. However, X-rays could be produced by several different mechanisms. Either the transient electron energies extend up to high-energies (≈ 100 GeV, i.e. $\gamma \approx 10^{5-6}$), giving rise to X-rays also through synchrotron radiation (SYN, Dodds-Eden et al., 2009; Ponti et al., 2017) or X-rays are produced by inverse Compton (IC) processes. The IC scattering is done by the same electrons that emit by synchrotron the NIR flare which either scatter the same IR photons to X-rays, through the so called Synchrotron Self Compton process (SSC, Eckart et al., 2008) or scatter the quiescent sub-mm thermal emission (EIC, Yusef-Zadeh et al., 2006) of the accretion flow⁵. In case of simple SYN, the slope shall extend to the X-rays unchanged, but since high-energy electrons cool faster (time scales of ≈ 30 s) than low-energy ones (≈ 30 min), a spectral break ($\Delta\Gamma \approx -0.5$) is expected at a break frequency between IR and X-rays. Because of the fast cooling, this model requires electrons to be continuously accelerated during flares, which last much longer than the cooling time of the electrons producing X-rays. IC generally tends to produce boosted photons with the same spectral shape as the original seed photons, so IR and X-ray shall present the same slopes.

While the first simultaneous X-ray/NIR detection of a weak flare was made in 2003 with VLT and *Chandra* (Eckart et al., 2004), the first significant spectral constraints in both bands were obtained in a MWC for the very bright 2007 Sgr A* flare, observed simultaneously with *XMM-Newton* and the VLT (Fig. 10). The VLT/VISIR measurement in the MIR (Dodds-Eden et al., 2009; Trap et al., 2010), simultaneous to a NACO one in the NIR, set an upper limit on the IR slope, showing that it had to be very hard compared to the X-ray one. The authors interpreted the feature as supporting a broad-band synchrotron emission with a cooling break and showed that IC and SSC could fit the data only if assuming very extreme physical parameters (magnetic field, tiny emitting zone, huge electron densities). The first real simultaneous spectra were however obtained in a MWC which involved the spectrometer SINFONI of the VLT

⁴ NIR flux F_ν is often given in Jy units and the power-law slope by the frequency index α ($F_\nu \propto \nu^\alpha$), while X-ray flux is in $\text{ph cm}^{-2} \text{s}^{-1} \text{keV}^{-1}$ units with inverted power-law photon index Γ ($F_X \propto E^{-\Gamma}$), and are often compared in νF_ν ($\text{erg cm}^{-2} \text{s}^{-1}$) or luminosity νL_ν (erg s^{-1}) units with β index ($\nu F_\nu \propto \nu^\beta$). Indices relations are then: $\alpha = 1 - \Gamma$, $\beta = \alpha + 1$. If photons are produced by an electron population with inverted power-law energy distribution of index p ($n_e \propto \gamma^{-p}$), by SYN or IC, then we also have $\beta = \frac{3-p}{2}$.

⁵ The case in which the mildly relativistic (10–50 MeV) electrons that produce the quiescent sub-mm emission scatter the transient synchrotron NIR radiation was also considered (Yusef-Zadeh et al., 2012) but Dodds-Eden et al. (2009) demonstrated that, at least in the optically thin case, it is always negligible compared to the primary EIC process (IR-electrons scatter sub-mm photons).

for another very bright flare, observed simultaneously in 2014 also with *NuSTAR* and *XMM-Newton* (Ponti et al., 2017, and Fig. 11, left). Again, while EIC is completely excluded by these data, the SYN model is preferred over the SSC, but it needs two additional features: the maximum energy (γ_m) of the electron distribution must vary during the flare as well as the cooling break frequency. These features can explain why IR flares last longer than X-ray ones: at the beginning γ_m is below the limit that gives X-rays, then rises to 10^{5-6} producing the HE flare and then decreases again below the X-ray threshold. The varying break frequency can explain why NIR spectra are steeper (redder) at low intensities, when it moves into the IR range. This variation indicates a possible magnetic origin of the energy reservoir that powers the events, as the cooling frequency is related to the magnetic field.

The most recent successful MWC involving GRAVITY, in coordination with *Spitzer*, *NuSTAR* and *Chandra*, caught a very bright NIR flare in 2019 associated with a moderate X-ray one (GRAVITY Collaboration et al., 2021). The detailed time-resolved spectral analysis of this excellent data set again support the SYN model if it is assumed, in addition to the features identified previously (variable cooling break and varying γ_m of the particle distribution), also an exponential decrease of the electron distribution above γ_m rather than a sharp cut-off (Fig. 11, right). Both EIC and SSC models are ruled out because they cannot fit the difference between X-ray and NIR slopes and their relative fluxes, unless accepting really extreme parameters and notably an extreme magnetic field. In addition to the poor fit, the authors argue that the extreme field implied by the IC models, would decrease the cooling time so much that variations shorter than tens of seconds shall be observed in both IR and X-ray light curves, while they are not. The only IC model that could fit the data is the one in which also IR are due to SSC (SSC-SSC, Witzel et al., 2021) from electrons producing sub-mm flare by synchrotron (if IR are not due to SYN, B can stay low even though γ is low) but with the caveat that electron densities need to be very high ($\approx 10^{10} \text{ cm}^{-3}$), which is at odds with the expected densities of the accretion flow (GRAVITY Collaboration et al., 2021).

4. Summary and possible origins of the events

In conclusion, at present, radiation mechanisms of the Sgr A* flares seem better explained if one uses simple single-zone models, by those where both IR and X-rays are produced by synchrotron emission of transiently accelerated electrons, with varying maximal energy of the electron distribution and exponential cut-off above this energy, possibly powered by the magnetic field, as in magnetic reconnection events. In this picture (GRAVITY Collaboration et al., 2021; Ponti et al., 2017) the

magnetic field decreases during the event and then goes back to its value of the steady accretion flow at the end of the flare. This variation produces a shift of the cooling break frequency down to IR frequencies, producing the steeper IR slopes, detected at the beginnings and ends of the events, when the intensity is low.

In recent works on the 2019 MWC (Boyce et al., 2022; Michail et al., 2024) the SYN (for sub-mm) - SSC (for NIR) - SSC (for X-rays) radiative model (Witzel et al., 2021), associated to a plasma cloud adiabatic expansion, has been re-proposed. However the data of the most recent MWC (2024), when it was possible for the first time to detect a flare in MIR with the JWST, in absence of an X-ray flare but along with a 40 min delayed sub-mm event, can again be explained with a pure SYN model with gradual cooling of electrons accelerated by magnetic reconnection and/or magnetized turbulence (von Fellenberg et al., 2025). As GRAVITY Collaboration et al. (2021) conclude, certainly a fully coherent and complete model of Sgr A* flares explaining both spectral and variability properties in all frequency ranges is still lacking.

The primary origin of the phenomenon is also not yet fully understood and several ideas have been proposed to explain the process that powers the flares. While some consider just energy transfer from the plasma magnetic field to the particles, others evoke temporary larger accretion rates, that eventually power either MHD instabilities, shocks or magnetic re-connection in the inner flow (Yuan et al., 2003), or the activity of the jet (Markoff et al., 2001), as for example accretion of stellar-wind higher density clumps, of asteroids, comets and planets (Zubovas et al., 2012, and references therein), or of gas captured from transiently approaching objects. As mentioned above, searches for varying X-ray flare rates have been carried out in order to link the phenomenon to the known variations of the environment, like the periastron passages of the Gs gaseous objects (G1 in 2001, G2 in 2014) or of the closest approaches of the windy star S2 (2002, 2018). No firm conclusions were reached from these X-ray studies and, while no variations of the IR flaring rate were reported by Witzel et al. (2018), a burst of bright NIR flare rate was detected in 2019 with both Keck and VLT (§ I.E) and confirmed then by Weldon et al. (2023) who discussed the possible link to the G2 periastron passage. Considering that a variation of the accretion rate at the Bondi radius takes a while to produce repercussions in the inner accretion flow, since the estimated viscous timescale is of 5–10 years, it is difficult to directly link these possible rate variations to the original accretion event, but it is certainly worth to continue the search for such connections.

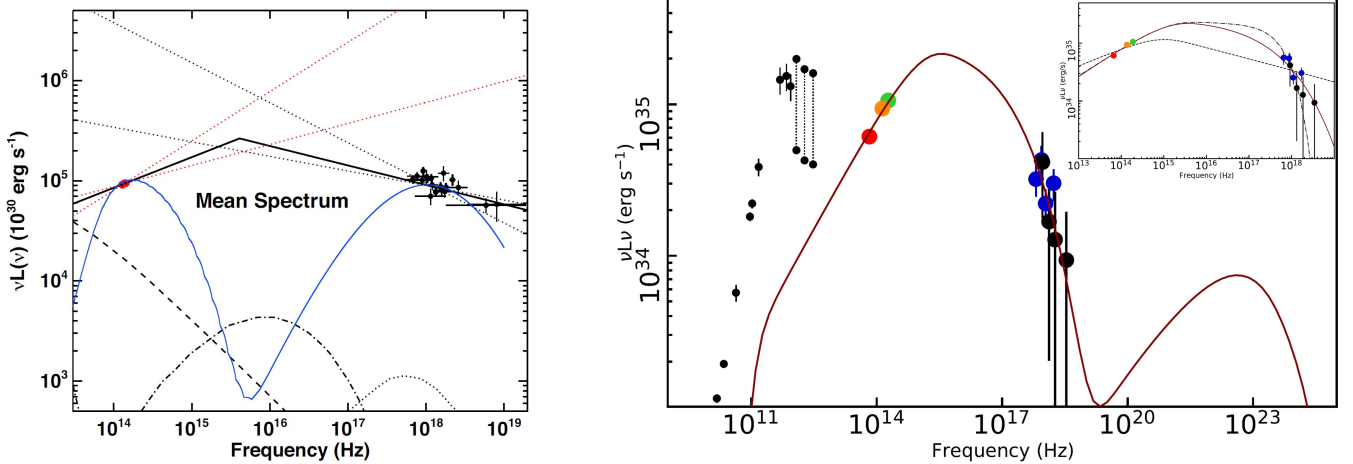


FIG. 11 The average SEDs of Sgr A*’s flares from successful multi-wavelength campaigns. Left: NIR and X-ray spectra of the 2014 flare observed with *XMM-Newton*, *NuSTAR* and VLT/SINFONI (from Ponti et al., 2017). The best fit SYN model with cooling break is shown (solid black line), with uncertainties in IR (red dotted) and X-ray (black dotted) slopes, along with the best-fit SSC model (thin solid blue line) and various IC components (others). Right: M/NIR and X-ray spectra of the 2019 flare observed with *Spitzer* (red point), VLT/GRAVITY (orange, green), *Chandra* (blue) and *NuSTAR* (black) (adapted from GRAVITY Collaboration et al., 2021). Fluxes (in luminosity units) are corrected for extinction and absorption. Some not-simultaneous radio to sub-mm fluxes (and variability ranges) of the quiescent emission are also indicated (small black points). The best fit SYN model (with cooling break and exponential cut-off) is plotted as solid brown line and includes the expected SSC component at gamma-ray energies (too low to be detected by *Fermi*). Inset panel shows a zoom on the IR/X-ray frequencies, with other tested models: SYN with break and no γ_{max} (dashed line), SYN with break and γ_{max} but sharp cutoff (dashed-dotted line).

C. X-rays and hard X-rays from the central 20 pc

1. Discrete X-ray sources

Several persistent X-ray sources are visible in the X-ray images of the central 20 pc (Baganoff et al., 2003; Maeda et al., 2002). Few weak objects are detected within 30'' from the BH (Fig. 7, left). The most interesting feature is certainly the cometary-shaped PWN also detected in radio as G359.95–0.04 only 10'' north from Sgr A*, which is a serious counterpart to the source of the TeV central emission (§ VI.A). Two other point-like sources have no stellar counterpart and were classified as weak XRBs.

A number of transient point-like sources have also been detected during the numerous observations of the GC with *Chandra*, *XMM-Newton* and the other observatories, particularly *Swift*, the most remarkable of which are certainly the 2004 transient (CXOGC J174540.0–290031, see Fig. 7 left) discovered at only 2'' from Sgr A* and seen to display microquasar-like radio jets (Muno et al., 2005b, and references therein) and the magnetar SGR J1745–2900, located 2.4'' from the SMBH, detected in outburst in 2013 (Kennea et al., 2013) and which is now back to quiescence. This cusp of X-ray transient sources will be discussed below along with the relevant source populations (§ IV.A).

On larger scales, more extended features include Sgr A East (§ III.C.2), hard X-ray sources (§ III.C.3) and also

another relevant X-ray jet feature detected with *Chandra*. This is the linear filament named G359.944–0.052, located about 20'' from Sgr A*, and aligned towards the BH in the S-E direction, which displays some peculiar spectral properties, no variability, and which has been proposed as a possible X-ray counterpart of a parsec-scale jet from Sgr A* (see Zhu et al., 2019, and references therein).

2. Sgr A East X-ray emission

A distinct bright thermal emission from a hot plasma with prominent lines of S, Ar, Ca, and Fe ions, appears coincident with the inner region of the non-thermal radio shell of the Sgr A East SNR (Fig. 12). First detected at low resolution with *ROSAT*, *ASCA* and *BeppeSAX* (Koyama et al., 1996; Sidoli & Mereghetti, 1999) Sgr A East was clearly resolved from the GC diffuse X-ray components with *Chandra* (Baganoff et al., 2003; Maeda et al., 2002) and then studied deeply (Park et al., 2005), also with *XMM-Newton* (Sakano et al., 2004) and *Suzaku* (Koyama et al., 2007b). With a total 2–10 keV luminosity of $8 \times 10^{34} \text{ erg s}^{-1}$, the SNR emission is rather soft and characterized by a two-temperature (1 keV and 5 keV) plasma with high metal abundance at the center of the radio shell and by one temperature (1.3 keV) plasma with solar abundances in the external northern part. This has been interpreted as emission dominated by stellar ejecta

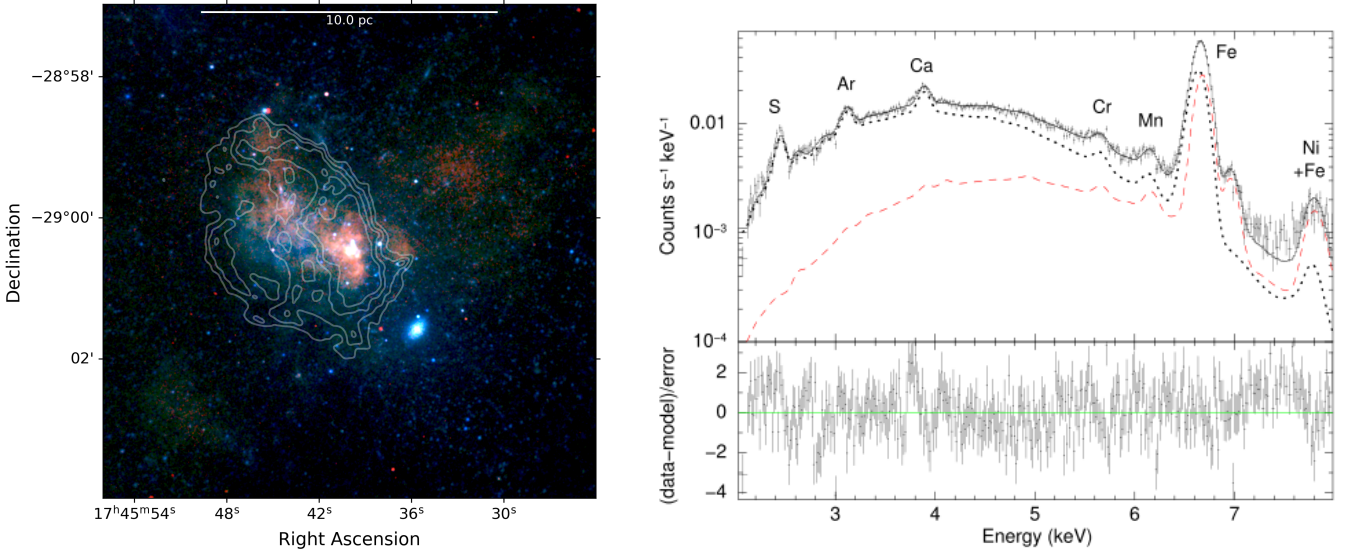


FIG. 12 Left: *Chandra* 3-color X-ray image of Sgr A East (red: 1.5–2.6 keV, green: 2.6–4.5 keV and blue 4–5–7.5 keV) with the 6 cm MeerKAT radio contours of its radio shell overlaid. The hot thermal emission fills the interior of the radio shell. The Cannonball is visible on the northern part of the shell. Right: The X-ray spectrum of Sgr A East central part with the best-fit thermal models (from Zhou et al., 2021).

heated by a reverse shock in the center and by hot swept up ISM close to the shell. Sgr A East was then classified as a single metal-rich mixed-morphology rest of a core collapse SN of a $< 20 M_{\odot}$ star 2–4 pc behind Sgr A*. The SN was thought to have occurred about 10 kyr ago, releasing about 5×10^{50} erg and possibly leaving behind the high-velocity neutron star (NS) remnant, now seen as the X-ray (Park et al., 2005) and radio PWN known as the Cannonball, just outside the north side of the radio shell.

However, since the recent detection of Mn, Ni and Cr lines with *Suzaku* (Ono et al., 2019), a younger (1–2 kyr) event, possibly even due to a thermonuclear white dwarf (WD) deflagration of a type Iax SN, has been considered as origin of the remnant (Zhou et al., 2021), in order to explain the *Chandra* X-ray feature the ridge, at the edge of the central cavity, as due to the interaction of the SNR ejecta and the stellar-wind outflow from the YNC (Zhang et al., 2023). In this model the Cannonball is not the NS remnant of the SN, the central plasma is not due to ejecta heated by conventional collisional ionization of the SNR reverse shock (that needs more than 2 kyr to develop) but rather a recombination plasma, photo-ionized by a large outburst of Sgr A* in the past (Ono et al., 2019).

Whatever the type and age of the original SN, Sgr A East is a very important object in the HE phenomena context given its unique position close to the SMBH. Note that recent modelling of the SNR and its interaction with the GC environment (Zhang et al., 2023) does not support the initial hypothesis that it may have caused a large rise in the BH mass accretion several centuries ago as the swept-up dense material passed through

Sgr A*, and does not explain either the present BH starving due to the ISM having been cleared out from its vicinity. Its interaction with the 50 km s⁻¹ cloud and, towards the center, with the CND and even with the YNC stellar-wind outflow can lead to prominent CR acceleration and production of gamma-ray emission by their subsequent interaction with the molecular material. Very recently *XRISM* has confirmed the presence of over-ionized plasma within Sgr A East, interpreted as due to a past outburst of Sgr A* (*XRISM* Collaboration et al., 2025). A conclusive interpretation of the Sgr A East SNR is therefore still to be drawn, and may benefit from future high-spectral resolution X-ray telescopes with higher angular resolution (§ II.D).

3. The central hard X-ray sources

In hard X-rays, the *INTEGRAL* surveys revealed a significant central ($R < 20$ pc) emission, extending up to > 100 keV, compatible with the 12' FWHM PSF of the IBIS instrument, centered at only 1' from Sgr A* (Bélanger et al., 2004, 2006a), but clearly too bright to be compatible with the extension of the Sgr A* spectrum at high energies. The nature of this source (IGR J17456–2901) was clarified by *NuSTAR* (Mori et al., 2015), which could unambiguously identify its harder emission with the central PWN G359.95–0.04 detected by *Chandra* (discussed in § VI.A) and the softer one (predominant in the 20–40 keV band) with a diffuse emission that the authors attributed to an unresolved population of magnetic cataclysmic variables (mCV) (Perez et al., 2015,

see also § V.A), as initially suggested by Krivonos et al. (2007). Above 10 keV, *NuSTAR* did not find non-thermal X-rays from Sgr A East but could detect, in addition to the Sgr A* flares mentioned above, few other hard X-ray features in the central 10 pc, none attributed to PWNe. G359.97–0.038 detected up to 40 keV, is located just outside the Sgr A East shell, close to the Plume and it is probably illuminated by non-thermal bremsstrahlung or inverse Compton processes of electrons originated by the interaction between the shell and the 50 km s^{−1} cloud (Nynka et al., 2015). Another filament appears associated to a radio feature (G359.89–0.08) and was attributed to synchrotron emission from ≈ 100 TeV electrons trapped in magnetic flux tubes, which could be generated by the interaction of relativistic protons accelerated by Sgr A* or by the Sgr A East SNR with the nearby 20 km s^{−1} cloud (Zhang et al., 2014). Other non-thermal features discovered with the *NuSTAR* GC survey outside the Sgr A complex are discussed below (§ IV.B).

IV. X-RAY SOURCE POPULATIONS AND DISCRETE STRUCTURES IN THE CMZ

Typical X-ray point-like sources detectable at a distance of 8 kpc and under strong absorption are accretion-powered systems, including white dwarfs, neutron stars or black holes, which are tracers of the old stellar population but with open questions on the specificity of the compact remnant population at the GC (§ IV.A). Part of these compact sources and other energetic phenomena also accelerate particles that are responsible for more extended features detected in X-rays (§ IV.B). In addition, massive stars with strong winds, such as WR or O-stars, tracing recent star formation processes, can also be detected as X-ray point sources and be associated with extended high-energy thermal emission (§ IV.C).

A. The CMZ populations of point-like X-ray sources

In the inner region of our Galaxy, the X-ray point source distribution follows the stellar population seen in the near-infrared. The highest density is measured towards the central few parsecs, where the contribution from the nuclear star cluster dominates, and smoothly decreases outwards, following the more-extended nuclear disk component (see Hong et al., 2009; Muno et al., 2006; Zhu et al., 2018, and Fig. 13). The majority of these sources are persistent and most likely associated with a population of magnetic cataclysmic variables (mCVs, § IV.A.1). Known transients reveal a sparser population of X-ray binaries (§ IV.A.2), and rarer classes of point sources may be part of additional populations that remain to be constrained (§ IV.A.3).

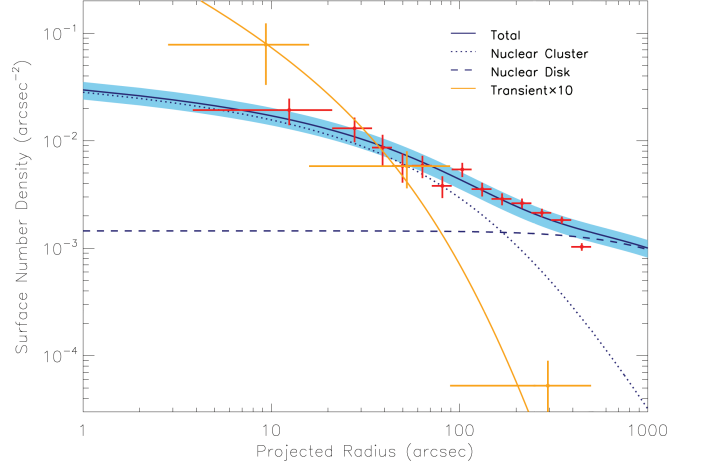


FIG. 13 Surface density profile of X-ray sources with a luminosity $L_{2-10\text{keV}} \gtrsim 6 \times 10^{31} \text{ erg s}^{-1}$ in the inner 40 pc of our Galaxy (in red), tracing a population of mCVs. The best fit model derived from the stellar mass distribution (solid blue line, and uncertainties in shaded blue) includes the contributions from the nuclear star cluster (dotted line) and from the nuclear disk (dashed line). The surface density profile of known transients (multiplied by 10, in orange), tracing a population of quiescent LMXB, appears much steeper than the stellar distribution. Figure adapted from Zhu et al. (2018).

1. Magnetic cataclysmic variables

Existing deep *Chandra* observations covering the CMZ revealed close to 10,000 point sources within this region (after excluding foreground sources, Muno et al., 2009; Zhu et al., 2018). The X-ray information available for the vast majority of these objects is insufficient to classify them individually, but their statistical and cumulative properties support the identification of a large fraction of these sources as intermediate polars (IPs), a subclass of magnetic CVs, i.e. white dwarfs accreting from a low-mass companion (for a review on the X-ray properties of these objects, see Mukai, 2017). Indeed, most of the X-ray point sources detected in the CMZ have a 2–10 keV luminosity between 10^{31} and $10^{34} \text{ erg s}^{-1}$, and do not exhibit strong variability on either short or long timescales (less than 15% of the sources were detected as significantly variable, Muno et al., 2009; Zhu et al., 2018). Among them, few sources do have periodic variability detected, with time periods compatible with typical IP spin periods (e.g. Muno et al., 2003). The surface density of persistent sources follows the stellar mass traced by the near-infrared starlight (see Fig. 13) with a ratio compatible with the abundance of mCVs in the solar neighborhood, supporting the identification of a large fraction of these sources as mCVs.

Their cumulative spectrum reveals a hard continuum and prominent iron emission lines at 6.4 (Fe K α), 6.7 (Fe XXV He α) and 7.0 keV (Fe XXVI Ly α), which are also typical of mCVs (e.g. Xu et al., 2016). Further inves-

tigation for the X-ray sources overlapping the NSC in the central 20 pc demonstrates that the equivalent width of the lines and their flux ratio are different for sources above and below $L_{2-10\text{keV}} = 6 \times 10^{31} \text{ erg s}^{-1}$. Above this threshold, the properties of the cumulative spectrum is fully compatible with what is expected for IPs while a larger fraction of non-magnetic CVs, namely dwarf novae, may be present among fainter sources.

Contribution from populations of sources with no Fe XXV emission line (i.e. other than CVs and coronally active binaries, ABs) should affect the value of the equivalent widths measured in the cumulative spectra, and therefore cannot exceed few percents of the total amount of persistent sources detected in the 2–10 keV range (see also § IV.A.2). Above 10 keV, only the brightest part of these populations have been detected, with few dozens of sources resolved by *NuSTAR* (Hong et al., 2016). IPs likely contribute to at least 40–60% of this bright hard subsample, along with a possibly higher fraction of X-ray binaries (see § IV.A.2). The faintest part of the CV population is yet to be resolved and likely contributes to several components of diffuse hard X-ray emission detected at various spatial scales around the Galactic center (see § V.A).

2. Low mass X-ray binaries

A population of X-ray binaries at the Galactic center is expected from stellar evolution and stellar dynamics, and should be strongly linked to the total number of NS and BH present in these inner regions. The XRB population has primarily been detected through a few bright persistent sources and dozens of X-ray outbursts. Across the CMZ, about twenty five transients reaching luminosities $L_{2-10\text{keV}} \gtrsim 10^{34} \text{ erg s}^{-1}$ have been identified. Most of them are located in the central 50 pc and have been closely monitored by *Swift*/XRT starting from 2006 (Degenaar et al., 2015; Muno et al., 2009, see also § II.B), which now provides the complete sample of all transients from this region having recurrence times below fifteen years. Their radial distribution is different from the bulk of mCVs described previously (see Fig. 13). It is steeper and consistent with an overabundance in the central parsec, suggesting an important role of dynamics (through mass segregation and stellar capture) in the formation of, at least, part of these systems (Muno et al., 2005b; Zhu et al., 2018).

Sources reaching luminosities above $10^{36} \text{ erg s}^{-1}$ with outbursts lasting for several months have been classified as low mass X-ray binaries (LMXBs), i.e. NS or BH accreting from a low-mass stellar companion (for a review on the properties and demographic of these systems, see Sazonov et al., 2020). The GC *Swift*/XRT monitoring also revealed very faint X-ray binaries (VFXB) that have outbursts lasting less than about a month with luminosi-

ties in the $10^{34-36} \text{ erg s}^{-1}$ range, and recurrence times similar to the ones of brighter LMXBs (Bahramian & Degenaar, 2023). They likely constitute an inhomogeneous subclass of LMXBs in which the accretion is limited, due to e.g. a small accretion disk, a high magnetic field or wind-feeding (Degenaar et al., 2015, and references therein). However, the high extinction towards the CMZ makes it hard to further classify these faint GC transients. Among all bright or faint and persistent or transient sources, NS-LMXBs have been securely identified through the detection of type I X-ray bursts or of coherent pulsations (see e.g. Degenaar et al., 2012). The identification of BH-LMXBs is not as straightforward but few BH candidates have also been proposed (see e.g. Mori et al., 2019; Muno et al., 2005a).

In quiescence, LMXBs may be detected as very faint non-thermal point sources. Investigation of the spectral properties of *Chandra* sources close to the supermassive black hole revealed twelve point sources with power-law like spectra ($\Gamma \sim 2$, and no iron emission lines) in the central parsecs, contrasting with both the spatial distribution and the spectral properties of mCVs (Hailey et al., 2018; Mori et al., 2021). None of these sources has ever been detected in outburst but several of them show moderate long term variability. Their exact classification has been debated. They are presented as most likely BH-LMXBs (Mori et al., 2021) but NS-LMXB with recurrence time longer than the ones that have been observed at the GC so far, or millisecond pulsars (MSP), cannot be ruled out for at least part of these systems.

Mass segregation around SMBHs predicts the high density of massive compact remnants in the inner regions traced by detected LMXB. However, the number of NS- and BH-XRBs could be altered with respect to isolated ones, by e.g. SN kicks (Bortolas et al., 2017) or 3-body encounters (Generozov et al., 2018), leaving important uncertainties on the extrapolations that can be done from the observations. Current predictions state that more than a hundred of BH-LMXB could be present in the central parsec, together with thousands of isolated BHs (Mori et al., 2021, and references therein), while the population of NSs should be also closely related to the population of pulsars (see § IV.A.3).

3. More elusive pulsar populations

One X-ray transient, SGR J1745–2900, detected within 0.1 pc from Sgr A* was not classified as a LMXB but as a magnetar (Mori et al., 2013; Rea et al., 2013), i.e. an isolated neutron star powered by a very strong magnetic field (see Mereghetti et al., 2015, for a review on magnetars). This source went into outburst in 2013, reaching an X-ray luminosity of few $10^{35} \text{ erg s}^{-1}$, followed by a slow exponential decay over several years (Rea et al., 2020). The NS has a spin period of $\sim 3.76 \text{ s}$ detected both in

X-ray and in radio (Mori et al., 2013; Shannon & Johnston, 2013). Its dispersion measure is the highest ever measured towards a pulsar, $DM = 1778 \pm 3 \text{ cm}^{-3} \text{ pc}$, and together with its high rotation measure is indicative of a strong magnetic field in its surrounding medium, $B \gtrsim 50 \mu\text{G}$ or higher (see discussion by Eatough et al., 2013). This makes it the first X-ray pulsar unambiguously identified close to Sgr A*⁶. Since magnetars are relatively rare, this finding could be consistent with former predictions of a large population of pulsars around Sgr A* (Pfahl & Loeb, 2004) and, on larger scale, across the CMZ (Spitler et al., 2014; Wharton et al., 2012, see also § VI.D). The objects with large spin-down powers are expected to emit in X-rays and could account for a small fraction of unidentified X-ray point sources (Berteaud et al., 2021; Possenti et al., 2002). The detection of their spin would be the definitive proof of their existence. However, due to the scattering of radio waves off the dense interstellar medium, extensive radio pulsation searches have only revealed a handful of long period pulsars (Deneva et al., 2009; Johnston et al., 2006; Wong-puechauxsorn et al., 2024) and one MSP (Lower et al., 2024) in the CMZ (distance estimates based on dispersion measures). Only one of them, PSR J1747–2809, has a counterpart identified in X-ray (see § VI.B.1). Across the CMZ, additional extended X-ray features, such as PWNe, are further hints of the presence of X-ray emitting pulsars within the GC environment (see § IV.B).

B. Filaments and pulsar wind nebulae

High spatial resolution X-ray observations of the CMZ revealed a total of about thirty elongated features, with lengths of the order of 1 pc or more, referred to as X-ray filaments (see the review by Koyama, 2018, for the most complete list of known filaments in the central $1^\circ \times 0.5^\circ$)⁷. Most of the known X-ray filaments are located within 12 pc from Sgr A*, possibly due to the highest exposure available towards this inner region (Johnson et al., 2009; Koyama, 2018, see also § III.C).

Their exact morphology varies from one filament to the other, in terms of length, width, curvature and flux gradients. Several works have highlighted the cometary shape of a significant fraction of these filaments, part of them even having a point source (often called the head) associated with their extended emission (their tail, see

e.g. Johnson et al., 2009; Lu et al., 2008). The majority of known X-ray filaments has spectral properties consistent with a non-thermal emission best fit by an absorbed power-law with $\Gamma \sim 1\text{--}3$ and a total 2–8 keV luminosity within $10^{32}\text{--}10^{34} \text{ erg s}^{-1}$ (Johnson et al., 2009; Lu et al., 2008; Muno et al., 2008). Four of them have also been detected above 10 keV by *NuSTAR* (Mori et al., 2015), including two that also coincide with gamma-ray sources (see § VI.B). Despite their resemblance to the numerous non-thermal radio filaments, which are explained by the synchrotron radiation of GeV electrons trapped by enhanced magnetic features close to the Galactic center (e.g. Heywood et al., 2022, see also Fig. 3), only a handful of X-ray filaments have radio counterparts (e.g. Lu et al., 2003; Muno et al., 2008; Ponti et al., 2015b).

The origins of the non-thermal X-ray filaments are diverse. The properties listed above are fully consistent with the ones of PWNe (see Gaensler & Slane, 2006; Kargaltsev et al., 2017, for a review) having filamentary-like structures due either to the motion of the young pulsars or to strong magnetic field in their environment. In agreement with the massive star formation rate, it has been proposed that a large fraction (~ 20 out of the 34 X-ray filament detected within 20 pc of Sgr A*) of the non-thermal X-ray filaments could be PWNe (Johnson et al., 2009; Lu et al., 2008; Muno et al., 2008). However, no pulsation detection ever proved the presence of a pulsar in any of these sources (see also § IV.A.3)⁸. Among the most secured PWNe identifications are G0.13–0.11 (Churazov et al., 2024; Zhang et al., 2020) and G359.95–0.04 (Mori et al., 2015; Wang et al., 2006b), which will be discussed along with their possible gamma-ray emission in § VI.B, and the Cannonball (Nynka et al., 2013; Park et al., 2005) already mentioned in § III.C. Other mechanisms can provide similar X-ray signatures. One example is the interaction of SNRs with surrounding molecular clouds, which has been proposed for one filament close to Sgr A East (Nynka et al., 2015, see also § III.C). A second example is the interaction of TeV electrons with magnetic structures (similar to radio NTF), which has been proposed for few filaments, such as Sgr A-E (e.g. Zhang et al., 2014). In addition, several elongated features close to Sgr A* could also be linked to the supermassive black hole activity (see § III.C).

Finally, thermal spectra including a 6.7 keV emission line have also been reported for at least one X-ray filament. Ram-pressure or magnetic field confined stellar winds from massive stars could explain such thermal structures (see e.g. Johnson et al., 2009).

⁶ There may be additional pulsars within identified NS-LMXB (see § IV.A.2). GRO J1744–28 is currently the only known pulsating NS-LMXB towards the GC, but its LoS distance has been debated (Degenaar et al., 2012; Doroshenko et al., 2020; Sanna et al., 2017).

⁷ Additional filaments, characterized by a strong 6.4 keV emission line, are also detected. They are ignored through this section and will be discussed in § V.C.

⁸ PSR J1747–2809 (see § VI.B.1) is the only exception but it is outside of the central $1^\circ \times 0.5^\circ$ considered by filament studies discussed in this Section.

C. Massive stars and star clusters

Star formation occurring within the CMZ (see § I.C.3) sustains the presence of numerous massive stars, namely Wolf Rayet and O supergiants, characterized by fast stellar winds. When colliding, these winds can produce a harder thermal emission than their parent star and be detected in X-rays despite the Galactic center strong LoS absorption (see Rauw & Nazé, 2016, for a review on the X-ray emission from interacting wind massive binaries).

At the Galactic center, the most obvious signatures of these high-energy processes are the three young and massive stellar clusters: the Arches, the Quintuplet and the YNC clusters (their main characteristics are given in § I.C.3). The Arches and Quintuplet clusters have been resolved by *Chandra* into a collection of point sources (4 and 5, respectively, if ignoring one foreground source for the Quintuplet cluster) together with an extended diffuse emission (Law & Yusef-Zadeh, 2004; Tsujimoto et al., 2007; Wang et al., 2006a; Yusef-Zadeh et al., 2002b). The spectral shapes of the point sources are consistent with emanating from a hot diffuse gas having a twice-solar abundance and temperatures ranging from $kT \sim 2$ keV to ~ 9 keV, together with large foreground absorption. The brightest of these sources is within the core of the Arches cluster and has a luminosity $L_{0.3-8\text{keV}} \sim 10^{34}$ erg s $^{-1}$ (e.g. Wang et al., 2006a). As several other X-ray point sources across the CMZ (~ 30 in total), the NIR counterpart of the cluster point sources has been identified as WR or O supergiants (Mauerhan et al., 2010, and references therein). Because isolated such massive stars cannot produce the X-ray emission detected, these sources have instead been classified as likely colliding wind binaries (these X-ray sources would represent less than about 5% of the massive star content of these clusters, see e.g. Mauerhan et al., 2010; Wang et al., 2006a). This type of source could also explain the 70% X-ray flux enhancement of at least 4 days detected towards the Arches cluster in 2007 (Capelli et al., 2011).

In the Arches and Quintuplet clusters, the diffuse emissions has a thermal⁹ origin with a strong 6.7 keV emission line and temperatures consistent with their point source contents (e.g. Law & Yusef-Zadeh, 2004; Tsujimoto et al., 2007; Wang et al., 2006a; Yusef-Zadeh et al., 2002b). The winds from all massive stars present in these two massive young clusters can also be responsible for, at least, a significant part of the diffuse thermal emission detected (Wang et al., 2006a). However, collective emission of point sources below the detection threshold should also contribute. This likely includes fainter colliding wind binaries, as well as young stellar objects. X-ray

emitting young stellar objects are tracing the young low-mass stars ($0.3\text{--}3 M_{\odot}$, Feigelson et al., 2005) and the clusters' diffuse emission can be used to put constraints on these lighter populations and thereby on their stellar initial mass function (IMF). These studies highlight a deficit of X-ray diffuse emission compared with what would be expected from a standard IMF, in all GC clusters, including the YNC (Nayakshin & Sunyaev, 2005; Wang et al., 2006a). In agreement with other works focusing on the stellar populations detected at lower wavelengths, this has been interpreted as a top-heavy IMF, i.e. an overabundance of massive stars in the main clusters of the CMZ (see also Hosek et al., 2019; Hußmann et al., 2012; Paumard et al., 2006), which could be due to physical and dynamical properties of the CMZ (Chabrier & Dumond, 2024).

Across the CMZ, close to 100 massive stars are known, including ~ 30 with an X-ray counterpart (Clark et al., 2021; Mauerhan et al., 2010). Most of them are in apparent isolation. However, stellar clusters could be responsible for part of these isolated massive stars over a significant fraction of the CMZ, due to their proper motion, Supernovae kicks and tidal stripping from the CMZ dense environment (e.g. Clark et al., 2021; Habibi et al., 2014). While colliding wind binaries have been the favored scenario to explain the X-ray counterpart from these massive stars, quiescent high mass X-ray binaries could also account for few of these sources and possibly many more below the detection threshold of current X-ray surveys.

Through their winds and violent death as Supernovae and the plausible subsequent CR accelerations, these massive stars contribute to the energetics of the central regions. Constraints on the SN rate and the high-energy properties of the SNR detected within the CMZ will be discussed in § V.B, while their link with gamma-ray emission is presented in § VI.

V. DIFFUSE X-RAY EMISSION FROM THE CMZ AND BEYOND

The Galactic ridge X-ray emission (GRXE, see also § II.A) is characterized by a two-temperature plasma (see e.g. Kaneda et al., 1997; Yamauchi et al., 1996), a softer component with a temperature of about 0.8 keV and a hotter component of 7 keV. The softer component is understood as being caused by interstellar gas shocked by supernova remnants and stellar winds (Kaneda et al., 1997, § V.B). The hotter component is understood as being caused by the cumulative emission of faint unresolved sources. In the GC, the X-ray diffuse emission has different characteristics. An excess of the hot component peaking at the center is observed and it has been proposed to be caused by a genuine gravitationally unbound plasma (§ V.A). Additionally, a non-thermal component

⁹ The large-scale non-thermal emission reported in these works for the Arches cluster is now associated with the past activity of Sgr A*, see § V.C.

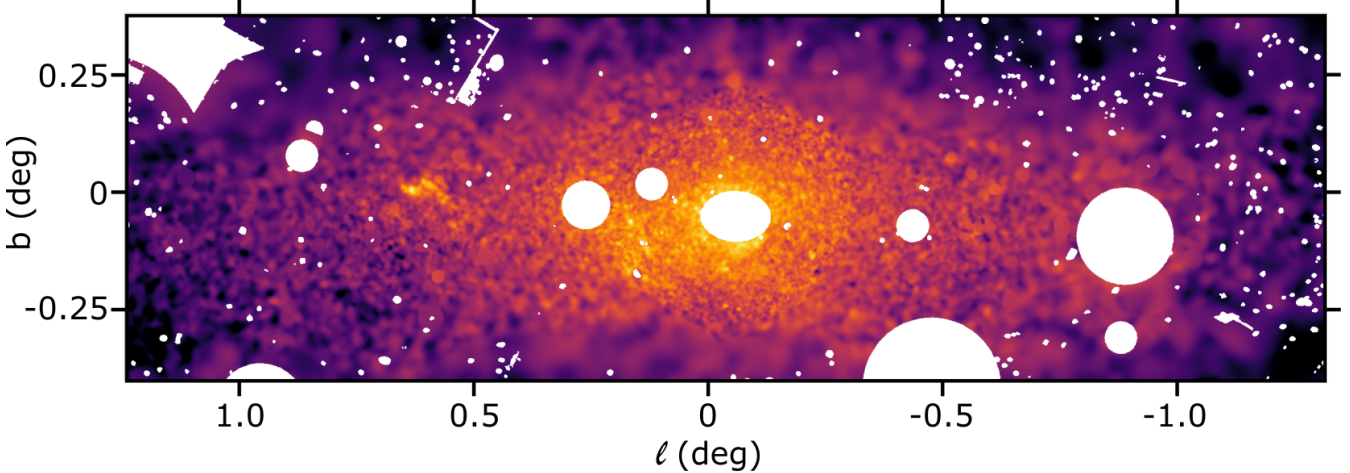


FIG. 14 Hot thermal emission detected by *XMM-Newton* within the CMZ. The color highlights the surface brightness of the signal detected in the 6.62–6.80 keV band in logarithmic scale, after correction for contamination from non-thermal emission estimated from the 6.3–6.5 keV band. An adaptive smoothing has been applied to the mosaic and regions around bright sources have been excluded to avoid contamination (in white). Figure slightly adapted from Anastasopoulou et al. (2023).

extending in the hard X-ray range with a prominent neutral iron $K\alpha$ line is observed from ISM gas clouds in the CMZ. This emission is time variable and attributed to illumination by a bright past outburst of Sgr A* (§ V.C). The contribution of low-energy CRs to this emission has been debated. While, other tracers such as H_3^+ indicate a larger density in the CMZ than in the rest of the Galactic disk, it does not seem sufficient to represent a large fraction of the apparently steady emission (§ V.D).

A. The hard diffuse component: very hot plasma or unresolved point sources?

Among the diffuse emissions detected towards the CMZ, there is a hot thermal component, having a temperature of $kT \sim 7$ keV, traced by a strong Fe XXV He α and Fe XXVI Ly α emission lines at 6.7 and 6.97 keV (see Fig. 15). This hot component peaks at the GC and smoothly decreases outwards (see Fig. 14), connecting to the bulge diffuse emission at higher latitudes and to the ridge one at larger longitudes. Its emission is largely accounted for by the populations of unresolved X-ray sources and can therefore be used to study the cumulative properties of these sources (§ V.A.1). The origin of the excess emission relative to the estimation of the unresolved point source contribution has been debated and could originate from an extended hot plasma (§ V.A.2).

1. Populations of unresolved point sources

The large-scale morphology of the hot thermal component follows the stellar mass traced by NIR light, with a flux ratio compatible with the local one (Anastasopoulou et al., 2023; Revnivtsev et al., 2006). Towards

the bulge, more than 80% of the 6.7 keV emission has been resolved into point sources and the remaining signal is likely attributed to the X-ray point sources that are below the sensitivity limit of *Chandra* deepest observations (Revnivtsev et al., 2009). Resolved sources include mCVs, which were initially thought to be the dominant contributor to the diffuse emission (see e.g. Hong, 2012; Krivonos et al., 2007; Yuasa et al., 2012). However, further investigation of the bulge component by *Suzaku* and *NuSTAR* allowed to better constrain the cumulative spectrum of these sources, including the EW of its iron emission lines (Nobukawa et al., 2016) and its average temperature ($kT \sim 8$ keV, Perez et al., 2019), challenging previous interpretations. These results are instead fully consistent with a population dominated by dwarf novae (see also Reis et al., 2013; Xu et al., 2016).

Towards the Galactic center, harder emission and stronger EWs are detected. In the inner 10 pc, *NuSTAR* revealed an unresolved hard X-ray emission possibly associated with the NSC, strongly peaked towards the center, with a hard X-ray luminosity $L_{20-40\text{keV}} \sim 2 \times 10^{34} \text{ erg s}^{-1}$ and a Bremsstrahlung temperature above 35 keV (Perez et al., 2015). This hard emission has been attributed to a population of IPs with WD masses $M_{\text{WD}} \gtrsim 0.8 M_{\odot}$ (Hailey et al., 2016; Xu et al., 2019). These unresolved IPs would be similar to the ones detected as individual sources by *NuSTAR* across the CMZ (Hong et al., 2016, see also § IV.A.1) and consistent with the average WD mass measured by the Sloan Digital Sky Survey (Zorotovic et al., 2011). The fraction of IPs likely decreases outwards, together with a relative increase of non-mCVs, which could explain why large-scale spectral analyses including the CMZ or adjacent regions detected significantly harder emission than in the bulge, and initially hinted towards a single population of less massive

IPs rather than dwarf novae (Krivonos et al., 2007; Yuasa et al., 2012). However, combining populations of mCVs, non-mCVs and ABs still fails to reproduce the EWs detected towards the CMZ, which may indicate different source properties or contamination by truly diffuse components (see § V.A.2).

2. Constraints on the contribution from a hot plasma

The normalization factors derived for the bulge/ridge to explain the level of 6.7 keV emission from the stellar mass distribution (SMD) models have failed to reproduce the strong 6.7 keV emission from the Galactic center, providing evidence for a significant excess within $|l| \lesssim 1^\circ$ and $|b| \lesssim 0.25^\circ$ (e.g. Anastasopoulou et al., 2023; Uchiyama et al., 2011). The precise description of this excess depends on the analyses performed and the SMD model used. The bulk of this excess has the same profile as the SMD but with normalisation ratios ranging from 1.3–1.5 for the most recent estimations (Anastasopoulou et al., 2023) up to values $\gtrsim 2$ for previous works (Heard & Warwick, 2013a; Nakashima et al., 2013; Yasui et al., 2015, and references therein) and a significant increase towards the NSC, as well as local enhancements towards known point and extended sources such as XRBs, SNRs and stellar clusters (see also Fig. 14).

There is no consensus on the nature of this emission. The precise description of the 6.7 and 6.97 keV emission lines (i.e. their exact energy, flux ratios, and EWs) has been interpreted by several studies as due to a truly diffuse optically thin thermal plasma close to collisional ionization equilibrium, with a temperature ~ 7 keV (Koyama et al., 2007a, 2009; Uchiyama et al., 2013; Yamauchi et al., 2009, 2016). Such a hot plasma would not be gravitationally bound and would escape the central region within few 10^4 yr, requiring either a huge energy input to sustain it or a confinement mechanism to maintain it. A large-scale toroidal magnetic field within the CMZ, as suggested by NIR polarimetric results, could provide sufficient pressure support to relax the energetic problem by maintaining the hot plasma over its 10^7 – 10^8 yr radiative-cooling timescale (see Nishiyama et al., 2013, and references therein). In terms of heating, possible contributions from SN explosions, violent past activity from Sgr A* or magnetic reconnection have all been discussed, along with their respective limitations to reach a thermal energy of $\sim 10^{53}$ erg and a temperature of ~ 7 keV (see e.g. Anastasopoulou et al., 2023; Koyama, 2018; Nishiyama et al., 2013; Uchiyama et al., 2013).

Other studies have pointed to the close morphological correspondence between the region covered by the excess and the NSD, and argue that it could be entirely due to unresolved point sources. In this case, the X-ray enhancement could be explained by a modification in the underlying source populations, higher metallicity

or an improper modeling of the stellar mass in these inner regions (Anastasopoulou et al., 2023; Heard & Warwick, 2013a). Unlike the large-scale hot plasma scenario, this point source interpretation would also be compatible with the warm diffuse gas with a large filling-factor reported by Oka et al. (2019, see also § V.D). However, this would not rule out the possibility of having smaller scale plasma components contributing to local 6.7 keV enhancements, including softer components with $kT \sim 1.5$ keV, which are also detected towards the CMZ (Heard & Warwick, 2013a, see also § V.B).

B. The soft plasma component: hot plasma bubbles, loops and chimneys

Contrary to the hot plasma, the soft plasma component pervading the inner 300 pc is unambiguously a truly diffuse but structured and patchy emission (Muno et al., 2004; Wang et al., 2002a). It is characterized by a number of strong helium-like and hydrogenoid lines of Sulfur, Silicium and Calcium. The brightest one is the S XV He α at 2.46 keV (see Fig. 15). They trace a plasma distribution with typical temperatures of about 0.7–1.0 keV (Kaneda et al., 1997; Muno et al., 2004) and densities of about 0.7–0.1 cm $^{-3}$.

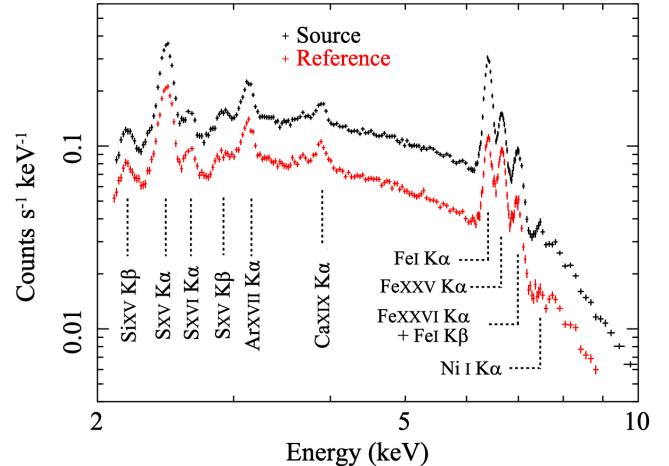


FIG. 15 *Suzaku* spectra of various soft plasma emitting regions in the CMZ (see Nobukawa et al., 2010, for more details). The more prominent lines from the soft plasma component are S XV at 2.46 keV, Si XIII at 1.86 keV (not shown), Ar XVII at ~ 3.12 keV and Ca XIX at ~ 3.9 keV. The neutral Fe K α line at 6.4 keV and the helium-like Fe XXV line at 6.7 keV, associated with other diffuse components, are also visible. Figure adapted from Nobukawa et al. (2010).

While the soft plasma was initially identified with *ASCA*, subsequent surveys of the GC region by *Chandra* (Wang, 2021; Wang et al., 2002a), *XMM-Newton* (Ponti et al., 2015b; Sakano et al., 2003) and *Suzaku* (Koyama et al., 2007a; Yamauchi et al., 2018) have resolved various localized features. The spatial distribu-

tion of the soft plasma emission is indeed highly non-uniform as visible from Fig. 16. In the inner 20 pc, *Chandra* observations reveal brightness variations between $(0.2 - 1.8) \times 10^{-13}$ erg cm $^{-2}$ s $^{-1}$. Correcting for absorption, Muno et al. (2004) finds bolometric luminosities of the soft plasma ranging from 0.6 to 9×10^{34} erg s $^{-1}$ within the inner 20 pc.

Similarly to the soft X-ray plasma component observed in the GRXE, the GC soft plasma is likely heated by supernovae shocks and by winds of massive stars. Energetically, the radiative cooling rate of the soft plasma within the inner 20 pc of the Galaxy could be balanced by 1% of the kinetic energy of one supernova every 3×10^5 yr. *XMM-Newton* X-ray survey reveals about 10–12 supernova remnants candidates through their thermal emission, implying a supernova rate as large as $0.3 - 1.5 \times 10^{-3}$ yr $^{-1}$ in the CMZ (Ponti et al., 2015b).

In the following, we discuss a few specific features. For in depth reviews of these features and overall emission, we refer the reader to Ponti et al. (2015b) and Koyama (2018).

1. A ring-like superbubble southwest of Sgr A*

Mori et al. (2009) discovered two soft plasma features, G359.77–0.09 and G359.79–026 with *Suzaku*, with absorption column densities consistent with the GC distance and ionization timescales of ~ 30 kyr. *XMM-Newton* observations by Heard & Warwick (2013b) confirmed the characteristics of these features. Mori et al. (2009) and Heard & Warwick (2013b) have both proposed that they are physically connected and part of an apparent elliptical structure centered on $l \sim 359.9^\circ$ and $b \sim -0.125^\circ$ with minor and major axes of 18 and 28 pc at the GC distance. Ponti et al. (2015b) observed that S XV emission fills the elliptical structure showing it is the projection of a large shell of hot gas. The total thermal energy of the structure is estimated to be $\sim 10^{51}$ erg, which is too large for a single regular supernova remnant (Heard & Warwick, 2013b; Mori et al., 2009). It could have been energized by supernova explosions from a collection of massive stars. Several massive stars escaped from the Quintuplet cluster are indeed found in the region (Habibi et al., 2014) and could be plausible progenitors (Ponti et al., 2015b). Another alternative origin is a single very energetic event. Sgr A* being in projection inside the ellipse, the shell could have been produced by an unbound remnant of a stellar capture by the SMBH (a tidal disruption event or TDE) occurring in the last 30 kyr (Ponti et al., 2015b). The expected recurrence time of TDEs in the GC is in the range of 10–100 kyr (Alexander, 2005; Merritt, 2010), making the existence of such remnant today plausible. This mechanism could release energies up to 10^{52} erg (Khokhlov & Melia, 1996), large enough to power the superbubble, although more recent

studies suggest unbound debris might have lower kinetic energies of about 10^{50} erg (Guillochon et al., 2016).

2. The Radio Arc bubble

A very bright region of soft X-ray emission is visible around $l \sim 0.1^\circ$ and $b \sim -0.1^\circ$ (see Fig. 16). This region is located between the Sgr A complex and the Radio Arc, overlapping the Radio Arc bubble, a large mid-IR shell (Levine et al., 1999). The bubble has a 23 pc (10') diameter and encompasses the Quintuplet cluster (Simpson et al., 2007). Figer et al. (1999) has proposed the IR shell to be caused by winds from the cluster massive stars. Rodríguez-Fernández et al. (2001) noted that the arc bubble is filled with continuum X-ray emission measured with *ASCA* which they assumed could be due to a population of sources. With deep *XMM-Newton* observations, Ponti et al. (2015b) observed that the bright soft plasma X-ray emission in the region extends over 7' and completely fills the Radio Arc bubble. The total thermal energy of the X-ray plasma inside the arc bubble could be as large as 1.5×10^{51} erg requiring multiple supernova events to energize it. The emission is not uniform with several cavities possibly due to different explosion events.

With its IR shell morphology filled with thermal X-rays, the Radio Arc bubble is therefore a likely superbubble associated to the young and massive Quintuplet cluster.

3. G359.41–0.12 and the Sgr C-chimney

In the Sgr C region, Tsuru et al. (2009) have observed a peculiar pair of soft X-ray plasma emission regions, named G359.41–0.12 and the chimney. The former is an $5' \times 3'$ elliptical region, while the latter is a vertical structure emanating from the edge of G359.41–0.12 and extending more than 0.15° towards the Galactic halo. Both structures have comparable spectral properties, consistent with being located at the GC and being physically connected. Tsuru et al. (2009) have measured thermal energies of 5.9×10^{49} erg and 7.6×10^{49} erg and dynamical timescales of 2.4×10^4 yr and 4×10^4 yr for each structure, respectively. The morphology, energetics and timescales of G359.41–0.12 are suggesting this is a thermal SNR. The origin of the chimney is less obvious. Tsuru et al. (2009) proposed that it is an outflow from the SNR, possibly caused by ambient gas distribution and extending up to 30 pc. Conversely, Ponti et al. (2015b) discuss the morphological similarities of the Sgr C-chimney with the Radio Arc and proposed it is part of the GC lobe detected in radio (Law, 2010, see also § V.B.5).

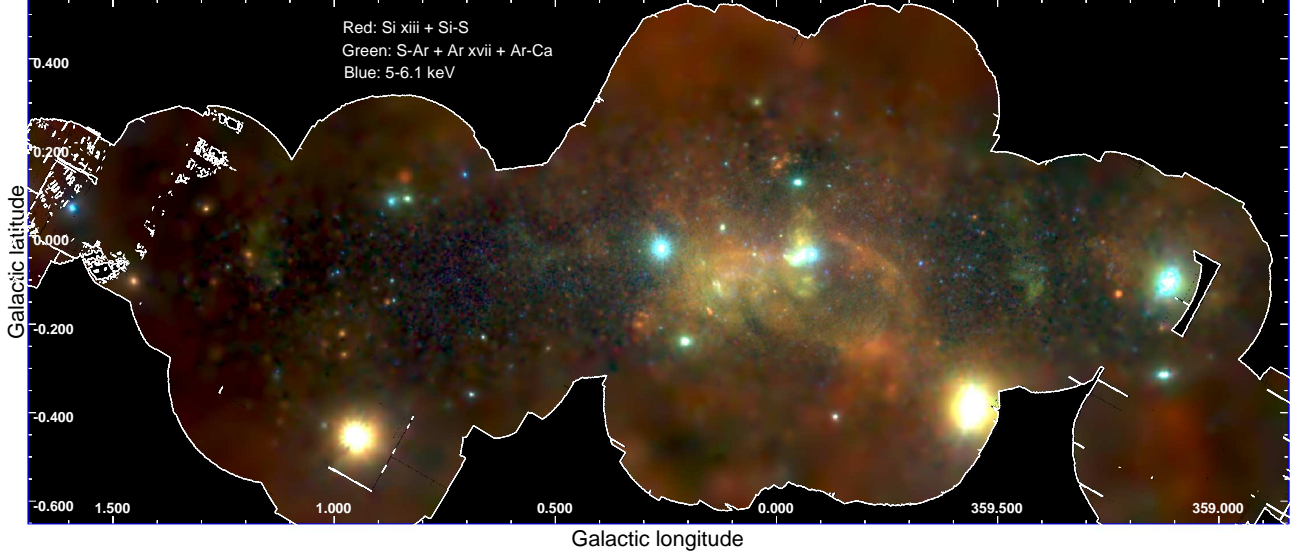


FIG. 16 *XMM-Newton* 3-color image of the soft plasma X-ray emission in the CMZ. Red band is within 1.8–2.3 keV and contains the Si line, green band is within 2.7–3.7 keV and contains the Ar line, blue band is 5–6.1 keV. The large ring like feature west of Sgr A* is clearly visible, as well as the Radio Arc bubble. The bipolar outflows are visible about 0.1° north and south of Sgr A*. Figure extracted from Ponti et al. (2015b).

4. The GC bipolar outflows

The bipolar Sgr A* lobes are symmetric structures extending 15 pc above and below the Galactic plane. They were initially observed in the deep *Chandra* image of the GC (Baganoff et al., 2003; Markoff, 2010; Morris et al., 2003) and were interpreted as a possible outflow from Sgr A*. Further studies with *XMM-Newton* demonstrated the thermal nature of the emission (Heard & Warwick, 2013b). The temperatures range between 0.7 and 1.1 keV, electrons densities between 1–10 cm⁻³, somewhat larger than in the rest of the CMZ. The lobes surface brightness and gas pressure decrease rapidly with increasing latitude indicating outflowing gas (Ponti et al., 2019). Edges are relatively sharp in the X-ray images. Radio observations with the VLA show that the north lobe has a clear radio counterpart characterized by free-free emission. The presence of a radio counterpart to the southern X-ray lobe is less clear (Zhao et al., 2016). The thermal energy in the lobe has been estimated to be a few 10⁵⁰ erg and the sound crossing time of the lobes is a few tens of kyr (Ponti et al., 2019).

Several scenarios have been invoked to explain the lobes (see e.g. Clavel, 2019; Heard & Warwick, 2013b; Markoff, 2010; Morris et al., 2003; Ponti et al., 2019, 2015b). Most of them involve collimation of the plasma injected close to the GC by the CND. They can typically be split in two categories: quasi-stationary outflows of hot plasma, or burst-like injections connected to transient events occurring near the SMBH. Quasi-stationary outflows can be caused by the stellar winds from the mas-

sive stars of the YNC. The latter process is unlikely due to the age difference between the lobe (tens of kyr) and the massive stars, see § I.D.1. The accretion flow onto Sgr A* being radiatively inefficient, it has been proposed that a large fraction of the power and mass accreted at the Bondi radius is dissipated in the form of outflows rather than accreted by the black hole (Wang et al., 2013). The power of these outflows could be sufficient to energize the bipolar lobes. Since the clumpy morphology of the lobes and their sharp edges cannot be easily explained by steady sources, transient or episodic phenomena have been discussed.

The X-ray lobes could have been produced by a supernova occurring in the YNC. With an estimated supernova rate of $0.3\text{--}1.2 \times 10^{-4} \text{ yr}^{-1}$ (Jouvin et al., 2017), it is likely that an explosion has occurred sufficiently recently to have produced the lobes. The energy released should be sufficient to account for the total thermal energy. Ponti et al. (2015b) have proposed that the lobes could be the remnant of the explosion at the origin of the magnetar SGR J1745–290. Hydrodynamical simulations show that a SN can inflate the lobes on a few kyr (see e.g. Yalinewich et al., 2017). Finally, episodic outbursts from the SMBH could be powerful and frequent enough to create the lobes. The energy released by a stellar tidal disruption is sufficient to power the structure and the recurrence rate at the GC is high enough (Alexander, 2005) so that one such event could be at the origin of the lobes. Markoff (2010) have also argued that a collection of prominent outbursts of the SMBH has caused the emission and is responsible for the observed knots.

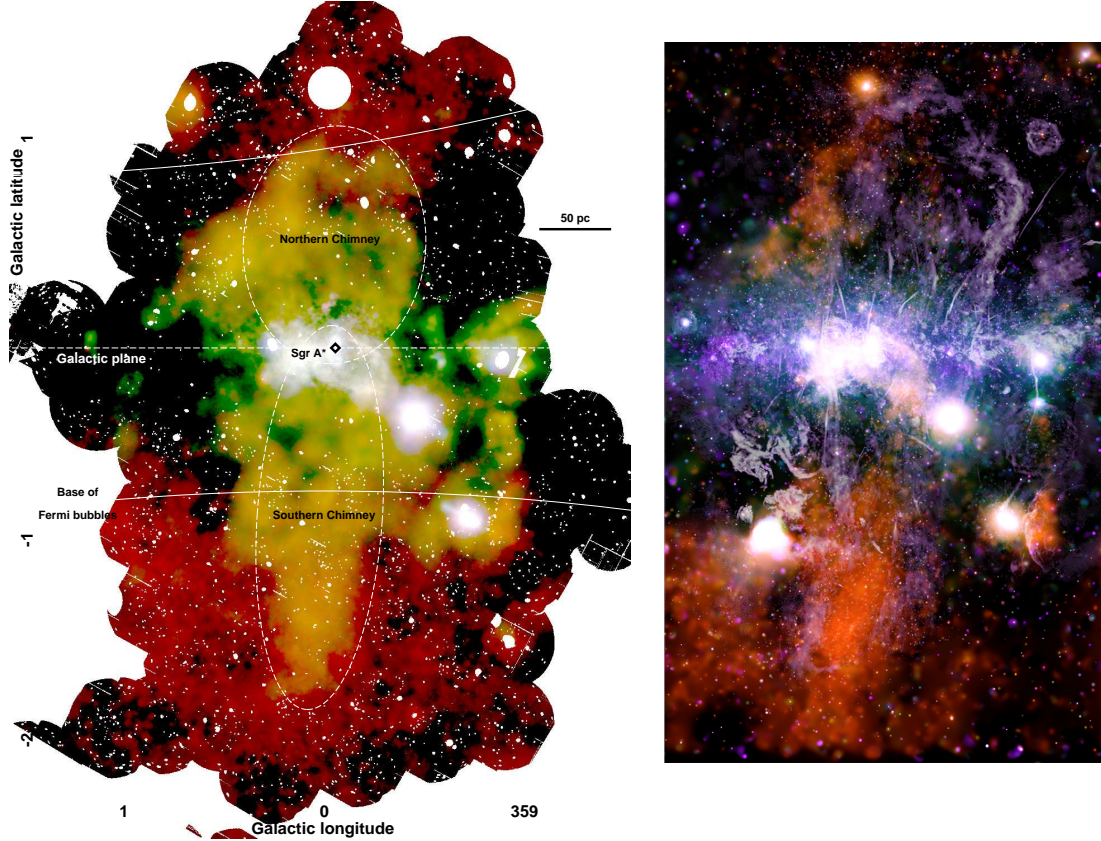


FIG. 17 Left: Three-color image of the X-ray emission from the inner $1^\circ \times 3^\circ$ (red: continuum emission in the 1.5–2.6 keV band, green: 2.35–2.56 keV band (S XV line), blue: continuum emission in the 2.7–2.97 keV band. Two symmetric features are clearly visible extending ~ 150 –200 pc north and south of the GC. These features are reported and called the chimneys by Ponti et al. (2019). The northern part is co-spatial with the GC lobe visible in radio, while the southern lobe has been discovered by Nakashima et al. (2013) and interpreted as 100 kyr old recombining plasma. Figure extracted from Ponti et al. (2019). Right: Composite image of the inner 2.2° by 4.2° , from *Chandra* data (orange, green and purple, Wang, 2021) and from MeerKAT (gray, Heywood et al., 2019). The spatial correlation of the X-ray chimney or plume with the radio bubble, especially in the southern part is clearly visible. Figure extracted from the 2021 *Chandra* photo album (<https://chandra.harvard.edu/photo/2021/gcenter/>), credits X-ray: NASA/CXC/UMass/Q.D. Wang; Radio: NRF/SARAO/MeerKAT.

5. The X-ray chimneys

There are additional evidences of an outflow from the GC on scales of ~ 150 pc. The Galactic Centre lobe is a loop-like structure detected in radio and extending north of the Galactic plane by more than one degree (Sofue & Handa, 1984). A large X-ray thermal emission region has been observed with *Suzaku* one degree south (Nakashima et al., 2013) of the GC. The plasma is optically thin and is over-ionized with a recombining time scale of $\sim 10^5$ yr which had been interpreted as the result of a possible past outflow of the SMBH. A similar degree-scale plume was found in the north of the GC with *Suzaku* supporting such a scenario (Nakashima et al., 2019).

The high-latitude *XMM-Newton* survey of the GC has shown that these plumes are part of a larger structure extending 160 pc to the north and south of the GC, called

the X-ray chimneys (Ponti et al., 2019, see Fig. 17). They are well confined in longitude and present sharp edges. Their base is a relatively large region of 50 pc surrounding Sgr A*. Their thermal energy content is estimated to be $\sim 4 \times 10^{52}$ erg. The chimneys are not symmetric which might be due to ISM asymmetries. Contrary to the bipolar lobes the X-ray surface brightness and plasma electron density are relatively flat over the north and south chimneys. The latter varies from 0.2 to 0.1 cm^{-3} from the base to the top. Based on their different plasma physical characteristics, Ponti et al. (2019) argued that the bipolar lobes and the chimneys are distinct features and that the lobes are embedded in the larger volume of the chimneys.

MeerKAT radio continuum observations have observed a pair of radio bubbles roughly symmetric around the GC with a total span of 140×430 pc (Heywood et al., 2019).

The bubble emission is edge-brightened which suggests it has been caused by a time bounded event, rather than steady state outflows. The cosmic-ray energy in the bubbles is estimated to be 7×10^{51} erg and the total energy content could reach 7×10^{52} erg.

The X-ray and radio structures match well in particular in the southern part where the X-rays are enclosed within the the radio emission (see Heywood et al., 2019; Ponti et al., 2021; Wang, 2021). The association is less clear in the northern part, since the two emissions do not exactly overlap (Wang, 2021). Some authors even propose that part of the northern radio bubble, coincident with the thermal radio emission in the west of the GC lobe, is in fact a foreground H II region (Tsuboi et al., 2020). Yet, Ponti et al. (2021) suggest that the chimneys could be tilted towards us so that the northern structure is in front of the GC. Finally, Ponti et al. (2021) found that the bubble correlate well with spurs of warm dust emission surrounding it (visible in WISE IR images) which they interpret as dense gas heated by the shock traced by the radio emission.

The X-ray chimneys and radio bubbles are interpreted as signatures of an outflow from the GC towards the halo and as such are likely connected to the Galaxy scale *Fermi* and *eROSITA* bubbles (see § VII.C). Several type of processes might have created them: past activity from the SMBH or nuclear star formation processes. Zhang et al. (2021) have performed numerical simulations showing that supernovae occurring in the nuclear stellar disk naturally form a collimated outflow, and by adjusting the SN rate and vertical magnetic field strength they could reproduce the morphology of the X-ray chimneys. Another possible interpretation is that the chimneys act as a channel connecting the intermittent activity of the GC with the larger scale features like the *Fermi* bubbles (Ponti et al., 2019, 2021). This is supported by the observation of linear plasma structures in the southern chimney and interpreted as an ‘exhaust vent’ by Mackey et al. (2024). Measurements of proper motions or Doppler shifts which might be accessible with micro-calorimeters would give credit to this hypothesis.

C. Non-thermal emission by molecular clouds: past activity of Sgr A*

A bright and highly variable non-thermal emission correlated with the molecular clouds has been first detected through the CMZ in the 1990s (see § II.A), traced by both a strong Fe K α fluorescent emission line and a hard X-ray continuum. Its detailed properties (§ V.C.1) are characteristic of an illumination by photons produced by the intense past activity of a hard X-ray source. These photons, most likely originating from Sgr A*, are currently propagating in the inner region of our Galaxy (§ V.C.2). When these light echoes leave the clouds, a fainter level

of non-thermal emission remains, whose origin has also been investigated (§ V.C.3).

1. Properties of the bright non-thermal emission

The morphology of the non-thermal X-ray emission detected at the Galactic center closely follows the distribution of matter in the CMZ, with the brightest regions being Sgr B, Sgr A and Sgr C molecular complexes (see Fig. 18, Koyama 2018; Terrier et al. 2018, and references therein). Within these molecular complexes, the non-thermal emission traced by a prominent 6.4 keV fluorescent line is highly structured, with bright clumps or filaments and more diffuse and extended features matching molecular material also seen in submillimeter line surveys (Alboslani et al., 2025; Brunker et al., 2025; Clavel et al., 2014, 2013; Ponti et al., 2010; Terrier et al., 2018). This correlation indicates that these clouds play a key role in the emission process. It is also important to note that while the bright X-ray non-thermal emission matches with molecular structures, within each molecular complex not all clouds are emitting X-rays and the ones that are emitting are not necessarily the densest ones, indicating that the signal is restricted to a fraction of the CMZ only (e.g. Ponti et al., 2010; Terrier et al., 2018).

Moreover, the non-thermal emission of the CMZ is highly variable both in flux and in morphology. Clear signatures of flux variability have been first reported towards Sgr B (Inui et al., 2009; Terrier et al., 2010) and are now detected across the whole CMZ (Terrier et al., 2018, and references therein). The collection of X-ray bright clouds has also changed over the past decades, indicative of a signal propagation through these regions (e.g. Churazov et al., 2017; Clavel et al., 2013; Terrier et al., 2018). Such propagation has been characterized to be superluminal across the Bridge cloud inside the Sgr A region (Ponti et al., 2010), and such motion can only be reproduced by projection effects of light echoes from a source that is distant from the reflecting clouds. Thereby, these results ruled out previously competing scenarios involving LECR interacting with MC (e.g. Tatischeff et al., 2012).

Dedicated variability studies of the CMZ have shown that, for a given cloud, the amplitude and the time-scale of the variability depend on the size of the region considered. For instance, larger regions tend to have lower amplitude and slower variations, which can be explained by the dilution of the variable signal and/or a sum of sub-structures varying differently (Clavel et al., 2013; Rogers et al., 2022). The variability properties can also change from one cloud to another, which can be explained by either different density distribution of the clouds along the LoS and/or differences in the incident light front itself (Clavel et al., 2013, see also Cramphorn & Sunyaev,

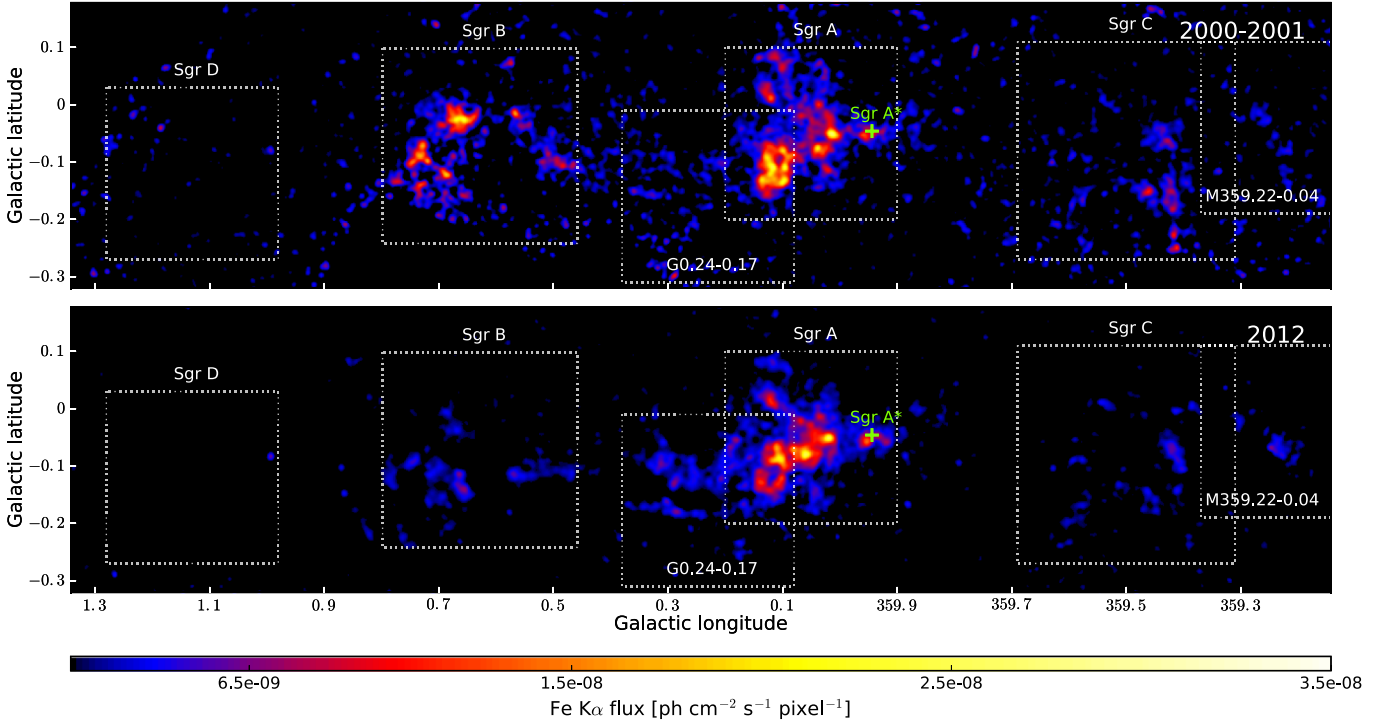


FIG. 18 Morphology and variability of the non-thermal emission at the Galactic center, traced by the Fe K α fluorescent line detected by *XMM-Newton* in 2000-2001 (top) and in 2012 (bottom). Figure from Terrier et al. (2018), reproduced with permission © ESO. The white dotted squares highlight all molecular complexes with 6.4 keV emission detected (see also Fig. 1).

2002; Odaka et al., 2011; Sunyaev & Churazov, 1998, for theoretical estimations of MC emission light curves). In particular, the variability study performed on the smallest possible scale with *Chandra* in the Sgr A region has revealed two different time behaviors: a very short peaked signal that lasts no longer than two years, and slower linear variations, either increasing or decreasing over a decade or so (Fig. 19, Clavel et al., 2013). The variations detected across the CMZ are all compatible with these two time behaviors, and all bright features have been significantly variable over the past decades (Chuard et al., 2018; Terrier et al., 2018). The amplitudes between the lowest and the highest non-thermal fluxes detected for these individual clouds are generally a factor of a few. The strongest variation reported so far is a flux increase of at least a factor of 10 over less than a year of a 1-pc scale filament within the Sgr A molecular complex (Clavel et al., 2013). As of 2025, the latest X-ray observations of the CMZ show a decreasing trend of the once brightest molecular structures, with only a few brightening features. The current brightest region is coincident with the eastern part of the Bridge molecular cloud (Khabibullin et al., 2022; Marin et al., 2023).

X-ray observations with *ASCA*, *Suzaku*, *XMM-Newton* and *Chandra* have shown that the spectrum of the bright non-thermal emission is characterized by a strong emission line created by the fluorescence of neutral iron, Fe K α at 6.4 keV, with an equivalent width $EW \sim 1$ keV,

and the associated Fe K β line at 7.06 keV with an EW which is about seven times lower. These lines are associated with a power-law continuum which is absorbed at low energies, with column densities ranging from few 10^{22} to $\sim 10^{24}$ cm $^{-2}$, in agreement with the N_H integrated along the line of sight in the direction of the CMZ. The current spectral measurements are also compatible with the presence of an absorbing Fe K edge at 7.1 keV (see Inui et al., 2009; Murakami et al., 2001a, 2000; Nobukawa et al., 2011; Ponti et al., 2010; Ryu et al., 2009, 2013, for examples of detailed spectral analyses). Observations at higher energies with *NuSTAR* and *INTEGRAL* have detected this non-thermal component up to 40 keV and even to 100 keV, in the brightest regions, allowing to better constrain the power-law photon index of the signal to $\Gamma \sim 2$ (Krivonos et al., 2017, 2014; Mori et al., 2015; Revnivtsev et al., 2004; Terrier et al., 2010; Zhang et al., 2015). Spectral analyses performed on observations from different years show that the 6.4 keV emission line and the underlying power-law continuum vary synchronously (Clavel et al., 2014; Nobukawa et al., 2011; Terrier et al., 2010) and the typical surface brightness reported for the 6.4 keV line at the peak ranges from few 10^{-5} cm $^{-2}$ s $^{-1}$ arcmin $^{-2}$ for the brightest region in Sgr A down to few 10^{-7} cm $^{-2}$ s $^{-1}$ arcmin $^{-2}$ in Sgr D (Terrier et al., 2018).

Finally, *IXPE* has detected polarization towards the Sgr A molecular complex, with a polarization degree of

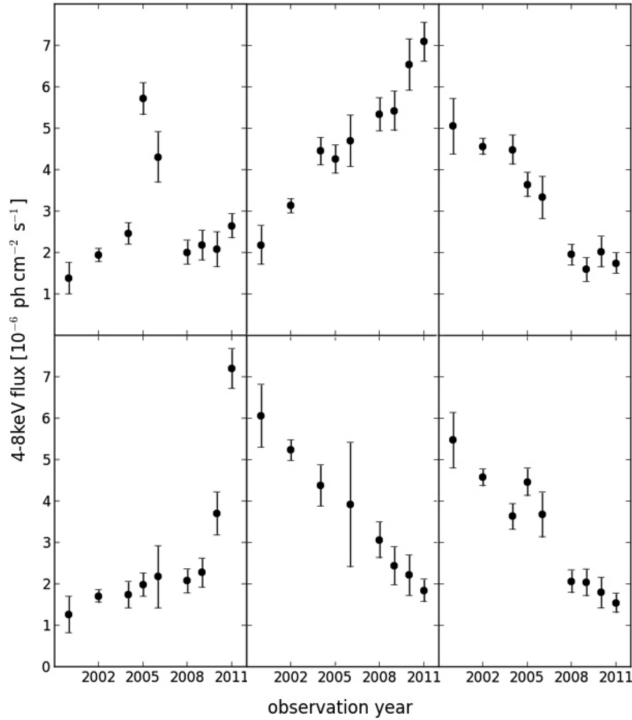


FIG. 19 The two different time behaviors of the non-thermal emission observed within the Sgr A molecular complex. The 4–8 keV light curves are extracted from $15'' \times 15''$ sub-regions of the Bridge cloud (left) and of three other molecular clouds (middle and right). Figure adapted from Clavel et al. (2013), reproduced with permission © ESO.

the non-thermal continuum emission of $(31 \pm 11)\%$ and a polarization angle of $(-48 \pm 11)^\circ$ (Marin et al., 2023). These values further prove the reflection nature of the signal and constrain the scattering geometry. In particular, the direction between the cloud and the illuminating source is likely perpendicular to the direction of the polarization detected¹⁰, making the *IXPE* measurement compatible with a past illumination from Sgr A* (Marin et al., 2023).

2. X-ray echoes and past activity of Sgr A*

The variability, the spectral shape and the polarization of the bright non-thermal emission, along with its correlation with molecular clouds, are all consistent with it being caused by the reflection of X-ray light onto molecular material present in this region (Churazov et al., 2002; Sunyaev & Churazov, 1998). This incident X-ray light is scattered by the cloud, creating the power-law continuum with the same photon index than the incident

spectrum with significant photoelectric absorption within the cloud (and possibly also all along the light path), inducing both a spectral absorption at low energy and fluorescence. Several elements have their K-shell fluorescence lines in the X-ray energy range. The strength of these emission lines depends on both the abundance of the element and the probability of fluorescence after photoelectric absorption by atoms of this element, which explains why the Fe K α line dominates the spectrum of the reflected signal.

The exact shape of the spectrum, including the intensity of the 6.4 keV emission line, depends on the cloud properties (size, density, metallicity), on the incident signal properties (luminosity, spectrum and duration), as well as on the geometry of the reflection (LoS position of the cloud and its distance to the source) and possible absorption along the light path (e.g. Odaka et al., 2011; Sunyaev & Churazov, 1998; Walls et al., 2016). Thus, the 6.4 keV flux of a spherical cloud at a distance D from the observer is a function of the luminosity L_X of the incident event, and can be written as:

$$F_{6.4\text{keV}} \propto f_{Fe} \frac{\Omega}{4\pi D^2} \delta_{Fe} N_H \sigma_K^{Fe} L_X \quad (1)$$

where f_{Fe} is the iron fluorescent yield, δ_{Fe} the iron abundance with respect to hydrogen, σ_K^{Fe} the iron K shell photoabsorption cross section at 7.1 keV, Ω the solid angle of the cloud from Sgr A*, and N_H the illuminated column density within the cloud. Using reasonable values for all these parameters, the observed Fe K α flux can therefore be used to estimate the luminosity of the incident event (Sunyaev & Churazov, 1998). If we assume the source responsible for the X-ray echoes is at the Galactic center, the corresponding events need to have an X-ray luminosity in the 2–10 keV range of at least a few 10^{39} erg s $^{-1}$ for several years to explain the brightest molecular clouds (e.g. Koyama et al., 1996; Murakami et al., 2001b; Ponti et al., 2010). The actual value of Sgr A*'s past luminosity depends on the line-of-sight position of the cloud as well as the duration of the illuminating event. Clouds that are further away from Sgr A* than their projected distance will intercept a smaller fraction of the incident signal, while shorter events will illuminate only a fraction of the clouds at a given time, resulting in a possibly large underestimation of the past luminosity of Sgr A* (Churazov et al., 2017).

The energetic involved and the spectral constraints are such that among the variety of X-ray transients in the inner region of our Galaxy, only the supermassive black hole Sgr A* can be responsible for the X-ray echoes detected across the CMZ (Clavel et al., 2013). The time delay t between the direct detection of an event from Sgr A* and of its reflection onto a given molecular cloud, depends on the projected distance x and the line-of-sight distance z between the cloud and the black hole. Thereby, at a given time, all clouds illuminated by the same event are

¹⁰ This statement assumes that the incident light is not polarized (see Khabibullin et al., 2020, for more details).

distributed along the paraboloid defined by

$$z(t) = \frac{1}{2} \left(ct - \frac{x^2}{ct} \right), \quad (2)$$

where c is the speed of light (Fig. 20; Sunyaev & Churazov, 1998). Therefore, the extension of the CMZ along z and x allows, in principle, to probe Sgr A*’s past activity from the past 1000 years or so.

However, reconstructing the past lightcurve of Sgr A* from the X-ray echoes is not trivial, since the line-of-sight position of the clouds are poorly known (see § I.C.1 and Fig. 2). Therefore, different techniques have been developed through the years to constrain the past activity of Sgr A* from the properties of these bright X-ray echoes, using their variability pattern, their spectral shape and, more recently, also their polarization properties.

The light curves of the clouds are the result of a convolution between the past light curve of Sgr A* and the density profile of the clouds. Therefore, studying the variability of the 6.4 keV emission on the smallest possible scale, to avoid averaging substructures that vary differently, can provide strong upper limits on the duration of the illumination. Such studies have shown that for all bright clouds the illumination cannot be longer than about a decade (Terrier et al., 2018), and even shorter than a few years for several clouds in Sgr A (Churazov et al., 2017; Clavel et al., 2013). Furthermore, under the assumption that clouds that are experiencing the same time behavior are illuminated by the same past event from Sgr A*, it is possible to constrain their relative position following equation (2). However, the age of the event t remains unknown, unless there are constraints about the line-of-sight position of the reflecting clouds. Methods have been developed to infer it from the spatial and temporal variation themselves (Churazov et al., 2017), or from the 6.4 keV flux and the relative density of the clouds obtained from molecular tracers (Clavel et al., 2013; Ponti et al., 2010). However, the results obtained strongly depend on the number of illuminating events assumed by the authors.

A precise modeling of the X-ray emission detected towards the clouds can provide independent information on their line-of-sight position. The cloud will absorb a higher fraction of the X-ray emission from the ambient plasma if located closer to the front edge of the CMZ, providing information on its position within the CMZ (Ryu et al., 2009, 2013). The spectrum of the echo itself also depends on the line-of-sight position of the cloud: the properties of the continuum emission change with respect to the scattering angle, while the characteristics of the fluorescent lines are isotropic. Hence, the equivalent width of the emission lines depend on the scattering angle (Capelli et al., 2012), and dedicated spectral models accounting for the geometry of the reflection process have been developed to retrieve the line-of-sight position of the reflecting clouds (e.g. Chuard et al., 2018; Walls

et al., 2016, see also Fig. 20). Given the possible degeneracies between the spectrum of the X-ray echo, the astrophysical background emissions and the foreground absorption, absolute positions obtained from these techniques can suffer from poorly controlled uncertainties.

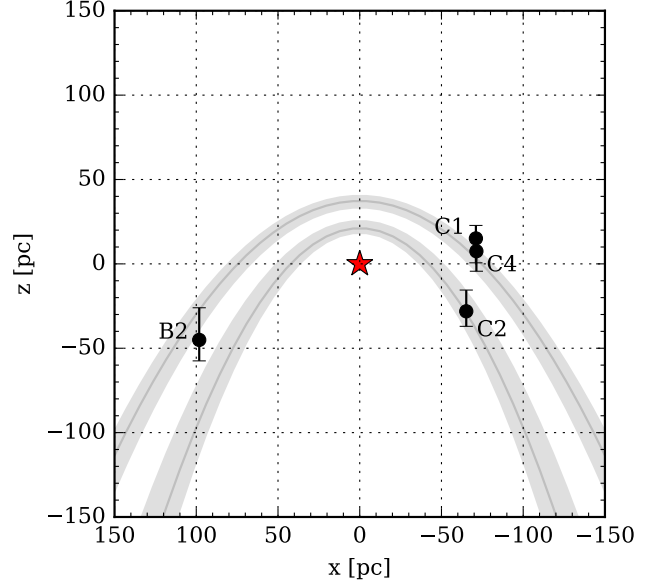


FIG. 20 Echoes in the Galactic center viewed from the Galactic north pole. The line-of-sight distance (z) of clumps within Sgr B (B2) and Sgr C (C1, C2 and C4) derived from their spectral shape are shown in black. The red star marks the position of Sgr A*. The grey parabolas correspond to the two past events illuminating the CMZ derived by Chuard et al. (2018), together with their age uncertainty (parabola widths). They corresponds to a relatively short event occurring ~ 140 years ago and a longer one occurring ~ 240 years ago. Figure from Chuard et al. (2018), reproduced with permission © ESO.

Lastly, the polarization degree of the X-ray echo also depends on the scattering angle, with decreasing values for increasing absolute values of the line-of-sight position, $|z|$ (Churazov et al., 2002). The current brightness of the reflection signal across the CMZ, restrict polarization measurement with *IXPE* to a single subregion within the Sgr A molecular complex (see § V.C.1). The polarization degree reported is compatible with a two-century old event from Sgr A* (Marin et al., 2023). However, any unpolarized signal contributing to the non-thermal emission or the possible contribution from different clouds having different polarization properties would lower this value.

Based on the variability, spectral and polarization constraints obtained, there is a consensus on the fact that Sgr A* was at least a million times brighter than today for at least a short period of time within the past three centuries or so. The number of past outbursts currently propagating in the CMZ, their exact age, duration and

luminosity, are however still debated (see e.g. Chuard et al., 2018; Churazov et al., 2017; Clavel et al., 2013; Stel et al., 2025, and Fig. 20). The nature of the accretion events that likely caused these past outbursts is also unknown, and several scenarios have been proposed, including the tidal disruptions of low-mass objects (cold clumps from stellar winds, gas clouds, planets), the partial capture of a star or a ‘failed’ TDE (see e.g. Cuadra et al., 2008; Czerny et al., 2013; Sacchi & Lodato, 2019; Yu et al., 2011; Zubovas et al., 2012).

3. Fading signals and constraints on what remains

The light front created by Sgr A*’s past outbursts are currently propagating within the CMZ, creating the bright X-ray echoes described in § V.C.1. These light fronts are expected to progressively leave the clouds that have been illuminated in the past decades, possibly reaching other features along the line of sight, and will eventually leave the CMZ. The monitoring of the variations over the last decades has shown a global decrease of the emission in most regions (Khabibullin et al., 2022; Terrier et al., 2018). The once brighter molecular cloud Sgr B2 follows this trend, while on small scales *XMM-Newton* still detects limited variability surrounding the densest core, Sgr B2 itself is at its record low in terms of 6.4 keV flux (Rogers et al., 2022). Starting from 2011, on larger scales, the *INTEGRAL* light curve of Sgr B2 has entered a regime consistent with a constant flux in the hard X-rays (30–80 keV, Kuznetsova et al., 2022), questioning the nature of the remaining stationary signal detected from this molecular cloud and from others (see e.g. Kuznetsova et al., 2019).

A stationary and fainter non-thermal emission could be created by the same process as the bright X-ray echoes, for instance by the reflection of a lower-luminosity plateau in the light curve of Sgr A*, or by sparser material with a larger extension along the line of sight. However, following the passage of the light front across the densest molecular clouds of the CMZ, an emission due to multiple scattering could persist over several years, creating a stable non-thermal signal with a harder spectrum and a 6.4 keV emission line including a large Compton shoulder (Odaka et al., 2011). A possible alternative to a reflection-related origin of this stationary emission is the interactions between LECR and the molecular clouds (see § V.D). The spectral constraints currently available do not allow to conclude on the respective contribution of these different processes to the faint level of stationary non-thermal emission (Chernyshov et al., 2018; Kuznetsova et al., 2022; Rogers et al., 2022; Zhang et al., 2015). However, LECR are likely not responsible for the major part of Sgr B2’s current level of non-thermal emission, either due to unphysical spectral parameters (for electrons, Rogers et al., 2022; Zhang et al., 2015) or to

incompatibilities with constraints based on other tracers (for protons, Kuznetsova et al., 2022, see also § V.D.3).

D. Ionization and non-thermal emission from cosmic rays

As we will see in § VI, gamma-ray observations of the GC region reveal the presence of ongoing particle acceleration there, not associated to the ubiquitous background of cosmic rays that pervades the entire Galactic disk (for a general overview on Galactic cosmic rays see Gabici 2022). It is therefore natural to explore whether such additional component in the CR intensity plays a role in the generation of the non-thermal X-ray emission in the CMZ discussed above. In particular, the interactions of LECRs (sub-GeV) with the gas in the CMZ might result in a stationary X-ray emission.

A way to constrain/predict the contribution from LECRs to the stationary hard X-ray emission from the CMZ is to search for other manifestations of the presence of such particles in the region. With this respect, one possibility is to search for absorption or emission lines associated to molecular species which are produced in clouds as a result of the cosmic-ray ionisation of interstellar matter (e.g. Dalgarno, 2006; Tielens, 2013). Particles in the sub-GeV domain are most effective in ionising interstellar matter. The amount of LECRs present in the region can be then derived from the intensity of these lines, provided that the chemistry operating in the cloud is well known.

1. A very large cosmic ray ionisation rate in the CMZ revealed by molecular lines

LECRs play a crucial role in molecular clouds, as they are the only ionising agents able to penetrate large column densities of gas (see Gabici, 2022; Padovani et al., 2020, for reviews). This is because the ionising UV radiation is absorbed in the external layers of the cloud. The classification of molecular clouds is a complex matter (see e.g. Snow & McCall, 2006), but for simplicity here we name them *diffuse* or *dense*, depending on whether photons or cosmic rays dominate the ionisation of the gas in the cloud, respectively. With this definition, the transition from photoionisation to cosmic-ray ionisation takes place at a hydrogen column density of $N_H \approx 8 \times 10^{21} \text{ cm}^{-2}$ (McKee, 1989).

A quantity which is generally adopted to quantify the ionisation of interstellar matter due to LECRs is the CR ionisation rate of molecular hydrogen, ζ_{CR} , which has units of s^{-1} and represents the number of CR-induced ionisations per second and per hydrogen molecule. For reference, the value of this quantity in the local interstellar medium could be measured with unprecedented accuracy after the Voyager probes crossed the heliopause

and entered interstellar space (see Cummings et al., 2016, and references therein). For CR nuclei, the local ionisation rate slightly exceeds $\zeta_{CR}^N \sim 3 \times 10^{-17} \text{ s}^{-1}$, while for CR electrons, due to the steepness of their energy spectrum, this quantity cannot be constrained but certainly exceeds $\zeta_{CR}^e \sim 0.5 \times 10^{-17} \text{ s}^{-1}$ (e.g. Cummings et al., 2016; Gabici, 2022).

In diffuse molecular clouds, UV radiation mainly ionises carbon and is rapidly attenuated. On the other hand molecular hydrogen, due to its larger ionisation potential, is mostly ionised by cosmic rays. Once produced, H_2^+ interacts very rapidly with H_2 to produce protonated molecular hydrogen, H_3^+ . This molecule plays a pivotal role in molecular clouds, as it triggers most interstellar chemistry (e.g. Dalgarno, 2006). Rovibrational transitions of H_3^+ can be observed in the infrared absorption spectra of stars embedded in (or located behind) a molecular cloud (Lindsay & McCall, 2001; Miller et al., 2020; Oka, 2006).

The typical ionisation fraction in diffuse molecular clouds is $\approx 10^{-4}$, mostly determined by photoionisation of carbon. The abundance of free electrons is quite small, but still suffices to determine the rate at which H_3^+ is destroyed (through dissociative recombination). The rate of production of H_3^+ per unit volume is then proportional to the CR ionisation rate, ζ_{CR} , while its destruction rate is proportional to the dissociative recombination Langevin rate constant, which has been measured in laboratory experiments (McCall et al., 2003). This explains why the CR ionisation rate can be estimated from the measured intensity of H_3^+ lines. In fact, as astronomical observations provide the column density of H_3^+ , rather than its volumetric one, the actual quantity that can be constrained from observations is the product $\zeta_{CR} \times L$, where L is the LoS path length inside the cloud. This introduces an important uncertainty on the estimate of the CR ionisation rate, as it is not trivial to measure L .

Oka et al. (2005) reported on the detection of H_3^+ absorption lines in stellar spectra along lines-of-sight crossing the CMZ. From the measured column densities of H_3^+ , they obtained values of the product $\zeta_{CR} \times L$ exceeding $\mathcal{O}(10^4) \text{ cm s}^{-1}$. This implies that values of the CR ionisation rate similar to those measured in the local ISM would require unreasonably large values of the path length, namely, L exceeding a kiloparsec, which is larger than the size of the CMZ! They were forced to conclude, then, that the ionisation rate close to the GC has to be much larger than the local one.

New infrared observations were performed by the same team in order to increase the number of sightlines explored (e.g. Goto et al., 2014) and Oka et al. (2019), based on spectral observations of about 30 stars located through the entire CMZ (from 140 pc west to 120 pc east of Sgr A*), estimated an astonishingly large CR ionisation rate of $\zeta_{CR} \sim 2 \times 10^{-14} \text{ s}^{-1}$. An independent study based on a similar set of H_3^+ data and on a more detailed

chemical modelling also obtained extremely large values of the ionisation rate in the range $\zeta_{CR} \sim 1-11 \times 10^{-14} \text{ s}^{-1}$ (Le Petit et al., 2016). No significant spatial variations of the ionisation rate were observed across the CMZ. These measurements probe the warm ($\sim 200 \text{ K}$) and diffuse ($< 100 \text{ cm}^{-3}$) gas phase, which dominates the volume of the CMZ (Oka et al., 2019).

The detection, in stellar spectra, of absorption lines from the oxygen-bearing ions OH^+ , H_2O^+ , and H_3O^+ can also be used to constrain ζ_{CR} in diffuse atomic clouds. This is because the chain of reactions leading to the formation of such ions is initiated by the CR ionisation of atomic hydrogen, followed by charge exchange with oxygen, and then by a chain of reactions with H_2 to produce the sequence of hydrides $\text{O}^+ \rightarrow \text{OH}^+ \rightarrow \text{H}_2\text{O}^+ \rightarrow \text{H}_3\text{O}^+$. The analysis of *Herschel* spectral data performed by Indriolo et al. (2015) showed that, for lines-of-sight crossing the CMZ, the abundance of such molecules implies very large ionisation rates in the range $2 \times 10^{-15} \text{ s}^{-1} \lesssim \zeta_{CR} \lesssim 2 \times 10^{-14} \text{ s}^{-1}$.

Finally, the high gas temperatures (from $\sim 60 \text{ K}$ to 100 K and beyond) measured in the dense clouds within the CMZ are most likely due to turbulent heating, and this allows to infer an upper limit on CR heating which would correspond to a quite large upper limit on the CR ionisation rate, $< 10^{-14} \text{ s}^{-1}$. However, this applies to the dense gas, and CRs may play a more prominent role in the diffuse phase (where H_3^+ measurements are relevant) (Ginsburg et al., 2016).

The results summarised above show that very large values of the CR ionisation rate are consistently found in the diffuse gas phase of the CMZ, based on observations of several chemical tracers, and this suggests that the intensity of low-energy (sub-GeV) CRs has to be much larger (by several orders of magnitude!) there than in the local ISM. This is indeed very puzzling because, as discussed in § VI.C, the interpretation of gamma-ray observations of the CMZ do not require any large excess in the intensity of CRs in the $\approx \text{GeV}$ energy domain. A simultaneous explanation of gamma-ray and astrochemical data would then require a very fine-tuned shape of the spectrum of CRs, exhibiting an extremely large enhancement in the sub-GeV energy domain (Ravikularaman et al., 2025).

Sightlines crossing the CMZ and characterised by large gas column densities (dense clouds) can also be probed, even though the large gas column densities might prevent the observation of background/embedded stars and therefore the search for absorption lines. As an alternative, one can search for molecular emission lines at submillimeter/millimeter wavelengths, and also in this case enhanced values of the ionisation rate have been reported. van der Tak et al. (2006) combined APEX and IRAM 30-m telescope data to map the distribution of H_3O^+ and H_2O in the Sgr B2 region. Based on astrochemical modeling, they found that the observed $\text{H}_3\text{O}^+/\text{H}_2\text{O}$ line intensity ratio requires a CR ionisation

rate of the order of $\zeta_{CR} \sim 4 \times 10^{-16} \text{ s}^{-1}$. This value is about one order of magnitude larger than the ionisation rate in the local ISM, as estimated based on data from the Voyager probes, but much smaller than that estimated in the diffuse molecular and atomic gas phases within the CMZ (absorption lines of H_3^+ and hydrides in stellar spectra, see above). These differences might reflect the fact that the penetration of LECRs into dense clouds is hindered by the severe ionisation energy losses suffered by energetic particles when the gas density is large. This would naturally reproduce a gradient in the CR intensity, which would be suppressed inside dense clouds such as Sgr B2 (Dogiel et al., 2015).

An accurate interpretation of these spatial variations of the CR ionisation rate would require a modeling of the penetration of LECRs into dense clouds. Unfortunately, this is a very complex problem, due to the intrinsic non-linearity of CR transport: CRs themselves excite the magnetic turbulence that regulates their penetration into the cloud. An extensive literature exists on the subject, from the pioneer studies by Skilling & Strong (1976) and Cesarsky & Volk (1978), to recent ones (e.g. Morlino & Gabici 2015, Phan et al. 2018, Ivlev et al. 2018, or Dogiel et al. 2018 for an application to the CMZ).

2. Problems with the interpretation of the ionisation rate measurements

Even though modeling the transport of LECRs in the CMZ is a challenging task, some conclusions which are almost model-independent can be drawn from the data. In this respect, a solid argument can be put forward to illustrate the main difficulty encountered in explaining the large values of the ionisation rates. Particles of energy below the GeV domain are those which contribute most to ionisation, and as a consequence they suffer severe energy losses. The ionisation energy-loss time decreases for lower particle energies, and is inversely proportional to the ambient gas density. In dense environments such as the CMZ, the rate at which freshly accelerated particles have to be injected to compensate for those lost due to ionisation has to be extremely fast, requiring an exceedingly large amount of energy (Recchia et al., 2019).

This issue has been investigated in detail by Ravikularaman et al. (2025), who modeled the injection and transport of CR from very low to very high energy in the CMZ. They found that the power needed to maintain a population of sub-GeV particles at the level needed to explain ionisation rates at a level $\zeta_{CR} \sim 2 \times 10^{-14} \text{ s}^{-1}$ is exceedingly large. For CR nuclei, the injection power has to be $\lesssim 10^{41} \text{ erg s}^{-1}$, which is comparable to the estimated power in CR nuclei of the entire Galaxy (Strong et al., 2010). The situation is even worse for CR electrons, that would require an injection power $\gtrsim 10^{40} \text{ erg s}^{-1}$, which is about an order of magnitude larger than the entire CR

electron power of the Milky Way (Strong et al., 2010). To further stress the enormity of the required CR powers, one can notice that they are comparable to the average power needed to inflate the huge *eROSITA* bubbles over the past tens of millions of years (Predehl et al., 2020). Similarly large CR power requirements were also found by Liu & Yang (2024).

Besides the prohibitive values of the CR powers, other observations are difficult to reconcile with the large values of the ionisation rates. As we will see below (see § VI.C), gamma-ray observations of the CMZ suggest the existence of a source of CRs of high energy (GeV and TeV domain) located very close to the GC. If such source is also assumed to produce the sub-GeV ionising particles in a continuous way (to compensate for those lost due to energy losses), one would expect the intensity of CRs to decline away from the GC, at odds with observations. To fix this problem, one might consider a scenario where LECRs are injected everywhere within the CMZ by a population of (unspecified) sources. In this case, the flat spatial profile of ionisation rates could be reproduced, but the energy reservoir problem would be even more severe, as the source of the power would not be connected with the SMBH located at the GC, which is the most powerful source in the region. Finally, if LECR electrons are invoked to explain the ionisation rates, the associated non-thermal Bremsstrahlung emission from these particles would have been detected in the sub-MeV domain by the SPI instrument on *INTEGRAL* as a steady source coincident with the CMZ, in disagreement with what has been reported by Bouchet et al. (2008).

All these issues show that it is extremely difficult to build a self-consistent scenario where LECRs are responsible for large ionisation rates observed within the CMZ (Ravikularaman et al., 2025). The only other plausible ionising agent is UV/X-ray radiation, but also this scenario does not seem to be very promising. UV photons are absorbed very quickly after crossing moderate column densities of gas (McKee, 1989), and even X-rays coming from past flares of Sgr A* would not suffice (Dogiel et al., 2013). The origin of the large ionisation rates remains a true puzzle.

3. Implications for high-energy observations: nuclear gamma-ray lines and 6.4 keV Fe K α line

An enhancement in the LECR intensity in the CMZ has at least two significant implications for high-energy observations. First, excitation of nuclear levels follows from the interactions of LECR nuclei with ambient matter, and the resulting de-excitation lines may be observed in the MeV domain (Ramaty et al., 1979). Second, the CR ionisation of iron atoms in a cold gas is accompanied by emission at 6.4 keV (e.g. Tatischeff et al., 2012, and references therein). The 6.4 keV line emission from

LECRs would be stationary, and therefore distinguishable from the X-ray reflection component discussed in § V.C.1.

Liu & Yang (2024) computed the expected intensity of nuclear line emission under the assumption that an ionisation rate of $2 \times 10^{-14} \text{ s}^{-1}$ (the largest reported value, Oka et al. 2019) is produced by LECR nuclei in the CMZ. They found that the line intensities are within the capabilities of future proposed MeV missions (see § II.D). However, these estimates are based on the most optimistic value for the ionisation rate in the region. A more conservative choice of this parameter (but still consistent with other values reported in the literature, for example those based on *Herschel* data which give $2 \times 10^{-15} \text{ s}^{-1} \lesssim \zeta_{CR} \lesssim 2 \times 10^{-14} \text{ s}^{-1}$) would make the perspective of a detection of nuclear lines much less appealing.

Similar conclusions can be drawn for the intensity of the 6.4 keV Fe K α line resulting from LECRs in the region. Several estimates from the line intensity can be found in the literature, for both LECR electrons and nuclei (Dogiel et al., 2009, 2015; Ravikularaman et al., 2025; Yusef-Zadeh et al., 2013, 2007). The most recent estimates by Ravikularaman et al. (2025) indicate that the LECR-related line intensity is much smaller (few orders of magnitude) than the currently observed one, which is due to X-ray reflection (Terrier et al., 2018). The value reported by Ravikularaman et al. (2025) is a spatially averaged one over the entire CMZ, and therefore more optimistic conclusions can be certainly drawn for dense concentrations of mass such as the Sgr B2 cloud (e.g. Dogiel et al., 2015). Thus, while the detection in the near future of the stationary signal of the Fe K α line associated with LECRs seem to be unlikely for the entire CMZ, pointed observations of most massive clouds might provide interesting constraints.

VI. GAMMA-RAY EMISSION AND COSMIC RAYS IN CMZ AND BEYOND

Gamma-ray observations from the HE to VHE domains reveal a bright source positionally coincident with Sgr A*. We review its measured characteristics and discuss some of the interpretations that have been proposed in § VI.A. In addition to the GC source, several gamma-ray sources are detected in the CMZ, in particular PWNe, which we discuss in § VI.B. Diffuse emission coincident with massive clouds in the inner 200 pc has also been detected. It reveals an excess of CRs at the GC, likely injected by an accelerator located in the inner few pc (see VI.C). On larger sizes, excess gamma-ray emission from the Galactic bulge is visible at the GeV and in soft gamma-rays at 511 keV. We briefly review these emissions and discuss their possible interpretations in § VI.D.

A. The central gamma-ray source

1. Observational results

The GC is known to harbor a gamma-ray source since EGRET detected a bright emission at a position compatible with that of Sgr A* (Mayer-Hasselwander et al., 1998). The source, named 3EG J1746–2851 (Hartman et al., 1999), was found to be located within 0.2° of the GC. Because of the poor angular resolution of EGRET and the large confusion in the region, the exact localization and possible confusion has lead to questioning its association with the GC (Pohl, 2005).

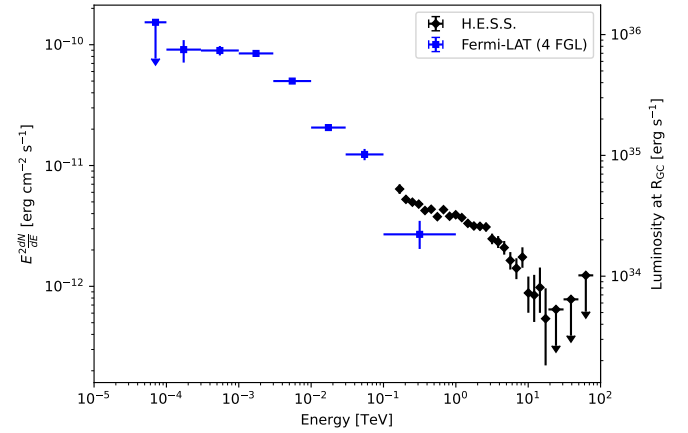


FIG. 21 Broadband SED of the gamma-ray source at the GC as reported by the 4th *Fermi* catalog 4FGL J1745.6–2859 (Abdollahi et al., 2020), and by H.E.S.S. Collaboration et al. (2016) for HESS J1745–290. The equivalent luminosity at the distance of 8.3 kpc is indicated on the right side axis.

The Galactic center has been a major target of interest for gamma-ray instruments in the Very High Energy domain for years before it was finally detected in 2004 by several instruments, namely Whipple (Kosack et al., 2004), Cangaroo-II (Tsuchiya et al., 2004) and H.E.S.S. (Aharonian et al., 2004). All reported the observations of a relatively bright and steady point-like source coincident with the SMBH position, which we name HESS J1745–290 in the following. Its luminosity, assuming it is located at the GC, is found to be of the order of $5 \times 10^{34} \text{ erg s}^{-1}$ (Aharonian et al., 2004; Albert et al., 2006; Archer et al., 2016). First results showed a rather hard power-law spectrum of index 2.2–2.3 without any significant curvature (Aharonian et al., 2004; Albert et al., 2006). With deeper observing time, a curvature clearly appeared in the measured spectrum of HESS J1745–290. Aharonian et al. (2009) found it to be well reproduced by an exponential cutoff power-law spectrum and report an index of ~ 2.10 and a cutoff energy of $\sim 15 \text{ TeV}$ (see Fig. 21). Later measurements confirmed this result and found indices ~ 2.1 and energy cutoff val-

ues ~ 10 TeV (Adams et al., 2021; Ahnen et al., 2017; H.E.S.S. Collaboration et al., 2016). It should be noted that the previous measurements do not fully correct for the contamination of the GC diffuse gamma-ray emission and of the Galactic foreground emission (see e.g. H.E.S.S. Collaboration et al., 2018a; Viana & Moulin, 2013).

The origin of the cutoff is an important element to understand the nature of HESS J1745–290. It can be the result of the maximum acceleration energy of the particles producing the gamma-ray emission or, equivalently, result from a change in the particle transport properties or even from pair creation photo-absorption in the strong ambient photon field. Yet, we note that the absorption by the ambient Galactic radiation field on the line of sight does not predict a pronounced suppression of the gamma-ray source flux in this energy range (Celli et al., 2017; Moskalenko et al., 2006). If the cutoff is caused by absorption, it must take place in the immediate surrounding of the acceleration and gamma-ray production site.

Early detections had a position uncertainty of the order of $1'$. After several years of observations and thanks to a very detailed work on the instrument pointing and the associated systematic errors, the H.E.S.S. collaboration was able to reduce the position uncertainty down to $20''$ ($6''$ of statistical uncertainty and $13''$ of systematic uncertainty, Acero et al., 2010). The angular separation between HESS J1745–290 and Sgr A* is found to be of only $8''$ which is consistent with the SMBH position but also with the PWN G359.95–0.04 (see upper panel of Fig. 22).

Acero et al. (2010) found the HESS J1745–290 source to be point-like, with an upper limit on its radius of $1.3'$ (95% C.L.) assuming a gaussian morphology. This size limit is significantly smaller than that of the radio shell of the SNR Sgr A East which shows that the latter can be excluded as the main source of VHE photons (see lower panel of Fig. 22).

To this day, these are the most precise constraint on the position and morphology of the GC gamma-ray source. Improving on this result will require increased statistics as well as a much better constrained pointing and PSF systematic uncertainties. This should be possible with CTAO which should be able to resolve the ambiguity between the SMBH and PWN positions (CTA Consortium et al., 2019). An intrinsic difficulty of such a measurement also lies in the underlying diffuse emission which is expected to be structured on small scales in this region due to the distribution of interstellar medium towards Sgr A* (see next sections).

If HESS J1745–290 is connected to the SMBH, its flux might display time variations on various timescales, from the frequent hour-long flares that Sgr A* experiences to longer timescales accretion rate variations. Variability of the GC gamma-ray source is therefore a crucial observable to interpret its nature. So far, observations of

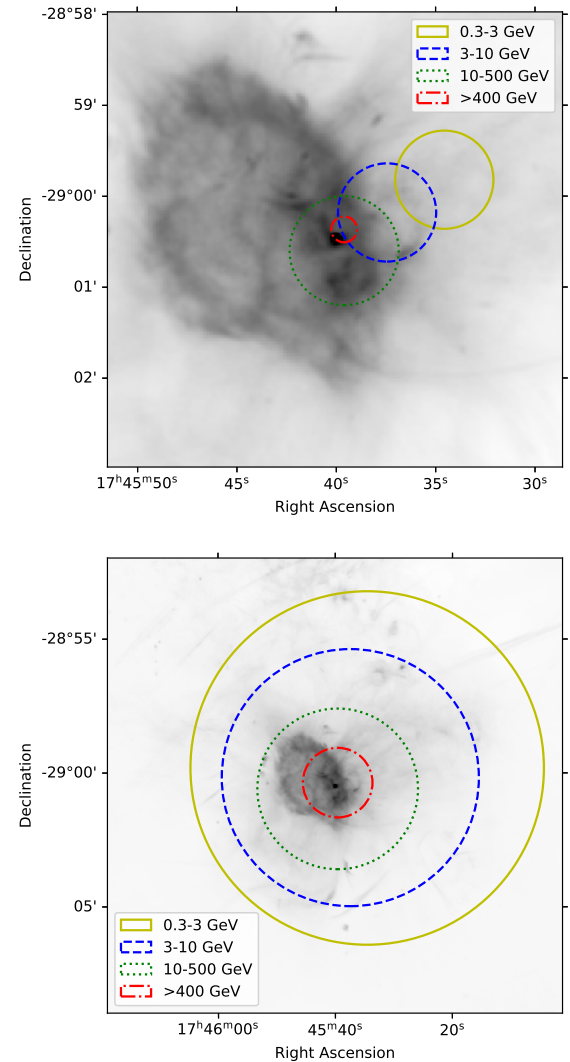


FIG. 22 GC gamma-ray source position errors (upper) and extension upper limits (lower panel) at various energies overlaid on the 1.28 GHz brightness of Sgr A East seen with MeerKAT. Measurements in the 0.3–3, 3–10 and 10–500 GeV were obtained with the *Fermi*/LAT (Cafardo et al., 2021), while the measurement > 400 GeV is obtained with H.E.S.S. (Acero et al., 2010).

HESS J1745–290 have not shown any evidence of variability. Based on observations spanning over three years, light curves obtained by Aharonian et al. (2009) did not reveal any variability on timescales longer than 28 minutes (the duration of an observing run). A factor of two increase compared to the steady flux would be required to detect a flare with timescales of an hour. Similarly, Ahnen et al. (2017) found no significant variation with MAGIC observations taken from 2013 and 2015 (in particular during the G2 periastron passage). Finally,

Adams et al. (2021) did not find any variability on day or months timescales in the VERITAS data set extending from 2009 to 2017.

To search for a possible flux variation in coincidence with an IR or X-ray flare, VHE observations have been conducted in the context of multi-wavelength campaigns aiming at Sgr A*. Such campaigns are crucial to test the existence of a signal in VHE gamma-rays associated with the regular flares observed in NIR and X-rays (see Sect. I.E.2 and III.B). During one such campaign, *Chandra* detected a bright flare during a H.E.S.S. observation. The latter did not reveal any variation of the gamma-ray signal; a factor of 2 variation of the flux could be excluded at 99% confidence level (Aharonian et al., 2008a). CTAO will be sensitive to 20% flux variations of the GC source over 30 minutes (Viana et al., 2019). Current models of Sgr A* flares predict that some of the brightest flares might have IC emission levels close to the CTAO sensitivity at low energy (see e.g. Petropoulou et al., 2024).

In the energy range from 100 MeV to tens of GeV, the excellent performances of *Fermi*/LAT revealed a point source coinciding with the position of Sgr A*. This source was analyzed by Chernyakova et al. (2011) and Malyshev et al. (2015) who found it to be brighter than HESS J1745–290 with a luminosity reaching $\sim 8 \times 10^{35}$ erg s $^{-1}$. Its spectrum was found to be flat in the range of few hundred MeV to few GeV and steeper in the energy range above a few GeV. Yet, the region is complex and subsequent *Fermi* catalogs have described the GC GeV emission with several sources. Abdollahi et al. (2020) finds the source 4FGL J1745.6–2859 within 0.01° of the GC. Cafardo et al. (2021) have reanalyzed more than 10 years of *Fermi* data to precisely characterize the source morphology in several energy bands (the constraints they obtain on the source position and size are shown in Fig. 22).

It is unclear whether the GeV and TeV sources are caused by the same phenomenon. The measured position of 4FGL J1745.6–2859 is only marginally consistent with that of HESS J1745–290 below 3 GeV and is in good agreement above it (Cafardo et al., 2021). The spectrum of 4FGL J1745.6–2859 is also steep in the range of 5 GeV to 300 GeV while the VHE spectrum is flat, suggesting that another component is appearing in this energy range.

So far, no counterpart to the GC gamma-ray source has been detected by neutrino telescopes. Upper limits on the neutrino flux obtained by IceCube (Abbasi et al., 2025) or Antares (Adrián-Martínez et al., 2014) are still larger than the measured gamma-ray flux. Improved limits would provide important constraints on the hadronic or leptonic nature of the gamma radiation.

2. Interpretation

High-energy gamma-ray emission is usually produced through the interaction of energetic particles with their environment. Two types of scenarios are usually invoked: leptonic ones involving energetic electrons and positrons, and hadronic ones involving ions. Energetic electrons and positrons interact with the ambient radiation fields via the inverse Compton process. They can also interact with neutral ISM and produce gamma-rays via bremsstrahlung radiation. On the other hand, energetic ions propagating in the ISM will undergo inelastic collisions with nuclei and produce gamma-rays (for a general overview, see e.g. Aharonian, 2004).

We can define different categories of models. The first one interprets the gamma-ray emission by the interaction of particles accelerated in the SMBH accretion flow in the neighboring environment (§ VI.A.2.a). The predictions regarding the spectrum, the variability or the size of the source depend on the distance of the acceleration site and the particle transport in the flow as well as the interaction with the ambient radiation fields or target matter. A second category connects the emission to specific objects and accelerators distinct from the SMBH (§ VI.A.2.b and VI.A.2.c). Finally, a third class of models interprets the signal in terms of collective effects from populations of objects in the vicinity of the GC (§ VI.A.2.d). A number of models, in particular those designed after the *Fermi* results, try to account for the broad band spectrum. The rest is more focused on the VHE source interpretation specifically.

a. *Sgr A**. Particles can be accelerated in the SMBH accretion flow or in a putative jet. The IR and X-ray flares prove that non-thermal particle acceleration occurs down to the inner few Schwarzschild radii. Because of the very low luminosity of Sgr A*, the photon field density in the inner accretion flow is not large enough to cause significant photo-absorption of TeV photons. The region is expected to be transparent to VHE γ -rays, particle acceleration and gamma-ray production can therefore occur in the inner accretion flow and be detectable as suggested by Aharonian & Neronov (2005). They propose several radiative mechanisms that could account for the measured TeV luminosity. It is nevertheless likely that particles accelerated in the inner tens of R_S can escape the region and interact further away in the accretion flow or beyond in the nearby ISM. This idea was explored by Liu et al. (2006), who proposed a scenario where protons are accelerated via stochastic acceleration in the turbulent flow in the inner 20 R_S (with a power of 10^{37} erg s $^{-1}$) and interact within 3 pc of Sgr A*. Magnetic reconnection has also been proposed as a mechanism to accelerate particles in the RIAF (Rodríguez-Ramírez et al., 2019). An important consequence of these models is

that time variability of the acceleration is washed out because of propagation timescales. Hence no variability of HESS J1745–290 is to be expected below at least year timescales (Liu et al., 2006), consistent with current observational results. Ballantyne et al. (2007) has showed that a likely site of hadronic interactions is the dense molecular circum-nuclear disk (see § I.D.2). If the TeV emission is produced by ions accelerated in the accretion flow of Sgr A*, it is therefore likely to be as extended as the CND, up to 30'' radius (Linden et al., 2012). While current measurements do not reach the required angular resolution, it is expected that CTAO will be able to resolve it (CTA Consortium et al., 2019).

Accounting for the bright and steep spectrum of 4FGL J1745.6–2859 and the fainter but harder one of HESS J1745–290 requires energy dependent propagation or temporal injection effects. Chernyakova et al. (2011) note that if particles diffuse in the inner GC in a similar manner as CR in the Galaxy, the mean free path of multi-TeV protons will reach pc scales making their propagation ballistic rather than diffusive. An expected consequence is a spectral hardening in the VHE range where the accelerator spectrum is not modified by diffusion, while the GeV emission is brighter and steeper because of particle confinement. Following this idea, Chernyakova et al. (2011) obtain a scenario that can account for most of the *Fermi*/LAT and H.E.S.S. emissions, assuming that particles steadily injected over 10 kyr account for the GeV spectrum while the VHE one requires more recently injected particles, possibly connected with the century old flares seen through X-ray reflection (see § V.C). Following this idea, Guo et al. (2013) propose a model where most of the particles would be injected during a recent acceleration episode linked to a past Sgr A* flare. IC emission of the electron population would account for the *Fermi*/LAT emission while hadronic emission account for the VHE signal. A consequence of such a model would be a long-term decrease of the GC source flux which has not been observed so far. This idea is supported by the results of Malyshev et al. (2015) showing that the spectrum of the source below 200 MeV is not consistent with a pure hadronic contribution.

b. The PWN candidate G359.95–0.04. Discovered with *Chandra* by Wang et al. (2006b), G359.95–0.04 is a cometary non-thermal X-ray structure located only 7'' away from Sgr A*. It displays clear spectral cooling from the head to the tail, making it a likely ram-pressure confined PWN. It is detected by *NuSTAR* above 40 keV demonstrating the presence of very high energy electrons in the nebula (Mori et al., 2015). With an X-ray synchrotron luminosity of $\sim 10^{34}$ erg s $^{-1}$, it is a plausible origin of the TeV emission provided inverse Compton emission is the dominant radiative process to account for the higher TeV luminosity. Hinton & Aharonian (2007)

have modeled its emission with a magnetic field of about 100 μ G and a far-IR radiation energy density of up to 5000 eV cm $^{-3}$. A key question for the association of HESS J1745–290 and G359.95–0.04 is therefore the intensity of the magnetic field that produces the X-ray emission. The measurement of radio pulses associated with the magnetar SGR J1745–2900 suggests that the ambient magnetic field could be as large as the mG level (Eatough et al., 2013, see also the discussion in § IV.A.3). Such a high field would make synchrotron the dominant radiative process and strongly suppress the expected gamma-ray emission (Kistler, 2015). Irrespective of this aspect, inverse Compton emission from G359.95–0.04 fails short of explaining the high luminosity of the GeV source 4FGL J1745.6–2859 (Cafardo et al., 2021).

c. Sgr A East. It is a bright radio supernova remnant shell filled with intense X-ray plasma emission located behind Sgr A*. It has been discussed in detail in § III.C. It was initially discussed as the counterpart of the EGRET GC gamma-ray source (Melia et al., 1998; Pohl, 2005). Given its age and its interaction with the nearby 50 km s $^{-1}$ cloud, Sgr A East is reminiscent of GeV gamma-ray bright evolved SNRs in the Galaxy, which could make it a plausible gamma-ray emitter (Acero et al., 2016b). Yet, based on the incompatibility of the measured size and position of HESS J1745–290 with Sgr A East morphology, Acero et al. (2010) have discarded it as a plausible counterpart of the TeV source (see also Fig. 22). Similarly, while the extension upper limit of 4FGL J1745.6–2859 is consistent with the SNR size, Cafardo et al. (2021) have argued that its position is markedly offset from the barycenter of the radio emission hence making the association with the GeV source unlikely as well.

d. Collection of sources. The central cluster should contain a large number of neutron stars, among which millisecond pulsars (MSP). Relativistic leptons accelerated above the TeV in the winds of these pulsars should produce VHE emission through inverse Compton scattering over the intense radiation field in the region. Bednarek & Sobczak (2013) estimate that energetic leptons from a population of around 100 such pulsars could explain the VHE GC source flux. Because of the strong losses, the diffusion distance of these leptons is limited to a few pc at most, consistent with the measured constraint on the source extension. Cumulative emission from the magnetospheric emission of the MSPs could account for the measured GeV flux, but their typical spectrum falls off quickly above few GeV. Whether the combination of the two components can account for the spectrum measured in the 10–100 GeV range remains to be tested (Cafardo et al., 2021).

B. GC HE and VHE gamma-ray discrete sources

In addition to the GC source, there are 4 *Fermi*/LAT sources within 1° from Sgr A* and 26 within 2° . While the majority is unidentified, a few are associated with extragalactic objects as well as a couple of foreground pulsars (Abdollahi et al., 2020). Similarly, the H.E.S.S. catalog contains 4 objects in the region.

We briefly review below three of these objects, two pulsar wind nebulae (§ VI.B.1 and VI.B.2) and a bright extended region of GeV–TeV emission: HESS J1745–303 and 4FGL J1745.8–3028e (§ VI.B.3).

1. G0.9+0.1 and its pulsar wind nebula

G0.9+0.1 was first identified as a composite radio supernova with 20-cm VLA observations (Helfand & Becker, 1987). The diameter of the radio shell is $8'$ while the one of the compact radio nebula is $2'$. Non-thermal X-ray emission from the nebula was observed with *BeppoSAX*, confirming it is a PWN (Mereghetti et al., 1998; Sidoli et al., 2000). *Chandra* resolved the emission of the G0.9+0.1 PWN and revealed an arc and jet-like feature as well as a plausible pulsar candidate (Gaensler et al., 2001). Radio pulsations were detected with the GBT (Camilo et al., 2009). PSR J1747–2809 has a period of 52 ms, a spin-down age of 5.3 kyr and a spin-down luminosity of $\dot{E} = 4.3 \times 10^{37}$ erg s $^{-1}$, one of the largest in the Galaxy. The large dispersion measure observed suggests that the pulsar is at the GC distance or beyond. This is confirmed by interstellar X-ray absorption measurement ($N_H \sim 10^{23}$ cm $^{-2}$) (Porquet et al., 2003a; Sidoli et al., 2000). The electron density model of Yao et al. (2017) yields a distance of 8.14 kpc for this pulsar (Manchester et al., 2005). Assuming a distance of 8.5 kpc, the PWN radio luminosity is $\sim 1.2 \times 10^{35}$ erg s $^{-1}$ (Dubner et al., 2008) and its 2–10 keV luminosity is $L_X \sim 4.7 \times 10^{34}$ erg s $^{-1}$ (Porquet et al., 2003a), both values consistent with a young nebula powered by PSR J1747–2809.

VHE emission from G0.9+0.1 was detected by H.E.S.S. (see top panel of Fig. 23). HESS J1747–281 was found to be spatially coincident with the PWN and point-like, excluding the SNR shell as a possible origin of the γ -rays (Aharonian et al., 2005). The spectrum was fitted with a power-law of index 2.4 ± 0.11 . Assuming a distance of 8.5 kpc, the gamma-ray luminosity above 200 GeV is $L_\gamma \sim 2 \times 10^{34}$ erg s $^{-1}$. These results were confirmed by subsequent observations with MAGIC (Ahnen et al., 2017; MAGIC Collaboration et al., 2020) and VERITAS (Adams et al., 2021; Archer et al., 2016) who found compatible source parameters, but no coincident HE source was found by the *Fermi*/LAT (Abdollahi et al., 2020). The VHE emission is well explained by inverse Compton emission of energetic electrons in the PWN (see Fiori

et al., 2020, and references therein).

2. Radio Arc gamma-ray source

There is evidence of the existence of a gamma-ray source located in the vicinity of the GC Radio Arc based on EGRET data (Pohl, 2005). The *Fermi*/LAT has confirmed the existence of such a source: 4 FGL J1746.4–2852 is located within the arc at $l = 0.15^\circ \pm 0.02^\circ$ and $b = -0.12^\circ \pm 0.02^\circ$. Its spectrum is significantly curved and becomes soft above a few GeV. Its luminosity is $L(> 1 \text{ GeV}) \sim 10^{35}$ erg s $^{-1}$ (Abdollahi et al., 2020).

IACTs have also detected gamma-ray emission in the vicinity of the GC Radio Arc: VER J1746–289 for VERITAS (Archer et al., 2016), HESS J1746–285 for H.E.S.S. (H.E.S.S. Collaboration et al., 2018a) and the “Arc” for MAGIC (Ahnen et al., 2017). This emission lies on top of a molecular complex, its measured characteristics, both morphological and spectral, are therefore strongly sensitive to the energy range and to the diffuse emission model (see § VI.C) used to extract them (if any) because of the different levels of contamination. The source spectrum measured by H.E.S.S. is found to be rather hard, a power-law of index ~ 2 and its luminosity is $L(0.35\text{--}10 \text{ TeV}) \sim 7 \times 10^{33}$ erg s $^{-1}$ (H.E.S.S. Collaboration et al., 2018a). Its position at $l = 0.14^\circ \pm 0.01^\circ$ and $b = -0.11^\circ \pm 0.01^\circ$ is found to be coincident with the PWN candidate G0.13–0.11 (note that there is an additional positional uncertainty due to the contribution of the underlying diffuse gamma-ray emission and the way it is modeled).

G0.13–0.11, an X-ray thread on the edge of the GC Radio Arc and the 6.4 keV line emitting molecular cloud G0.11–0.11, was first detected with *Chandra* (Yusef-Zadeh et al., 2002a). Its emission consists in a filamentary emission aligned with the Radio Arc and a point like emission, both having very hard non-thermal spectra. G0.13–0.11 was interpreted as the leading edge of a pulsar wind nebula, produced by a pulsar moving in a strong magnetic field environment (Wang et al., 2002b). Additional *Chandra* and *NuSTAR* observations have confirmed this scenario and revealed emission extending up to the hard X-ray domain (Zhang et al., 2020). The overall luminosity of G0.13–0.11 is $(12.0 \pm 0.3) \times 10^{33}$ erg s $^{-1}$ in the 2–79 keV range. The point source (CXOGCS J174621.5–285256) has a very hard spectrum of index $\Gamma = 1.4 \pm 0.5$, which makes it a plausible pulsar candidate albeit no pulsations were observed so far. The filament is very elongated with a dimension of $40'' \times 2''$ or $1.6 \text{ pc} \times 0.07 \text{ pc}$ at the GC distance. The X-ray flux decreases with distance from the pulsar candidate consistent with electrons radiating their energy as they propagate away from the pulsar. Yet, the spectral index along the filament is in the range 1.5–1.8 without significant evidence of spectral cooling with distance from the point

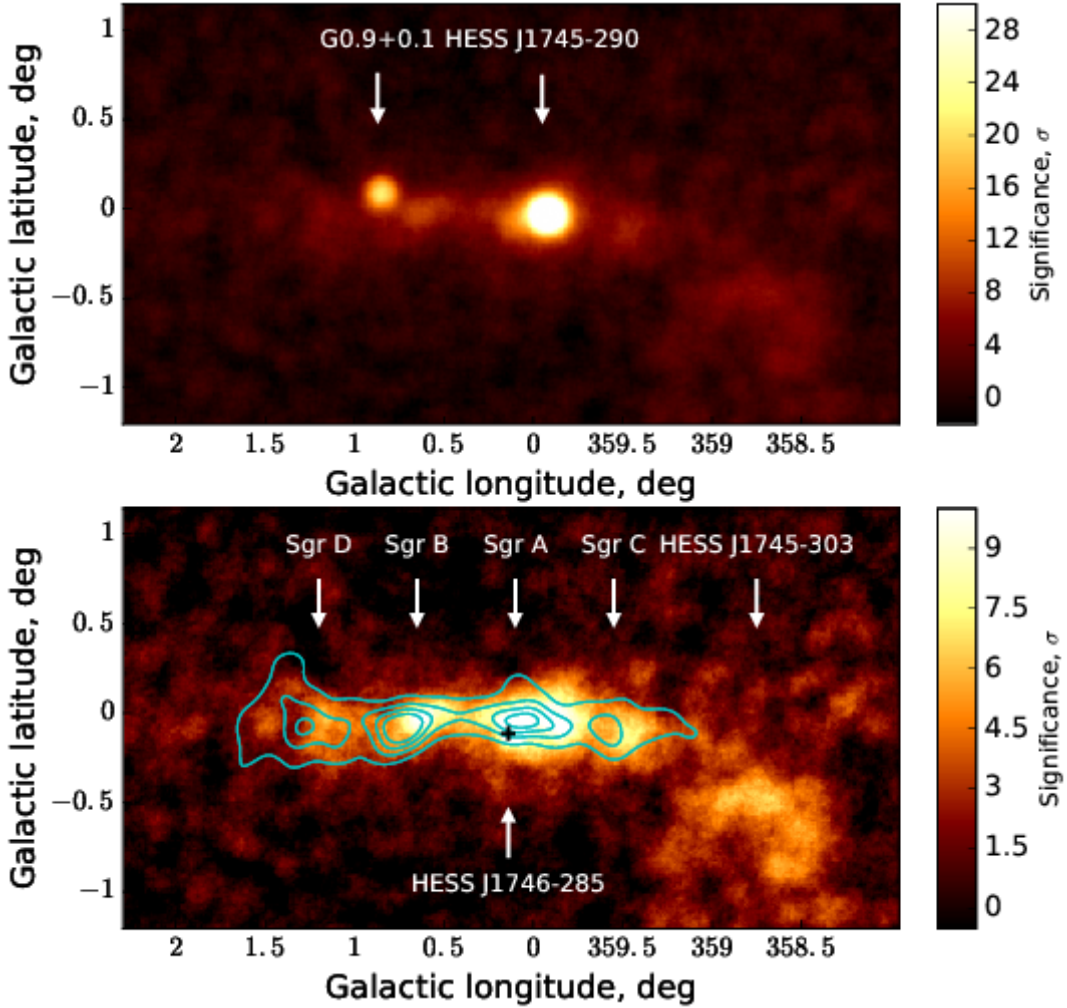


FIG. 23 Upper panel: Significance map of the CMZ seen by H.E.S.S. above 400 GeV. The emission is dominated by two point sources: HESS J1745–290, the source at the GC position, and G0.9+0.1 a pulsar wind nebula. Lower panel: Same map after subtraction of the two point sources. The residual diffuse emission is distributed following the dense gas distribution as traced by the CS molecule (cyan contours from Tsuboi et al. 1999). Figure from H.E.S.S. Collaboration et al. (2018a), reproduced with permission © ESO.

source (Zhang et al., 2020). The dimensions of the filament allows to place constraints on the magnetic field: the length of the filament imposes that the field as to be below $300 \mu\text{G}$ while its thickness implies $B \geq 20 \mu\text{G}$ (Wang et al., 2002b).

Recently, a high degree of polarization of the 3–6 keV emission of G0.13–0.11 has been measured ($57 \pm 18\%$) with *IXPE*. The polarization angle is approximately perpendicular to the non-thermal radio filaments (Churazov et al., 2024). This proves that the X-ray emission is synchrotron emission of electrons propagating along magnetic field lines traced by the filaments.

While the GeV luminosity is much larger than the X-ray and VHE gamma-ray luminosities, the latter are comparable. With the intense radiation fields produced by the nearby Quintuplet cluster, the energetic electrons powering the nebula could produce the observed

VHE gamma-ray emission via inverse-Compton scattering. Yet the contribution of the nebula to the GeV emission is likely too low to explain its flux (H.E.S.S. Collaboration et al., 2018a).

3. HESS J1745–303 and 4FGL J1745.8–3028e

The region around $(l, b) = (358.5^\circ, -1^\circ)$ is a complex γ -ray emitting region with several confused sources with complex morphologies from ~ 100 MeV to the multi-TeV region. An unidentified EGRET source, 3EG J1744–301, was first found in this region (Hartman et al., 1999). A VHE counterpart, HESS J1745–303, was discovered in good spatial coincidence with the EGRET source (Aharonian et al., 2006b). Aharonian et al. (2008b) have resolved its complex morphology into several hotspots.

And the source was finally resolved in two distinct objects in the HGPS. The first, HESS J1745–303, is centered on ($l=358.65^\circ$, $b=-0.56^\circ$) and has a radius of 0.18° . The second, HESS J1746–308, is centered on $l=358.44^\circ$, $b=-1.11^\circ$ and has a radius of 0.16° . Their spectra are steep with power-law indices respectively of 2.56 ± 0.06 and 3.27 ± 0.22 (H.E.S.S. Collaboration et al., 2018b). *Fermi*/LAT observations of the GeV source, 4FGL J1745.8–3028e, found its morphology is well modeled by a disk of radius 0.53° centered on ($l=358.44^\circ$, $b=-1.11^\circ$) which overlaps both VHE sources (Abdollahi et al., 2020). Its spectrum is modeled by a power-law of index 2.20, consistent with a spectral softening occurring between the GeV and TeV domains. A second *Fermi*/LAT source, 2FHL J1745.1–3035, has been revealed in the catalog of objects detected above 50 GeV (Ackermann et al., 2016). Being centered on ($l=358.53^\circ$, $b=-0.78^\circ$), it lies on the edges of HESS J1745–303, but its very hard spectral, with an index of 1.2 ± 0.4 suggests an additional distinct object (Marchesi et al., 2024).

The brightest of the VHE component, HESS J1745–303, is found to partly overlap the large radio shell SNR G359.1–0.5. At the GC distance, its angular size would result in a unrealistic physical size of 60 pc. G359.1–0.5 must therefore lie in front of the GC. Recent observations suggest a distance of ~ 4 kpc (Eppens et al., 2020; Suzuki et al., 2020). The presence of OH masers indicates the shell interacts with molecular gas. The interaction of CR accelerated at the shock with the dense gas might therefore produce the observed VHE γ -rays. The absence of any clear X-ray counterpart in *XMM-Newton* (Aharonian et al., 2008b) and *Suzaku* (Bamba et al., 2009) supports such a scenario. The latter paper also revealed an excess of 6.4 keV line emission suggesting the presence of dense gas. Yet, no clear correlation is found between the TeV emission and CO clouds in the vicinity of the remnant (Eppens et al., 2020; Suzuki et al., 2020). Recently, Marchesi et al. (2024) have discovered a very-hard compact, yet slightly extended ($5''$ in *Chandra* images) non-thermal X-ray source spatially coincident with 2FHL J1745.1–3035. They argue this could be a young PWN system, where the compact nebula would power the hard *Fermi* source while the softer and more extended component (HESS J1745–303 and 4FGL J1745.8–3028e) could be explained by an older diffuse hadronic component.

C. Diffuse HE and VHE gamma-ray emission from the CMZ

1. An excess of multi-TeV cosmic rays in the CMZ

In 2006, the H.E.S.S. Collaboration reported on the detection of a diffuse emission of VHE gamma rays extending for about 2° along the Galactic disk and roughly cen-

tered around the GC (Aharonian et al., 2006a). The diffuse emission is quite faint in terms of brightness. Thus, its detection required a relatively long exposure (55 hours of observations) and the subtraction of the two known discrete VHE sources in the region: HESS J1745–290 (see § VI.A) and G0.9+0.1 (see § VI.B). As shown in the bottom panel of Fig. 23, at Galactic longitudes in the range $|l| \lesssim 1^\circ$, the morphology of the VHE diffuse emission (taken from H.E.S.S. Collaboration et al. 2018a) follows quite closely the distribution of dense gas in the CMZ, as traced by CS line emission (Tsuboi et al., 1999). This spatial correlation points towards a hadronic origin of the VHE emission, i.e., gamma rays are generated in the decay of neutral pions produced by interactions between CR nuclei and ambient matter in the CMZ. While multi-TeV CR electrons might also produce VHE radiation through inverse Compton scattering (Yusef-Zadeh et al., 2007) or non-thermal Bremsstrahlung emission (Yusef-Zadeh et al., 2013), the very short radiative loss time of such particles (mainly due to synchrotron emission, see e.g. H.E.S.S. Collaboration et al. 2016) would prevent them to propagate away from their sources and spread over a region as large as the CMZ. A leptonic origin for the VHE emission seems then disfavored.

If the emission is indeed hadronic, the intensity and spectrum of CR nuclei in that region can be derived from gamma-ray data and from the knowledge of the gas mass distribution in the CMZ. The energy density of multi-TeV CRs measured in this way exceeds by a factor of 3 to 9 the one measured in the Solar neighbourhood. Moreover, the spectrum of CRs in the CMZ is significantly harder (slope of the differential energy distribution close to 2.3, Aharonian et al. 2006a) than that of the local interstellar spectrum (slope close to 2.7, see e.g. Gabici et al. 2019). These observations can be explained by invoking the presence of an additional population of energetic particles emerging in the TeV domain above the sea of CRs that pervades the entire Galactic disk.

2. Origin of the diffuse emission: impulsive cosmic-ray source?

The diffuse gamma-ray emission was initially detected at photon energies exceeding ~ 400 GeV (Aharonian et al., 2006a). Such photons are produced in interactions of CR nuclei of energy larger than ~ 4 TeV/nucleon (e.g. Aharonian, 2004), and in order to explain the observed diffuse gamma-ray flux such particles must carry an overall energy of $\sim 10^{49}$ erg. This estimate increases to $\sim 10^{50}$ erg if the CR spectrum is extrapolated down to the GeV domain. For this reason, the H.E.S.S. Collaboration initially suggested that the additional CR component in the CMZ might be accelerated by a single supernova explosion, provided that about 10% of the typical supernova explosion energy (which is $\sim 10^{51}$ erg) is converted into CR nuclei.

At the distance of the GC, the angular extent of the diffuse gamma-ray emission corresponds to a physical extent of few hundred parsecs. The large physical extent suggests that observations are best explained by assuming that CRs were produced in the past at an accelerator located somewhere in the GC region, and that they then escaped the production site and diffused away, filling a volume much larger than the one of the accelerator itself. The injection of CRs must have happened recently enough, otherwise the accelerated particles would have diffused well beyond the boundaries of the CMZ, and would be nowadays too diluted to produce any appreciable gamma-ray emission. This result is truly remarkable, as it was the first time that the presence of a CR accelerator in the Galaxy was revealed indirectly through the emission produced by runaway CRs, a strategy suggested long ago by Aharonian & Atoyan (1996).

The morphology of the diffuse gamma-ray emission provides tight constraints on where and when the hypothetical supernova explosion might have taken place. With this respect, in Aharonian et al. (2006a) it was noticed that the spatial correlation between gamma-ray emission and gas distribution degrades at Galactic longitudes $l > 1^\circ$, where a peak in the gas distribution at $l \sim 1.3^\circ$ does not correspond to an enhancement in the gamma-ray flux (see Fig. 23). If the supernova exploded t years ago, and was located close to the GC, the CRs that were injected into the CMZ had time to diffuse and spread over a region of size $R_{\text{diff}} \sim \sqrt{2a D t}$, where D is the spatial diffusion coefficient of multi-TeV CRs, and a accounts for the dimensionality of diffusion ($a = 1$ corresponds to 1D diffusion along a magnetic flux tube, and $a = 3$ to isotropic 3D diffusion). This expression can be inverted to derive the supernova explosion time, which is $t \sim 3 \times 10^3 (a \eta)^{-1}$ yr, where it was assumed that CRs are spread over a region of apparent size of 1° around the GC, and that $D = 10^{30} \eta \text{ cm}^2/\text{s}$, where the numerical factor represents the characteristic diffusion coefficient in the Galactic disk for multi-TeV CRs (e.g. Gabici et al., 2019), and η accounts for possible deviations from this value.

A natural candidate CR accelerator in the region is the supernova remnant Sgr A East, located within the inner few parsecs around the GC (see § III.C.2 and Maeda et al. 2002). The age of the remnant was initially estimated to be of the order of $\approx 10^4$ yr (Ehlerová et al., 2022; Maeda et al., 2002) which would require a suppressed diffusion coefficient ($\eta \ll 1$). This might be indeed plausible, given the highly turbulent environment in the GC region. However, according to other studies the estimated age should be reduced to $\approx 10^3$ yr (Fryer et al., 2006; Rockefeller et al., 2005; Zhang et al., 2023), which would be consistent with an ordinary value ($\eta \sim 1$) of the diffusion coefficient. As we will see below, the hypothesis of a single impulsive source originating the CRs responsible for the VHE diffuse emission is now disfavored, and there-

fore we do not comment further on the discrepancies in the estimated age of Sgr A East.

3. The morphology of the emission is best explained by a continuous cosmic-ray source at the GC

Following Aharonian et al. (2006a), further observations of the CMZ in VHE gamma rays were carried out by the Cherenkov telescope arrays H.E.S.S. (H.E.S.S. Collaboration et al., 2018a, 2016), MAGIC (MAGIC Collaboration et al., 2020), and VERITAS (Archer et al., 2016). In particular, the most recent results obtained by H.E.S.S. and presented in H.E.S.S. Collaboration et al. (2016) and H.E.S.S. Collaboration et al. (2018a) were based on much deeper exposures obtained after 226 and 259 hours of observations, respectively. Therefore, a more accurate reconstruction of the morphology of the gamma-ray emission became possible.

Based on such improved study of the morphology of the emission, an alternative interpretation of the deficit of VHE emission observed at the peak in mass distribution located at $l \sim 1.3^\circ$ was presented in H.E.S.S. Collaboration et al. (2016). In that work, the spatial distribution of multi-TeV CRs was inferred from the estimate of the gas mass integrated along the line of sight and from the VHE emission from a number of regions distributed along the CMZ. The excess in the energy density of multi-TeV CRs found in Aharonian et al. (2006a) was confirmed, and the morphology of the gamma-ray emission could be reproduced by a density of CRs declining away from the GC roughly as $\sim 1/R$, R being the distance from the GC (the best $1/r^\alpha$ fit to data is obtained for $\alpha = 1.1$, H.E.S.S. Collaboration et al. 2016). Within this framework, the deficit of VHE emission from the region located at $l \sim 1.3^\circ$ is not due to the inability of CRs to reach such a distance after escaping from a source located in the GC, but rather to a gradual decline of their energy density.

A $\sim 1/R$ decline is suggestive of a quasi-continuous injection of CRs over an extended period of time taking place very close to the GC. If multi-TeV CRs are injected at a constant rate \dot{Q}_{CR} at the GC ($R = 0$) and then undergo isotropic and homogeneous spatial diffusion ($a = 3$), their number density as a function of the radial coordinate and at a time t is indeed $n \sim (\dot{Q}_{CR}/4\pi DR) \propto 1/R$ for $R < R_{\text{diff}}$. The continuous injection of CRs has to last a time Δt larger than the CR diffusion time, up to at least $l \sim 1.3^\circ$, which implies $\Delta t > 2 \times 10^3 \eta^{-1}$ yr. The rate at which CR nuclei have to be injected in order to explain the VHE flux is $\dot{Q}_{CR}(> 10 \text{ TeV}) \sim 4 \times 10^{37} \eta \text{ erg s}^{-1}$. Interestingly, within this framework a strict upper limit on the value of both the diffusion coefficient and the injection rate can be obtained by recalling that the diffusive approximation breaks down when the diffusion time $\tau_{\text{diff}} \sim R^2/6D$ becomes comparable or smaller than the crossing time $\tau_{\text{cross}} \sim R/c$, where R is the size of the

region under examination. Imposing $\tau_{\text{diff}} > \tau_{\text{cross}}$ gives $\eta \lesssim 3$ which implies $\dot{Q}_{\text{CR}}(> 10 \text{ TeV}) \lesssim 3 \times 10^{38} \text{ erg/s}$ (H.E.S.S. Collaboration et al., 2016).

The most detailed analysis of the diffuse VHE emission from the CMZ was presented in the most recent publication by the H.E.S.S. Collaboration et al. (2018a), from which Fig. 23 is taken. Thanks to the improved statistics, individual molecular cloud complexes within the CMZ are now clearly resolved (Sgr B2, C and D, as indicated by the labels in the figure).

A template-based likelihood fit analysis of the data confirmed that most of the diffuse emission correlates with the distribution of very dense gas as traced by the CS emission, and that a strong (negative) gradient is present in the spatial distribution of CRs away from the GC. This further supports the evidence for a CR accelerator located at the GC. However, the fit to the data requires the existence of an additional large-scale component, that does not correlate with and is more extended in latitude than the CS gas template. One possibility is that such component might be generated by the interaction of CRs with molecular hydrogen in a diffuse phase, characterised by a comparatively lower density ($\sim 100 \text{ cm}^{-3}$), which is not mapped by CS emission but could account for about a third of the entire molecular matter in the region (Dahmen et al., 1998). This shows that accurate estimates of the global energy requirement to explain the gamma-ray emission from the CMZ can be obtained only by combining information on the mass distribution coming from different tracers.

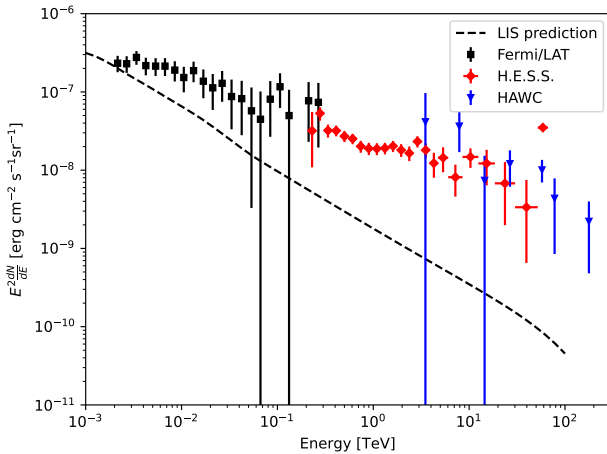


FIG. 24 Broadband SED of the gamma-ray diffuse emission at the GC extracted in a 0.45° annulus centered around Sgr A* as reported by Gaggero et al. (2017), by H.E.S.S. Collaboration et al. (2016) and by Albert et al. (2024). The extrapolated contribution from HESS J1745–290 has been subtracted from the HAWC flux points. The dashed line shows the predicted SED assuming the CR density measured in the local interstellar (LIS) medium.

4. A cosmic-ray PeVatron at the GC?

The measurement of the VHE gamma-ray spectrum of the CMZ attracted much interest as it was suggested that its extension to very large energies could imply the presence of a CR PeVatron, i.e., an accelerator capable of accelerating particles up to the PeV domain, in the GC (H.E.S.S. Collaboration et al., 2016). The acceleration of particles up to PeV energies is a central issue in cosmic-ray physics, as explanations of the observed spectrum of CRs require that Galactic accelerators must be able to accelerate protons to at least several PeVs, but the nature of such accelerators is not known (e.g. Gabici et al., 2019).

The spectrum of the diffuse emission was found to be quite hard, and could be described well by a pure power law of photon index ~ 2.3 (Aharonian et al., 2006a). Its extension up to photon energies of several tens of TeV suggests that the spectrum of the CR protons responsible for the emission likely extends up to at least a fraction of PeV, and possibly even beyond that. Otherwise, deviations from a pure power-law behaviour should have been observed in the gamma-ray spectrum (H.E.S.S. Collaboration et al., 2018a, 2016).

Extending the observations to larger photon energies is crucial in order to better characterise the spectral shape of the gamma-ray emission and to constrain the maximum energy of the parent CR protons. This was recently done thanks to the data collected over 7 years by HAWC, which extend the observed spectral range to photon energies exceeding 100 TeV (Albert et al., 2024). The HAWC Collaboration reported on the detection of a source, named HAWC J1745–290, coincident with the GC region and characterised by a maximum significance above the background at the 6.5σ level. Observations can be explained by a point-like gamma-ray source (68% confidence level upper limit on the size of 0.48°) exhibiting a steep power-law spectrum of photon index ~ 2.9 .

A comparison between HAWC and H.E.S.S. observations of the CMZ is not straightforward, mainly due to the very different angular resolutions of the two instruments, but also to the different energy ranges probed. Indeed, two H.E.S.S. sources (Sgr A* and the Radio Arc, see § VI.A and VI.B, respectively) are found within the upper-limit angular extension of HAWC J1745–290. For this reason, the gamma-ray emission from the CMZ was estimated by the HAWC Collaboration by subtracting the flux of these two H.E.S.S. sources (extrapolated up to $\gtrsim 100$ TeV photon energies) from that of HAWC J1745–290. When this is done, the H.E.S.S. and HAWC fluxes are well compatible at $\gtrsim 10$ TeV photon energies (see Fig. 24), but the spectrum estimated by HAWC is markedly steeper than the one measured by H.E.S.S. within a very similar region around the GC. As HAWC is more sensitive at higher photon energies, the difference in the measured slopes suggests that the gamma-ray spectrum of the CMZ is not described by

a pure power law, but is rather curved. The presence of a curvature in the spectrum is also supported by a recent preliminary analysis of the most recent H.E.S.S. data (presented at the 8th Heidelberg International Symposium on High-Energy Gamma-Ray Astronomy). Even though not conclusive, these latest results put into question the existence of a CR PeVatron in the GC region. The presence or not of a spectral steepening will also impact dramatically on the expectations of future detections of the GC region with neutrino telescopes such as Baikal-GVD (Belolaptikov et al., 2022) or KM3NeT (Adrián-Martínez et al., 2016), which are most sensitive in the multi-TeV/PeV energy domain. Neutrinos are produced in the very same hadronic interactions that produce the observed VHE photons and, in the absence of a spectral suppression, the GC region should be detected after 5 to 10 years of exposure (Celli et al., 2017; Guo et al., 2017).

5. What is the nature of the accelerator?

In any case, whether or not the maximum energy of CRs in the CMZ reaches the nominal value of 1 PeV, gamma-ray data tell us that a powerful CR accelerator is present in that region. Remarkably, as discussed above, the morphology of the gamma-ray emission requires an injection of CRs located very close (less than ≈ 10 pc) to the GC (H.E.S.S. Collaboration et al., 2016). This disfavors a number of potential accelerators, including the Arches and Quintuplet star clusters (located just outside of the region of interest, see e.g. Genzel et al. 2010 and § I.C.3), the radio filaments (see § IV.B and Yusef-Zadeh et al., 2013), or hypothetical discrete sources distributed throughout the entire CMZ (e.g. Wommer et al., 2008). The SNR Sgr A East is placed within the inner 10 pc but, as said above, it would most likely inject CRs in an impulsive event, rather than in a continuous (or quasi-continuous) manner, as required by the brightness profile of gamma rays. The YNC is also located very close to the GC, and should therefore considered a possible candidate for particle acceleration (see Gabici 2024 for a review on CR acceleration in stellar clusters). The recent detection of UHE gamma rays from the direction of stellar clusters reported by LHAASO (notably the OB association Cygnus OB2, Lhaaso Collaboration 2024, and the young star forming region W43, Cao et al. 2025) provides support to the idea that the YNC might power the diffuse very-high-energy gamma-ray emission observed from the CMZ. Intriguingly, another plausible candidate is the central SMBH and its immediate surroundings. The explanation of gamma-ray observations would require the conversion of a fraction of the energy associated to accretion/ejection phenomena around the SMBH into relativistic particles.

Observations of the CMZ in the VHE domain do not

suffice to constrain the global energetic associated with CRs. This is because for CR spectra steeper than E^{-2} the bulk of the energy is carried by \approx GeV particles. Therefore, HE (GeV photon energies) observations of the CMZ are needed. An analysis of *Fermi* data showed that the spectrum of the gamma-ray emission from the CMZ region can be described reasonably well by a single power law extending from the GeV to the multi-TeV domain (see Fig. 24 and Gaggero et al., 2017).

Remarkably, as indicated in Fig. 24, at multi-GeV photon energies, the flux is just a factor of $\lesssim 2$ larger than what one would expect from the interaction between the Galactic CR nuclei that pervade the entire Galaxy (assumed to have an intensity roughly equal to the one measured locally) and the dense ambient gas (Ravikularaman et al., 2025; Scherer & Cuadra, 2024). However, CRs with a spectral energy distribution similar to the local (near Earth) one would produce a gamma-ray emission from the CMZ characterised by a spectrum much steeper than the observed one. This fact prompted Gaggero et al. (2017) to propose that at least part of the gamma-ray emission from the CMZ could be explained if the Galactic CRs have a harder spectrum close to the GC. Indeed, a progressive hardening of the Galactic CR spectrum towards the GC is required to explain *Fermi* observations of the Galactic diffuse emission (Acero et al., 2016a; Pothast et al., 2018; Yang et al., 2016), but including this effect would not eliminate the need of a CR source located at the GC, but only reduce slightly its power (Gaggero et al., 2017).

Various estimates of the CR power associated to the (unknown) central source exist, and they mostly converge to values of $\sim 10^{38}$ – 10^{39} erg s $^{-1}$ (Crocker et al., 2011; Dörner et al., 2024; H.E.S.S. Collaboration et al., 2016; Macias et al., 2015; Ravikularaman et al., 2025; Yoast-Hull et al., 2014). This is a few orders of magnitude larger than the current bolometric luminosity of Sgr A* ($\sim 10^{36}$ erg s $^{-1}$), indicating that the SMBH environment (if responsible for the acceleration of particles) might be much more effective in producing CRs rather than photons. On the other hand, the required CR power is much smaller than the mechanical power needed to inflate the giant *Fermi* and *eROSITA* bubbles (Predehl et al., 2020; Su et al., 2010), which has been estimated to be $\sim 10^{41}$ erg s $^{-1}$, and significantly smaller than the mechanical power of $\lesssim 10^{40}$ erg s $^{-1}$ needed to excavate the X-ray chimneys (Ponti et al., 2019 and § V.B.5), i.e., the exhaust channels through which matter and energy flows from the GC into the bubbles (see Sarkar, 2024, for a review). This implies that, while the nature of the particle accelerator is still unknown, the energy reservoir for non-thermal particles is certainly not an issue.

In fact, as pointed out by Jouvin et al. (2017), it is probably more interesting to compare the required CR power with some sort of minimum available mechanical power in the region. A few percent of the massive star

formation of the entire Galaxy takes place in the GC region (see § I). The supernova explosion rate is correspondingly enhanced and is estimated to be, with large uncertainty, equal to $\approx 4 \times 10^{-4} \text{ yr}^{-1}$ within few hundred parsec from the GC (Crocker et al., 2011; Jouvin et al., 2017; Ponti et al., 2015b). Assuming that each supernova releases 10^{51} erg in form of mechanical energy and that, as required by CR observations in the Galaxy, $\sim 10\%$ of such energy is converted into CRs (e.g. Gabici et al., 2019), one gets a CR power of $\sim 10^{40} \text{ erg s}^{-1}$, which actually exceeds the power required to explain the gamma-ray emission from the CMZ (Jouvin et al., 2017, 2020). Therefore, instead of asking what is the origin of the CR excess in the CMZ, one should rather wonder why is the excess so small. Remarkably, a fast removal of CRs from the CMZ region, either due to a star-formation induced wind (Crocker & Aharonian, 2011; Su et al., 2010) or to AGN-like activity events at the SMBH (Guo & Mathews, 2012; Su et al., 2010), would provide a natural link between the GC and the giant bubbles detected by *Fermi* and *eROSITA*.

D. Gamma-ray emission from the Galactic bulge

The *Fermi* GeV excess and the 511 keV line emission are both peaked within the Galactic center region considered in this review but their roughly spherically symmetric signals extend much further out, likely covering the entire bulge of our Galaxy. Since the origin of these features are not yet understood and may be related with the activity at the GC, we briefly summarize their characteristics and mention the models evoking a possible connections with the center and between them.

1. The *Fermi* GeV excess

After subtracting all known discrete sources and diffuse components from the *Fermi*/LAT data, Goodenough & Hooper (2009) first revealed an excess of emission at GeV energies in the inner degrees of our Galaxy, the so-called *Fermi* GeV excess. The need for a extra component to fit the *Fermi*/LAT data has remained true for all independent analyses performed ever since, leading to a very significant detection of this excess (see Murgia, 2020, for a review). However, models of the gamma-ray sky used in these analyses are subject to many uncertainties (see e.g. Ackermann et al., 2017; Calore et al., 2015) and the precise description of the *Fermi* GeV excess, in particular of its morphology, is therefore still debated.

The most robust characteristic is its spectrum. The excess is significantly detected between 1 and 10 GeV with a peak at $\sim 1\text{--}3 \text{ GeV}$ (Abazajian et al., 2014; Ajello et al., 2016; Calore et al., 2015; Daylan et al., 2016; Gordon & Macías, 2013; Hooper & Slatyer, 2013). The presence of

the excess above and below the 1–10 GeV energy range is more uncertain (see discussion in Murgia, 2020). The *Fermi* GeV excess extends at least 10° away from the dynamical center of the Galaxy and its spectrum is almost uniform across this extent (e.g. Calore et al., 2015; Daylan et al., 2016). Nevertheless, there is no consensus on the spatial morphology of the *Fermi* GeV excess. Several descriptions have been proposed, and the main competing models are either a spherically symmetric morphology (Cholis et al., 2022; McDermott et al., 2023; Murgia, 2020, and references therein) or a bulge-like morphology (Bartels et al., 2018; Macías et al., 2018), they are also pointing to two different origins for the *Fermi* GeV excess.

Dark matter annihilation was the first interpretation proposed for the excess (Goodenough & Hooper, 2009). This scenario has since been largely explored and remains viable. Dark matter particles with a mass $\sim 60 \text{ GeV}$ annihilating with a velocity-averaged cross section of $\sim 4 \times 10^{-26} \text{ cm}^3 \text{ s}^{-1}$ would produce a diffuse spherically-symmetric signal having the same spectral properties than the excess (Di Mauro & Winkler, 2021; Murgia, 2020, and references therein). On the other hand, the cumulative emission of unresolved point sources distributed as the old stellar population of the bulge could also explain the *Fermi* GeV excess (e.g. Bartels et al., 2016; Calore et al., 2021; Lee et al., 2016; List et al., 2021). After Abazajian (2011) showed that the spectra of several globular clusters match the one of the *Fermi* GeV excess, millisecond pulsars, which are gamma-ray emitters known to be present in these clusters and that could also be present in the Galactic bulge, became natural candidates (e.g. Abazajian & Kaplinghat, 2012; Brandt & Kocsis, 2015; Gautam et al., 2022; Gordon & Macías, 2013). Despite on-going extensive searches for bulge MSPs, this population has not been discovered yet, possibly due to the difficulty of detecting fast pulsation for distant sources with high dispersion measures (see e.g. Calore et al., 2016). DM and MSPs are currently the two main competing scenarios, but other interpretations involving cosmic-ray outbursts from the central region have also been proposed (see Murgia, 2020, for more details).

2. The 511 keV emission line

The celestial emission from electron-positron annihilation (see Prantzos et al., 2011, for a review) produces a pure gamma-ray line at 511 keV (the electron rest mass energy) or a line mixed with a lower-energy continuum, when the process goes through formation of positronium. It was detected from outside the solar system as early as the 1970s from the general direction of the GC, by low-energy resolution balloon-borne instruments (Johnson et al., 1972) and then studied with high resolution Ge detectors (Leventhal et al., 1978). Many experiments

have tried to constrain the properties of the emission and to derive the sources of positron production, their power and the location of the annihilation. They established that the radiation is steady, mainly diffuse and extending over the Galactic bulge. The most precise results are from the *INTEGRAL* SPI (Churazov et al., 2020; Knödlseder et al., 2005; Siegert, 2023; Siegert et al., 2016). The emission appears centered at the GC, but shifted by $\approx 1^\circ$ towards negative longitudes, and extends with a Gaussian shape of $\approx 8^\circ$ FWHM width (even if two Gaussian components of widths $\approx 20^\circ$ and 6° better fit the data) encompassing the GB. An additional point-like component, centered on Sgr A*, could also be present in the data, but with low significance. A Galactic disk component, 24° FWHM wide in latitude and without longitudinal asymmetries, was instead clearly, and for the first time, unambiguously detected. The 511 keV fluxes are respectively (8.9–10.1), (13.1–20.1) and (0.6–1.2) in units of 10^{-4} ph cm $^{-2}$ s $^{-1}$ for the bulge, disk, and central source, respectively. The flux ratio between the bulge and the disk results in a luminosity ratio of 1.0 ± 0.1 , which is a very high ratio compared with what is seen at other wavelengths. High-resolution spectroscopy of the line shows that it is well centered at 511 keV with a width of 2.6 keV (but it could be a mixture of a broad line of 5 keV FWHM and a narrow one of 1 keV width) and a large positronium fraction, compatible with 1.0. This suggests that the annihilation of positrons occurs mostly at low (\approx keV) energies, and mainly in a warm ISM with gas temperature of 7000–40000 K and ionization state of 2–25%. These data imply a (model-dependent) estimate of the e $^+$ annihilation rate of $2\text{--}3 \times 10^{43}$ e $^+$ s $^{-1}$ in both bulge and disk components (e.g. Siegert, 2023).

Positrons are typically produced at mildly or highly-relativistic energies and they are expected to propagate through the ISM on timescales of 0.1–10 Myr along path lengths of 0.1–10 kpc from their initial sources (Siegert, 2023). Therefore the measured morphology is certainly a smeared-out image of the initial source distribution due to the propagation effects and the distribution of the gas where they annihilate. The observed flux of MeV γ -rays from the inner Galaxy also constrains the initial energy of the bulk of the positrons to less than a few MeV, otherwise the continuum emission from in-flight annihilation, i.e. before positron thermalization, would exceed the observed flux. Due to these elements, the large uncertainties of the measurements and the source and background model dependence of the results, the origin of the emission is still not understood (Prantzos et al., 2011; Siegert, 2023), and the large GB/GD ratio is particularly hard to explain. The main sources of e $^+$ considered include β^+ -radioactivity from isotopes generated by nucleo-synthesis processes in stars, both in steady and in explosive phases (SNe, hypernovae, novae), but also particle interactions or photon pair productions taking place close to compact objects such as pulsars, magnetars, XRBs or GNs, and

even processes involving DM.

The case for Sgr A* to be a contributor to this emission has been recently re-discussed by Jean et al. (2017) who studied the propagation of emitted positrons from the SMBH into the bulge. This has been first suggested in the 1980s, but was considered as unlikely given the present very-low level of activity of Sgr A* (Riegler et al., 1981). When the possibility of large past activity of the BH emerged, a model for pair production in the hot RIAF plasma of Sgr A*, assumed to accrete at larger rate in the past, was proposed by Totani (2006) who claimed that this process could explain the required e $^+$ production rate. Alternatively, a large amount of accelerated particles can be produced by the SMBH when accretion increases drastically during stellar TDE that are expected on time scales of $10^{4\text{--}5}$ yr, depending on the star mass (Cheng et al., 2006, 2007). In the latter work, the authors found that TDEs of low-mass stars by the SMBH, would liberate $\approx 10^{52}$ erg in positrons through p-p interactions and following pion decays, at a rate of one per 10^5 yr. The repeated events over 10 million years and the following propagation of e $^+$ would allow to fill the bulge with low-energy positrons that then annihilate in its warm ionized medium, giving the observed 511 keV line emission and associated continuum. Indeed, considering the different propagation effects in the zones encountered from the GC to the GB, Jean et al. (2017) showed that an outburst of $10^{52\text{--}53}$ erg of MeV positrons from Sgr A*, occurring $10^{5\text{--}6}$ years ago, can explain the latest measurements of the 511 keV line emission in the broad bulge.

Models invoking DM to produce the 511 keV emission, as for the SMBH models, allow for the large GB/GD ratio of the signal, due to the expected DM concentration towards the GN (see Boehm, 2009; Prantzos et al., 2011, for reviews and references). Viable such models for the GB 511 keV line involve either de-excitation of weakly interactive massive particles (1 GeV – 1 TeV), possibly the same than those invoked for the *Fermi* GeV excess, that have been excited to energies above the ground state of \approx few MeV, or annihilation of light DM particles (< 10 MeV). In this case, the disk component could be explained by nucleo-synthetic products or other stellar contributions. However, detailed predictions are scarce because the properties of the DM particles are unknown.

In spite of the large amount of data collected on the two GB components of the Galactic gamma-ray emission, the GeV excess and the 511 keV line emission, their origins are still a puzzle and the link between them remains unclear. New generations of instruments may help elucidate this relation in the future (§ VII).

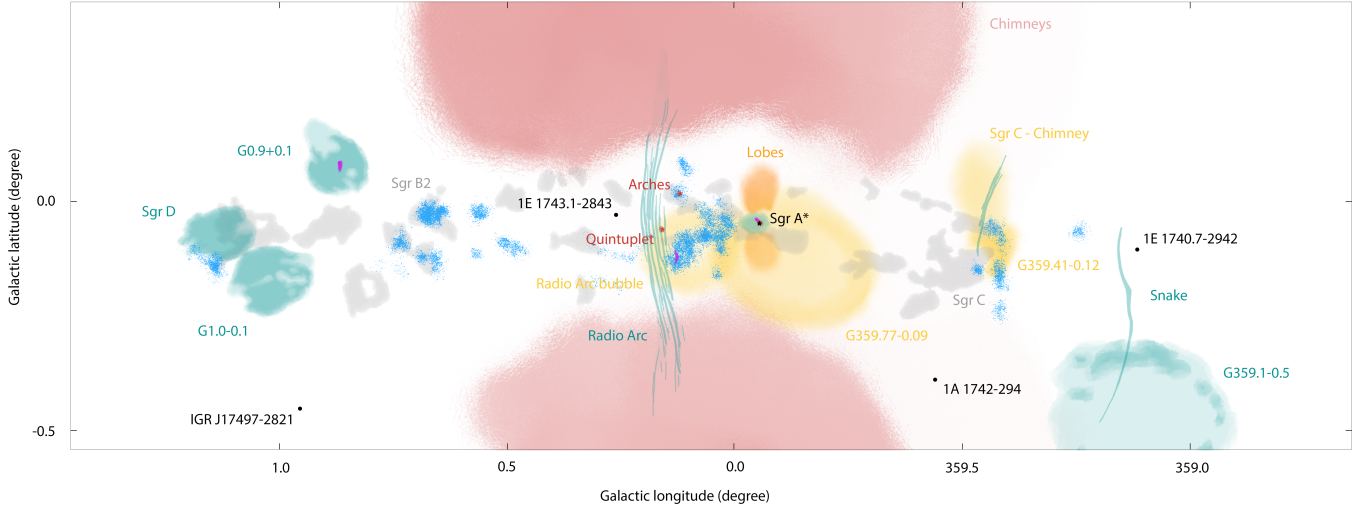


FIG. 25 Map of Galactic center features discussed in this review. The location of Sgr A* and of a selection of X-ray point sources is shown in black (star and points). Diffuse X-ray thermal structures are drawn in yellow, orange and pink (e.g. Radio Arc bubble, Lobes and Chimneys, see § V.B). Reflection features detected at 6.4 keV are shown in patchy blue (see § V.C). The three young stellar clusters are shown in red (YSC, Arches and Quintuplet clusters, see § IV.C). Three PWNe possibly associated with gamma-ray counterparts are highlighted in purple (G359.95–0.04, G013–0.11 and the one within G0.9+0.1, see § IV.B and VI). To help the comparison with maps at other wavelength presented in § I, radio SNR (emitting in X-rays, e.g. Sgr A East and Sgr D) plus a selection of radio non-thermal filaments (e.g. Radio Arc) are drawn in teal, and a catalog of molecular clouds from the CMZ is shown in light grey (e.g. Sgr B2 and Sgr C). See Fig. 26 for a close-up of the inner region.

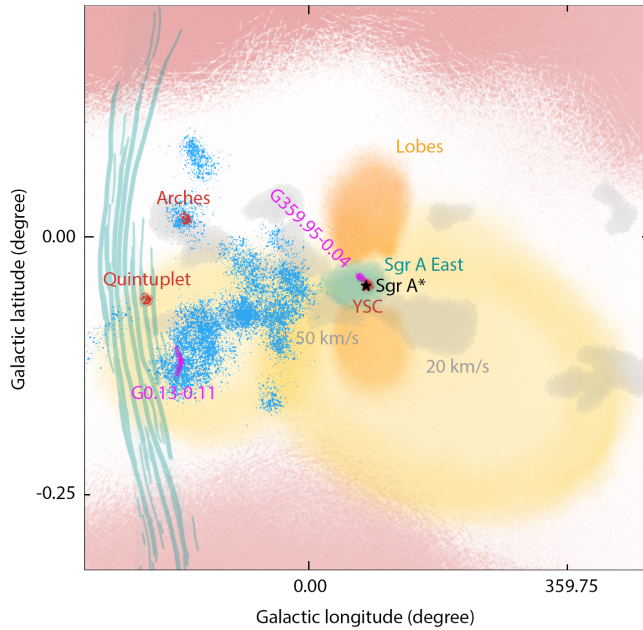


FIG. 26 Map of the inner Galactic center features, see caption of Fig. 25 for more details.

VII. CONCLUSIONS AND PERSPECTIVES

The HE emission from the GC is prominent and very complex. It is produced by thermal and non-thermal processes in many different discrete and diffuse sources, superposing, and sometimes interacting, with each other

in the narrow sky region of the CMZ. Figures 25 and 26 present a summary finding chart of the main features discussed in this review and in particular of the HE sources studied in the last 25 yr with the present generation of X-ray and gamma-ray observatories, with references to the sections where they are described.

A. Summary and open questions

Sgr A* is currently characterised by a very weak ($\sim 10^{-11} L_E$), persistent thermal X-ray emission, likely powered by the accretion flow fed by the YNC stellar winds. This makes it the best prototype of a very low accretion rate BH system, but the detailed characteristics of the plasma flow and, especially, the form of the outflows that seem to dominate it, are not yet understood. The X-ray emission increases by up to a couple of orders of magnitudes during flares, which happens at a daily rate and last at most few hours. Their variability timescale implies that they are produced very close ($< 20 R_S$) to the BH horizon, and their spectrum is non-thermal. Detected also at IR frequencies, their broad-band emission may be due to synchrotron emission of a population of relativistic electrons possibly generated at transient magnetic reconnection events. Their origin is still not understood.

Although rather quiet today, the GC was very active in the past. A direct proof of that came from the discovery of variability of the non-thermal diffuse X-ray emission

(iron 6.4 keV line) from the GC MCs. The emission is dominated by reflection of past X-ray outbursts emitted less than 1 kyr ago most likely by Sgr A*. Each outburst had a duration in the range 1-10 yr and released an energy of $\approx 10^{46}\text{--}10^{48}$ erg. Also in this case, the origin of these outbursts is not known. If connected to Sgr A*, explaining the bursts would require a large (but short) accretion (Low Luminosity AGN - like) of material into the SMBH.

Several signatures of more ancient eruptions and/or outflows originated in the very center of the CMZ have been revealed by the deep X-ray surveys of the region and by their extensions in the polar directions. They include, from the very center outwards, two symmetrical polar 15-pc lobes, two not axi-symmetric 50-pc superbubbles (one towards the Radio Arc the other in the SW direction) and finally two 150-pc polar chimneys. The energy involved in these outflows ranges from 10^{50} up to 10^{52} erg for the larger structures. Their origin is not fully clear, with both SF events and BH activity as possible explanations.

Other hints for the presence of very energetic events taking place in the GC region, and not necessarily related to the presence of the SMBH, come from the extremely large gas ionisation rates measured within the CMZ, and from the possible presence of a hot ($kT \approx 7$ keV) diffuse plasma in the region. The origin of the large ionisation rates remains puzzling. Ionisation by LECRs seems to be the most plausible scenario, but it requires an exceedingly large energy input in form of CR particles ($\approx 10^{40}\text{--}10^{41}$ erg/s). The presence of a hot plasma might explain the residual 6.7 keV line diffuse X-ray emission, which is mostly but probably not entirely due to unresolved mCv and non-mCv. Maintaining this hot plasma would require an energy input of the order of 10^{53} erg to be refilled on a time scale of about 10^4 yr if not bounded to the GC, and a strong toroidal magnetic field to confine it within the CMZ. We note that the energy input might be partly spread over the entire GC region

Given all these evidences for the availability of a large energy reservoir, it is somewhat odd that the excess of high-energy CRs in the GC region, deduced from the TeV gamma-ray diffuse emission of the CMZ, is very modest. This implies that CRs are likely evacuated very rapidly from the CMZ, due to either a wind driven by star formation or AGN activity at the SMBH. The morphology of the diffuse gamma-ray emission indicates that a powerful accelerator of CRs is present within the inner 10 pc of the Galaxy, injecting continuously energetic particles for at least thousands of years. The source, whose nature is still debated, was believed to be a CR proton PeVatron, i.e. an extreme Galactic particle accelerator, but recent data cast doubts on this hypothesis.

B. Future observations of the GC region

New X-ray observables will be essential for progress. In particular, high resolution micro-calorimeter spectroscopy (as provided by *XRISM* and *NewAthena*) will be decisive for characterizing the present and past emission of Sgr A*.

Plasma line diagnostics of its quiescent emission will further constrain the physics of the accretion flow on the SMBH, although achieving this will require good angular resolution observations as well to disentangle Sgr A* from the neighbouring plasma components. In addition, while X-ray polarimetry appears a very promising tool to constrain properties of Sgr A* echoes, high resolution spectroscopy of illuminated clouds will further constrain the geometry of the reflections and will enable velocity measurements. This will provide robust associations with ISM tracers and will be key to determine the number, timing and energetics of past outbursts.

High resolution spectroscopy will also improve our understanding of diffuse thermal emissions in the CMZ. Measurements of the diffuse He-like Fe line emission will probe its signatures of rotation around the GC constraining the respective roles of unresolved stellar systems and the hot ISM phase. More generally, detailed line diagnostics will allow measurements of bulk motions, gas expansion velocities, and turbulences along the LoS, thereby setting constraints on the physical parameters of the soft X-ray diffuse sources.

Understanding the mechanisms causing Sgr A* flares and their radiation, will require further coordinated MWC involving new generation instruments from sub-mm to NIR coupled with next generation X-ray telescopes providing large effective area and high angular resolution.

The next generation gamma-ray observatories, such as CTAO, will provide a precise location and extension of the GC gamma-ray source which, in addition to long term monitoring of its emission will be crucial to determine its nature. Emission from Sgr A* flares might be detectable thanks to improved sensitivity around 100 GeV. Determining the location and nature of the CR accelerator in the CMZ will be made possible by the improved energy resolution and energy coverage of the diffuse gamma-ray emission.

A new generation MeV mission would also be essential to measure the GC source spectrum below the pion bump to constrain the radiation processes at play as well as characterize the positron annihilation bulge emission properties. It could also observe nuclear line signatures of low energy CR interactions in the CMZ and help solve the mystery of the very large ionisation rate in the region. With this respect, progresses might also come from alternative and more robust ways to estimate the cosmic-ray ionisation rate, based on the study of infrared H₂ rovibrational lines from dense clouds. This is feasible in the

local ISM with JWST and might be applicable to the CMZ as well.

C. Link to the Galaxy: SMBH activity or Star Formation?

One of the key question is of course what level of feedback the GC exerts on the MW and whether HE observations of the GC can help to answer this question. To do so, it is necessary to establish the link between the GC features and the large Galactic polar structures which are the strongest signs of nuclear outflows.

The *Fermi* bubbles (FB) are gigantic elliptical lobes of HE gamma-ray emission extending from the central regions in both polar directions for 8–10 kpc along the rotation axis of the MW (Su et al., 2010). The symmetry of their morphology and their sharp edges imply they are powered from the central regions and the mechanical energy of the process is estimated to 10^{54} erg over timescales of the order of 10^6 yr or more. They are enveloped by the thermal X-ray *eROSITA* bubbles, that extend for 12–14 kpc, implying larger energies (10^{56} erg), timescales (10 Myr) and power (10^{41} erg s $^{-1}$, Predehl et al., 2020).

The HE GC features most connected to the FEB are certainly the soft X-ray chimneys, which rise to their bases, and have been suggested to trace the channels through which energy is injected from the GC in the FEB outflows. However the estimated power of the chimneys is at least one order of magnitude lower than the lower estimate of the FB power. It is possible that repeated events occurred and what is seen is the carved residual of the last event while the FEB accumulated the energy of several events along a long period. The smaller structures are difficult to reconnect to the giant polar outflows producing the FEB, but the 15-pc lobes could represent part of the same process giving rise to the chimneys (Ponti et al., 2019). As discussed in § VI.C.5, both the central gamma-ray source and the accelerator responsible for the gamma-ray diffuse emission are rather under-luminous compared to the powers needed to fill the FEB and even to explain the chimneys. However as the source and processes generating the CR that produce the gamma-rays are not identified yet, it is difficult to conclude on their relation with the outflows. As discussed in § VI.C, the existing estimates of the power needed by the central accelerator to produce the diffuse gamma-rays in the CMZ are 2–3 orders of magnitude lower than the FB power. Since the expected CR power in the CMZ should be of the order of the FB power, it has been proposed that processes (either SF winds or AGN-like outflows) rapidly remove CR out of the GC, possibly feeding the FB. Searches for an observational connection between the GC TeV emission and the bases of the FEB are in progress with H.E.S.S. and certainly foreseen with CTAO.

Moving on even larger scales, giant (≈ 200 kpc) X-ray

halos have been recently revealed by *eROSITA* around Milky Way-like galaxies (Zhang et al., 2024), and the presence of a gamma-ray halo of similar size has been reported, based on *Fermi* observations, for Andromeda (Karwin et al., 2019). A similar halo might exist also around the Milky Way, and phenomena related to the GC activity might play a role in explaining its characteristics (Recchia et al., 2021).

As discussed in § VI.D, if the large Sgr A* activity could release a fraction of the energy to power the production of 10^{52} erg in MeV positrons, this event could also generate the bulge component of the Galactic 511 keV emission, which GC SF processes may have difficulty to explain. A prototype of *COSI* has recently flown on a balloon and provided results on the bulge 511 keV emission that indicate a more extended morphology (width of $\approx 30^\circ$) than the one derived from *INTEGRAL* data (Kierans et al., 2020). Although these results need to be confirmed, improved designs of devices such as *COSI* may provide new important results that can contribute to resolve the mystery of the Galactic 511 keV emission and clarify its relation with the GC and the activity of the SMBH.

As a final comment, we remark that if all the central features, their energies and timescales, are attributed to the SMBH, the history of the Sgr A* activity in the past can be reconstructed. From the present $< 10^{-8}$ L_E (quiescent and flaring state), it was at $\approx 10^{-5}$ L_E about 300 yr ago (MC echoes), liberated $\approx 10^{-3}$ L_E about 10^4 yr before (15-pc lobes), then $\approx 10^{-2}$ L_E about 10^5 yr ago (chimneys) and finally $\approx 10^{-1}$ L_E more than 1 Myr ago (FB).

Clearly more data and more theoretical efforts are needed to understand what is going on in the center of the MW and its link with the whole Galaxy, and HE observations are crucial in these exploratory programs. The collection of new observatories progressively set in operation over the next 10–15 yr, working in synergy with those operating at low frequencies and in the multi-messenger domain, and in particular with SKA, ALMA, EHT, GRAVITY+, *JWST*, KM3Net and *LISA* between others, will hopefully clarify a number of key issues as discussed above.

Appendix A: Abbreviations, acronyms and conventions

In this manuscript we use a number of abbreviations and acronyms, which we list here with their definition. Observatories are named using their acronyms (known in the community) and for the HE ones we explicitly give the main references in the text (§ II). These contain further references, in particular for the instruments. Space observatory names are in italics, and instruments are reported after a separation slash: *Observatory*/Instrument.

AB	coronally Active Binary
ADAF	Advection Dominated Accretion Flow
BH	Black Hole
CCD	Charge Coupled Device
CDF	Cumulative Distribution Function
CMZ	Central Molecular Zone
CND	Circum-Nuclear Disk or Ring
CR	Cosmic Rays
(m)CV	(magnetic) Cataclysmic Variable
DM	Dark Matter
EW	Equivalent Width
FB	Fermi Bubbles
FEB	Fermi eRosita Bubbles
FoV	Field of View
FWHM	Full Width Half Maximum
GB	Galactic Bulge
GC	Galactic Center
GD	Galactic Disk (intended as thin GD)
(A)GN	(Active) Galactic Nucleus
GR	General Relativity
GRXE	Galactic Ridge X-ray Emission
HE	High-Energy
HED/P/W	Half Energy Diameter / Power / Width
(M)HD	(Magneto) Hydro Dynamics
(E)IC	(External) Inverse Compton
IMBH	Intermediate Mass Black Hole
IMF	Initial Mass Function
IP	Intermediate Polars
ISM	Interstellar Medium
(N/M/F)IR	(Near/Mid/Far) Infrared
LECRe/p	Low Energy CR electrons/protons
LMXB	Low Mass X-ray Binary
LoS	Line of Sight
MAD	Magnetically Arrested Disk
(G)MC	(Giant) Molecular Cloud
MSP	Millisecond Pulsar
MW	Milky Way (the Galaxy)
MWC	Multi-Wavelength Campaign
NB	Nuclear Bulge
NS	Neutron Star
NSC	Nuclear Star Cluster
NSD	Nuclear Stellar Disc
NTF	radio Non-Thermal Filament
PSF	Point Spread Function
PWN	Pulsar Wind Nebula
RIAF	Radiative Inefficient Accretion Flow
SANE	Standard and Normal Evolution
SED	Spectral Energy Distribution
SF(R)	Star Formation (Rate)
SMBH	Supermassive Black Hole
SMD	Stellar Mass Distribution
SN(R)	Supernova (Remnant)

SSC	Syncrotron Self inverse Compton
SYN	Synchrotron
TDE	Tidal Disruption Event
UHE	Ultra High Energy (gamma-ray)
UV	Ultra-Violet
VHE	Very High Energy (gamma-ray)
YNC	Young Nuclear Cluster
x1 / x2	orbit types induced by the bar
XRB	X-Ray Binary
XVP	<i>Chandra</i> X-ray Visionary Project
WD	White Dwarf
WR	Wolf Rayet
2D / 3D	two / three Dimension

ACKNOWLEDGMENTS

The authors acknowledge the Centre National d'Études Spatiales (CNES) for financial support. SG acknowledges support from Agence Nationale de la Recherche (grant ANR-21-CE31-0028). We thank the referees for the careful reading of the manuscript and the valuable suggestions that have improved the paper. This paper employs a list of Chandra data-sets, obtained by the Chandra X-ray Observatory, contained in the Chandra Data Collection (CDC) 369 doi:10.25574/cdc.369.

REFERENCES

Abazajian, K. N. 2011, *J. Cosmology Astropart. Phys.*, 2011, 010

Abazajian, K. N., Canac, N., Horiuchi, S., & Kaplinghat, M. 2014, *Phys. Rev. D*, 90, 023526

Abazajian, K. N. & Kaplinghat, M. 2012, *Phys. Rev. D*, 86, 083511

Abbasi, R., Ackermann, M., Adams, J., et al. 2025, arXiv e-prints, arXiv:2501.16440

Abdollahi, S., Acero, F., Ackermann, M., et al. 2020, *ApJS*, 247, 33

Abeysekara, A. U., Albert, A., Alfaro, R., et al. 2023, *Nuclear Instruments and Methods in Physics Research A*, 1052, 168253

Acero, F., Ackermann, M., Ajello, M., et al. 2016a, *ApJS*, 223, 26

Acero, F., Ackermann, M., Ajello, M., et al. 2016b, *ApJS*, 224, 8

Acero, F., Aharonian, F., Akhperjanian, A. G., et al. 2010, *MNRAS*, 402, 1877

Ackermann, M., Ajello, M., Albert, A., et al. 2017, *ApJ*, 840, 43

Ackermann, M., Ajello, M., Atwood, W. B., et al. 2016, *ApJS*, 222, 5

Adams, C. B., Benbow, W., Brill, A., et al. 2021, *ApJ*, 913, 115

Adrián-Martínez, S., Ageron, M., Aharonian, F., et al. 2016, *Journal of Physics G Nuclear Physics*, 43, 084001

Adrián-Martínez, S., Albert, A., André, M., et al. 2014, *ApJ*, 786, L5

Aharonian, F., Akhperjanian, A. G., Anton, G., et al. 2009, *A&A*, 503, 817

Aharonian, F., Akhperjanian, A. G., Aye, K.-M., et al. 2004, *A&A*, 425, L13

Aharonian, F., Akhperjanian, A. G., Aye, K.-M., et al. 2005, *A&A*, 432, L25

Aharonian, F., Akhperjanian, A. G., Barres de Almeida, U., et al. 2008a, *A&A*, 492, L25

Aharonian, F., Akhperjanian, A. G., Barres de Almeida, U., et al. 2008b, *A&A*, 483, 509

Aharonian, F., Akhperjanian, A. G., Bazer-Bachi, A. R., et al. 2006a, *Nature*, 439, 695

Aharonian, F., Akhperjanian, A. G., Bazer-Bachi, A. R., et al. 2006b, *ApJ*, 636, 777

Aharonian, F. & Neronov, A. 2005, *ApJ*, 619, 306

Aharonian, F. A. 2004, Very high energy cosmic gamma radiation : a crucial window on the extreme Universe

Aharonian, F. A. & Atoyan, A. M. 1996, *A&A*, 309, 917

Ahnen, M. L., Ansoldi, S., Antonelli, L. A., et al. 2017, *A&A*, 601, A33

Aitken, D. K., Greaves, J., Chrysostomou, A., et al. 2000, *ApJ*, 534, L173

Ajello, M., Albert, A., Atwood, W. B., et al. 2016, *ApJ*, 819, 44

Albert, A., Alfaro, R., Alvarez, C., et al. 2024, *ApJ*, 973, L34

Albert, J., Aliu, E., Anderhub, H., et al. 2006, *ApJ*, 638, L101

Alboslani, D., Battersby, C., Brunker, S. W., et al. 2025, *AJ*, 169, 213

Aleksić, J., Ansoldi, S., Antonelli, L. A., et al. 2016, *Astroparticle Physics*, 72, 76

Alexander, T. 2005, *Phys. Rep.*, 419, 65

Anastasopoulou, K., Ponti, G., Sormani, M. C., et al. 2023, *A&A*, 671, A55

Andrés, A., van den Eijnden, J., Degenaar, N., et al. 2022, *MNRAS*, 510, 2851

Archer, A., Benbow, W., Bird, R., et al. 2016, *ApJ*, 821, 129

Atwood, W. B., Abdo, A. A., Ackermann, M., et al. 2009, *ApJ*, 697, 1071

Baganoff, F. K., Bautz, M. W., Brandt, W. N., et al. 2001, *Nature*, 413, 45

Baganoff, F. K., Maeda, Y., Morris, M., et al. 2003, *ApJ*, 591, 891

Bahramian, A. & Degenaar, N. 2023, in *Handbook of X-ray and Gamma-ray Astrophysics*, 120

Balakrishnan, M., Corrales, L., Markoff, S., et al. 2024, *ApJ*, 974, 98

Balick, B. & Brown, R. L. 1974, *ApJ*, 194, 265

Ballantyne, D. R., Melia, F., Liu, S., & Crocker, R. M. 2007, *ApJ*, 657, L13

Bamba, A., Yamazaki, R., Kohri, K., et al. 2009, *ApJ*, 691, 1854

Barrière, N. M., Tomsick, J. A., Baganoff, F. K., et al. 2014, *ApJ*, 786, 46

Bartels, R., Krishnamurthy, S., & Weniger, C. 2016, *Phys. Rev. Lett.*, 116, 051102

Bartels, R., Storm, E., Weniger, C., & Calore, F. 2018, *Nature Astronomy*, 2, 819

Battersby, C., Walker, D. L., Barnes, A., et al. 2025, *ApJ*, 984, 156

Bednarek, W. & Sobczak, T. 2013, *MNRAS*, 435, L14

Bélanger, G., Goldwurm, A., Goldoni, P., et al. 2004, *ApJ*, 601, L163

Bélanger, G., Goldwurm, A., Melia, F., et al. 2005, *ApJ*, 635, 1095

Bélanger, G., Goldwurm, A., Renaud, M., et al. 2006a, *ApJ*, 636, 275

Bélanger, G., Terrier, R., de Jager, O. C., Goldwurm, A., & Melia, F. 2006b, in *Journal of Physics Conference Series*, Vol. 54, *Journal of Physics Conference Series*, ed. R. Schödel, G. C. Bower, M. P. Munoz, S. Nayakshin, & T. Ott (IOP), 420–426

Belolaptikov, I., Dzhilkibaev, Z. A. M., Allakhverdyan, V. A., et al. 2022, in *37th International Cosmic Ray Conference*, 2

Berteaud, J., Calore, F., Clavel, M., et al. 2021, *Phys. Rev. D*, 104, 043007

Bignami, G. F., Fichtel, C. E., Kniffen, D. A., & Thompson, D. J. 1975, *ApJ*, 199, 54

Blank, M., Morris, M. R., Frank, A., Carroll-Nellenback, J. J., & Duschl, W. J. 2016, *MNRAS*, 459, 1721

Blitz, L., Bloemen, J. B. G. M., Hermsen, W., & Bania, T. M. 1985, *A&A*, 143, 267

Boehm, C. 2009, *New Journal of Physics*, 11, 105009

Bortolas, E., Mapelli, M., & Spera, M. 2017, *MNRAS*, 469, 1510

Bouchet, L., Jourdain, E., Roques, J.-P., et al. 2008, *ApJ*, 679, 1315

Bouchet, L., Mandrou, P., Roques, J. P., et al. 1991, *ApJ*, 383, L45

Bouffard, É., Haggard, D., Nowak, M. A., et al. 2019, *ApJ*, 884, 148

Bowyer, S., Byram, E. T., Chubb, T. A., & Friedman, H. 1965, *Science*, 147, 394

Boyce, H., Haggard, D., Witzel, G., et al. 2022, *ApJ*, 931, 7

Boyce, H., Haggard, D., Witzel, G., et al. 2019, *ApJ*, 871, 161

Bradt, H., Narayan, S., Rappaport, S., & Spada, G. 1968, *ApJ*, 152, 1005

Brandt, T. D. & Kocsis, B. 2015, *ApJ*, 812, 15

Brunker, S. W., Battersby, C., Alboslani, D., et al. 2025, *ApJ*, 982, L20

Bryant, A. & Krabbe, A. 2021, *New A Rev.*, 93, 101630

Cafardo, F., Nemmen, R., & Fermi LAT Collaboration. 2021, *ApJ*, 918, 30

Calderón, D., Cuadra, J., Russell, C. M. P., et al. 2025, *A&A*, 693, A180

Calderón, D., Cuadra, J., Schartmann, M., Burkert, A., & Russell, C. M. P. 2020, *ApJ*, 888, L2

Calore, F., Cholis, I., & Weniger, C. 2015, *J. Cosmology Astropart. Phys.*, 2015, 038

Calore, F., Di Mauro, M., Donato, F., Hessels, J. W. T., & Weniger, C. 2016, *ApJ*, 827, 143

Calore, F., Donato, F., & Manconi, S. 2021, *Phys. Rev. Lett.*, 127, 161102

Camilo, F., Ransom, S. M., Gaensler, B. M., & Lorimer, D. R. 2009, *ApJ*, 700, L34

Cao, Z., Aharonian, F., An, Q., et al. 2024, *ApJS*, 271, 25

Cao, Z., Aharonian, F., Axikegu, et al. 2025, *Science China Physics, Mechanics, and Astronomy*, 68, 279502

Capelli, R., Warwick, R. S., Cappelluti, N., et al. 2011, *A&A*, 525, L2

Capelli, R., Warwick, R. S., Porquet, D., Gillessen, S., & Predehl, P. 2012, *A&A*, 545, A35

Celli, S., Palladino, A., & Vissani, F. 2017, *European Physical Journal C*, 77, 66

Cesarsky, C. J. & Volk, H. J. 1978, *A&A*, 70, 367

Chabrier, G. & Dumond, P. 2024, *ApJ*, 966, 48

Cheng, K. S., Chernyshov, D. O., & Dogiel, V. A. 2006, *ApJ*, 645, 1138

Cheng, K. S., Chernyshov, D. O., & Dogiel, V. A. 2007, *A&A*, 473, 351

Chernyakova, M., Malyshev, D., Aharonian, F. A., Crocker, R. M., & Jones, D. I. 2011, *ApJ*, 726, 60

Chernyshov, D. O., Ko, C. M., Krivonos, R. A., Dogiel, V. A., & Cheng, K. S. 2018, *ApJ*, 863, 85

Cholis, I., Zhong, Y.-M., McDermott, S. D., & Surdutovich, J. P. 2022, *Phys. Rev. D*, 105, 103023

Chuard, D., Terrier, R., Goldwurm, A., et al. 2018, *A&A*, 610, A34

Churazov, E., Bouchet, L., Jean, P., et al. 2020, *New A Rev.*, 90, 101548

Churazov, E., Khabibullin, I., Barnouin, T., et al. 2024, *A&A*, 686, A14

Churazov, E., Khabibullin, I., Sunyaev, R., & Ponti, G. 2017, *MNRAS*, 465, 45

Churazov, E., Sunyaev, R., & Sazonov, S. 2002, *MNRAS*, 330, 817

Ciurlo, A., Campbell, R. D., Morris, M. R., et al. 2020, *Nature*, 577, 337

Ciurlo, A. & Morris, M. R. 2026, in *Encyclopedia of Astrophysics*, Vol. 4, 1–18

Ciurlo, A., Morris, M. R., Campbell, R. D., et al. 2021, *ApJ*, 910, 143

Clark, G., Garmire, G., Oda, M., & Wada, M. 1965, *Nature*, 207, 584

Clark, J. S., Patrick, L. R., Najarro, F., Evans, C. J., & Lohr, M. 2021, *A&A*, 649, A43

Clavel, M. 2019, in *SF2A-2019: Proceedings of the Annual meeting of the French Society of Astronomy and Astrophysics*, ed. P. Di Matteo, O. Creevey, A. Crida, G. Kordopatis, J. Malzac, J. B. Marquette, M. N'Diaye, & O. Venot, Di

Clavel, M., Soldi, S., Terrier, R., et al. 2014, *MNRAS*, 443, L129

Clavel, M., Terrier, R., Goldwurm, A., et al. 2013, *A&A*, 558, A32

Corrales, L., Baganoff, F. K., Wang, Q. D., et al. 2020, *ApJ*, 891, 71

Cramphorn, C. K. & Sunyaev, R. A. 2002, *A&A*, 389, 252

Crocker, R. M. & Aharonian, F. 2011, *Phys. Rev. Lett.*, 106, 101102

Crocker, R. M., Jones, D. I., Aharonian, F., et al. 2011, *MNRAS*, 413, 763

Crocker, R. M., Jones, D. I., Melia, F., Ott, J., & Protheroe, R. J. 2010, *Nature*, 463, 65

Crudace, R. G., Fritz, G., Shulman, S., et al. 1978, *ApJ*, 222, L95

CTA Consortium, Acharya, B. S., Agudo, I., et al. 2019, *Science with the Cherenkov Telescope Array*

Cuadra, J., Nayakshin, S., & Martins, F. 2008, *MNRAS*, 383, 458

Cummings, A. C., Stone, E. C., Heikkila, B. C., et al. 2016, *ApJ*, 831, 18

Czerny, B., Kunneriath, D., Karas, V., & Das, T. K. 2013, *A&A*, 555, A97

Dahmen, G., Hüttemeister, S., Wilson, T. L., & Mauersberger, R. 1998, *A&A*, 331, 959

Dalgarno, A. 2006, *Proceedings of the National Academy of Science*, 103, 12269

Daylan, T., Finkbeiner, D. P., Hooper, D., et al. 2016, *Physics of the Dark Universe*, 12, 1

de Naurois, M. & Mazin, D. 2015, *Comptes Rendus Physique*, 16, 610

Degenaar, N., Miller, J. M., Kennea, J., et al. 2013, *ApJ*, 769, 155

Degenaar, N., Wijnands, R., Cackett, E. M., et al. 2012, *A&A*, 545, A49

Degenaar, N., Wijnands, R., Miller, J. M., et al. 2015, *Journal of High Energy Astrophysics*, 7, 137

Deneva, J. S., Cordes, J. M., & Lazio, T. J. W. 2009, *ApJ*, 702, L177

Di Mauro, M. & Winkler, M. W. 2021, *Phys. Rev. D*, 103, 123005

Do, T., Hees, A., Ghez, A., et al. 2019a, *Science*, 365, 664

Do, T., Witzel, G., Gautam, A. K., et al. 2019b, *ApJ*, 882, L27

Dodds-Eden, K., Gillessen, S., Fritz, T. K., et al. 2011, *ApJ*, 728, 37

Dodds-Eden, K., Porquet, D., Trap, G., et al. 2009, *ApJ*, 698, 676

Dogiel, V., Cheng, K.-S., Chernyshov, D., et al. 2009, *PASJ*, 61, 901

Dogiel, V. A., Chernyshov, D. O., Ivlev, A. V., et al. 2018, *ApJ*, 868, 114

Dogiel, V. A., Chernyshov, D. O., Kiselev, A. M., et al. 2015, *ApJ*, 809, 48

Dogiel, V. A., Chernyshov, D. O., Tatischeff, V., Cheng, K.-S., & Terrier, R. 2013, *ApJ*, 771, L43

Dörner, J., Becker Tjus, J., Blomenkamp, P. S., et al. 2024, *ApJ*, 965, 180

Doroshenko, V., Suleimanov, V., Tsygankov, S., et al. 2020, *A&A*, 643, A62

Dubner, G., Giacani, E., & Decourchelle, A. 2008, *A&A*, 487, 1033

Eatough, R. P., Falcke, H., Karuppusamy, R., et al. 2013, *Nature*, 501, 391

Eckart, A., Baganoff, F. K., Morris, M., et al. 2004, *A&A*, 427, 1

Eckart, A., Baganoff, F. K., Zamaninasab, M., et al. 2008, *A&A*, 479, 625

Ehlerová, S., Palouš, J., Morris, M. R., et al. 2022, *A&A*, 668, A124

EHT Collaboration, Akiyama, K., Alberdi, A., et al. 2022a, *ApJ*, 930, L12

EHT Collaboration, Akiyama, K., Alberdi, A., et al. 2022b, *ApJ*, 930, L13

EHT Collaboration, Akiyama, K., Alberdi, A., et al. 2022c, *ApJ*, 930, L16

EHT Collaboration, Akiyama, K., Alberdi, A., et al. 2024, *ApJ*, 964, L25

Eppens, L. K., Reynoso, E. M., Lazendic-Galloway, J., Combi, J. A., & Albacete-Colombo, J. F. 2020, *MNRAS*, 493, 3947

Eyles, C. J., Skinner, G. K., Willmore, A. P., & Rosenberg, F. D. 1975, *Nature*, 257, 291

Falcke, H. & Markoff, S. 2000, *A&A*, 362, 113

Feigelson, E. D., Getman, K., Townsley, L., et al. 2005, *ApJS*, 160, 379

Ferrière, K. 2012, *A&A*, 540, A50

Figer, D. F., McLean, I. S., & Morris, M. 1999, *ApJ*, 514, 202

Fiori, M., Zampieri, L., Burtovoi, A., Caraveo, P., & Tibaldo, L. 2020, *MNRAS*, 499, 3494

Fisher, P. C., Johnson, H. M., Jordan, W. C., Meyerott, A. J., & Acton, L. W. 1966, *ApJ*, 143, 203

Fryer, C. L., Rockefeller, G., Hungerford, A., & Melia, F. 2006, *ApJ*, 638, 786

Gabici, S. 2022, *A&A Rev.*, 30, 4

Gabici, S. 2024, in *7th Heidelberg International Symposium on High-Energy Gamma-Ray Astronomy*, 16

Gabici, S., Evoli, C., Gaggero, D., et al. 2019, International Journal of Modern Physics D, 28, 1930022

Gaensler, B. M., Pivovaroff, M. J., & Garmire, G. P. 2001, ApJ, 556, L107

Gaensler, B. M. & Slane, P. O. 2006, ARA&A, 44, 17

Gaggero, D., Grasso, D., Marinelli, A., Taoso, M., & Urbano, A. 2017, Phys. Rev. Lett., 119, 031101

Gautam, A., Crocker, R. M., Ferrario, L., et al. 2022, Nature Astronomy, 6, 703

Gehrels, N., Chincarini, G., Giommi, P., et al. 2004, ApJ, 611, 1005

Generozov, A., Stone, N. C., Metzger, B. D., & Ostriker, J. P. 2018, MNRAS, 478, 4030

Genzel, R. 2021, in APS Meeting Abstracts, Vol. 2021, APS April Meeting Abstracts, A01.002

Genzel, R., Eisenhauer, F., & Gillessen, S. 2010, Reviews of Modern Physics, 82, 3121

Genzel, R., Schödel, R., Ott, T., et al. 2003, Nature, 425, 934

Genzel, R. & Townes, C. H. 1987, ARA&A, 25, 377

Ghez, A. 2021, in APS Meeting Abstracts, Vol. 2021, APS April Meeting Abstracts, A01.003

Ghez, A. M., Wright, S. A., Matthews, K., et al. 2004, ApJ, 601, L159

Gillessen, S., Genzel, R., Fritz, T. K., et al. 2013, ApJ, 774, 44

Gillessen, S., Genzel, R., Fritz, T. K., et al. 2012, Nature, 481, 51

Ginsburg, A., Henkel, C., Ao, Y., et al. 2016, A&A, 586, A50

Goldwurm, A., Brion, E., Goldoni, P., et al. 2003, ApJ, 584, 751

Goldwurm, A., Cordier, B., Paul, J., et al. 1994, Nature, 371, 589

Goldwurm, A. & Gros, A. 2022, in Handbook of X-ray and Gamma-ray Astrophysics, ed. C. Bambi & A. Sanganello, 15

Goodenough, L. & Hooper, D. 2009, arXiv e-prints, arXiv:0910.2998

Gordon, C. & Macías, O. 2013, Phys. Rev. D, 88, 083521

Goto, M., Geballe, T. R., Indriolo, N., et al. 2014, ApJ, 786, 96

GRAVITY Collaboration, Abuter, R., Aimar, N., et al. 2023, A&A, 677, L10

GRAVITY Collaboration, Abuter, R., Aimar, N., et al. 2022, A&A, 657, L12

GRAVITY Collaboration, Abuter, R., Amorim, A., et al. 2018a, A&A, 615, L15

GRAVITY Collaboration, Abuter, R., Amorim, A., et al. 2021, A&A, 654, A22

GRAVITY Collaboration, Abuter, R., Amorim, A., et al. 2020a, A&A, 638, A2

GRAVITY Collaboration, Abuter, R., Amorim, A., et al. 2020b, A&A, 636, L5

GRAVITY Collaboration, Abuter, R., Amorim, A., et al. 2018b, A&A, 618, L10

GRAVITY Collaboration, Abuter, R., Amorim, A., et al. 2019, A&A, 625, L10

Guillochon, J., McCourt, M., Chen, X., Johnson, M. D., & Berger, E. 2016, ApJ, 822, 48

Guo, F. & Mathews, W. G. 2012, ApJ, 756, 181

Guo, Y.-Q., Tian, Z., Wang, Z., Li, H.-J., & Chen, T.-L. 2017, ApJ, 836, 233

Guo, Y.-Q., Yuan, Q., Liu, C., & Li, A.-F. 2013, Journal of Physics G Nuclear Physics, 40, 065201

Gursky, H., Gorenstein, P., & Giacconi, R. 1967, ApJ, 150, L75

Habibi, M., Stolte, A., & Harfst, S. 2014, A&A, 566, A6

Haggard, D., Nynka, M., Mon, B., et al. 2019, ApJ, 886, 96

Hailey, C. J., Mori, K., Bauer, F. E., et al. 2018, Nature, 556, 70

Hailey, C. J., Mori, K., Perez, K., et al. 2016, ApJ, 826, 160

Harrison, F. A., Craig, W. W., Christensen, F. E., et al. 2013, ApJ, 770, 103

Hartman, R. C., Bertsch, D. L., Bloom, S. D., et al. 1999, ApJS, 123, 79

Haymes, R. C., Ellis, D. V., Fishman, G. J., Glenn, S. W., & Kurfess, J. D. 1969, ApJ, 157, 1455

Haymes, R. C., Walraven, G. D., Meegan, C. A., et al. 1975, ApJ, 201, 593

Heard, V. & Warwick, R. S. 2013a, MNRAS, 428, 3462

Heard, V. & Warwick, R. S. 2013b, MNRAS, 434, 1339

Helfand, D. J. & Becker, R. H. 1987, ApJ, 314, 203

Henshaw, J. D., Barnes, A. T., Battersby, C., et al. 2023, in Astronomical Society of the Pacific Conference Series, Vol. 534, Protostars and Planets VII, ed. S. Inutsuka, Y. Aikawa, T. Muto, K. Tomida, & M. Tamura, 83

H.E.S.S. Collaboration, Abdalla, H., Abramowski, A., et al. 2018a, A&A, 612, A9

H.E.S.S. Collaboration, Abdalla, H., Abramowski, A., et al. 2018b, A&A, 612, A1

H.E.S.S. Collaboration, Abdalla, H., Aharonian, F., et al. 2018c, A&A, 620, A66

H.E.S.S. Collaboration, Abramowski, A., Aharonian, F., et al. 2016, Nature, 531, 476

Heywood, I., Camilo, F., Cotton, W. D., et al. 2019, Nature, 573, 235

Heywood, I., Rammala, I., Camilo, F., et al. 2022, ApJ, 925, 165

Hinton, J. A. & Aharonian, F. A. 2007, ApJ, 657, 302

Ho, L. C. 2008, ARA&A, 46, 475

Hong, J. 2012, MNRAS, 427, 1633

Hong, J., Mori, K., Hailey, C. J., et al. 2016, ApJ, 825, 132

Hong, J. S., van den Berg, M., Grindlay, J. E., & Laycock, S. 2009, ApJ, 706, 223

Hooper, D. & Slatyer, T. R. 2013, Physics of the Dark Universe, 2, 118

Hosek, Jr., M. W., Lu, J. R., Anderson, J., et al. 2019, ApJ, 870, 44

Hußmann, B., Stolte, A., Brandner, W., Gennaro, M., & Liermann, A. 2012, A&A, 540, A57

Indriolo, N., Neufeld, D. A., Gerin, M., et al. 2015, ApJ, 800, 40

Inui, T., Koyama, K., Matsumoto, H., & Tsuru, T. G. 2009, PASJ, 61, S241

Ilev, A. V., Dogiel, V. A., Chernyshov, D. O., et al. 2018, ApJ, 855, 23

Jansen, F., Lumb, D., Altieri, B., et al. 2001, A&A, 365, L1

Jean, P., Guessoum, N., & Ferrière, K. 2017, in IAU Symposium, Vol. 322, The Multi-Messenger Astrophysics of the Galactic Centre, ed. R. M. Crocker, S. N. Longmore, & G. V. Bicknell, 172–175

Jiao, Y., Hammer, F., Wang, H., et al. 2023, A&A, 678, A208

Johnson, S. P., Dong, H., & Wang, Q. D. 2009, MNRAS, 399, 1429

Johnson, III, W. N., Harnden, Jr., F. R., & Haymes, R. C. 1972, ApJ, 172, L1

Johnston, S., Kramer, M., Lorimer, D. R., et al. 2006, MNRAS, 373, L6

Jouvin, L., Lemièvre, A., & Terrier, R. 2017, MNRAS, 467,

4622

Jouvin, L., Lemière, A., & Terrier, R. 2020, *A&A*, 644, A113

Kaneda, H., Makishima, K., Yamauchi, S., et al. 1997, *ApJ*, 491, 638

Kargaltsev, O., Pavlov, G. G., Klingler, N., & Rangelov, B. 2017, *Journal of Plasma Physics*, 83, 635830501

Karwin, C. M., Murgia, S., Campbell, S., & Moskalenko, I. V. 2019, *ApJ*, 880, 95

Kellogg, E., Gursky, H., Murray, S., Tananbaum, H., & Giacconi, R. 1971, *ApJ*, 169, L99

Kennea, J. A., Burrows, D. N., Kouveliotou, C., et al. 2013, *ApJ*, 770, L24

Khabibullin, I., Churazov, E., & Sunyaev, R. 2020, *MNRAS*, 498, 4379

Khabibullin, I., Churazov, E., & Sunyaev, R. 2022, *MNRAS*, 509, 6068

Khokhlov, A. & Melia, F. 1996, *ApJ*, 457, L61

Kierans, C. A., Boggs, S. E., Zoglauer, A., et al. 2020, *ApJ*, 895, 44

Kistler, M. D. 2015, arXiv e-prints, arXiv:1511.01159

Knöldlseder, J., Jean, P., Lonjou, V., et al. 2005, *A&A*, 441, 513

Kormendy, J. & Ho, L. C. 2013, *ARA&A*, 51, 511

Kosack, K., Badran, H. M., Bond, I. H., et al. 2004, *ApJ*, 608, L97

Koyama, K. 2018, *PASJ*, 70, R1

Koyama, K., Awaki, H., Kunieda, H., Takano, S., & Tawara, Y. 1989, *Nature*, 339, 603

Koyama, K., Hyodo, Y., Inui, T., et al. 2007a, *PASJ*, 59, 245

Koyama, K., Maeda, Y., Sonobe, T., et al. 1996, *PASJ*, 48, 249

Koyama, K., Takikawa, Y., Hyodo, Y., et al. 2009, *PASJ*, 61, S255

Koyama, K., Uchiyama, H., Hyodo, Y., et al. 2007b, *PASJ*, 59, 237

Krivonos, R., Clavel, M., Hong, J., et al. 2017, *MNRAS*, 468, 2822

Krivonos, R., Revnivtsev, M., Churazov, E., et al. 2007, *A&A*, 463, 957

Krivonos, R. A., Tomsick, J. A., Bauer, F. E., et al. 2014, *ApJ*, 781, 107

Krujissen, J. M. D., Dale, J. E., & Longmore, S. N. 2015, *MNRAS*, 447, 1059

Kuznetsova, E., Krivonos, R., Clavel, M., et al. 2019, *MNRAS*, 484, 1627

Kuznetsova, E., Krivonos, R., Lutovinov, A., & Clavel, M. 2022, *MNRAS*, 509, 1605

Law, C. & Yusef-Zadeh, F. 2004, *ApJ*, 611, 858

Law, C. J. 2010, *ApJ*, 708, 474

Le Petit, F., Ruaud, M., Bron, E., et al. 2016, *A&A*, 585, A105

Lee, S. K., Lisanti, M., Safdi, B. R., Slatyer, T. R., & Xue, W. 2016, *Phys. Rev. Lett.*, 116, 051103

Leventhal, M., MacCallum, C. J., & Stang, P. D. 1978, *ApJ*, 225, L11

Levine, D., Morris, M., & Figer, D. 1999, in *ESA Special Publication*, Vol. 427, *The Universe as Seen by ISO*, ed. P. Cox & M. Kessler, 699

Lhaaso Collaboration. 2024, *Science Bulletin*, 69, 449

Linden, T., Lovegrove, E., & Profumo, S. 2012, *ApJ*, 753, 41

Lindsay, C. M. & McCall, B. J. 2001, *Journal of Molecular Spectroscopy*, 210, 60

Lingenfelter, R. E. & Ramaty, R. 1989, *ApJ*, 343, 686

Lipman, D., Battersby, C., Walker, D. L., et al. 2025, *ApJ*, 984, 159

List, F., Rodd, N. L., & Lewis, G. F. 2021, *Phys. Rev. D*, 104, 123022

Liu, B. & Yang, R. 2024, *Phys. Rev. D*, 110, 063033

Liu, S. & Melia, F. 2002, *ApJ*, 566, L77

Liu, S., Melia, F., Petrosian, V., & Fatuzzo, M. 2006, *ApJ*, 647, 1099

Lower, M. E., Dai, S., Johnston, S., & Barr, E. D. 2024, *ApJ*, 967, L16

Lu, F. J., Wang, Q. D., & Lang, C. C. 2003, *AJ*, 126, 319

Lu, F. J., Yuan, T. T., & Lou, Y.-Q. 2008, *ApJ*, 673, 915

Lynden-Bell, D. & Rees, M. J. 1971, *MNRAS*, 152, 461

Macias, O., Gordon, C., Crocker, R. M., et al. 2018, *Nature Astronomy*, 2, 387

Macias, O., Gordon, C., Crocker, R. M., & Profumo, S. 2015, *MNRAS*, 451, 1833

Mackey, S. C., Morris, M. R., Ponti, G., Anastasopoulou, K., & Mondal, S. 2024, *ApJ*, 966, L32

Maeda, Y., Baganoff, F. K., Feigelson, E. D., et al. 2002, *ApJ*, 570, 671

MAGIC Collaboration, Acciari, V. A., Ansoldi, S., et al. 2020, *A&A*, 642, A190

Malyshev, D., Chernyakova, M., Neronov, A., & Walter, R. 2015, *A&A*, 582, A11

Manchester, R. N., Hobbs, G. B., Teoh, A., & Hobbs, M. 2005, *AJ*, 129, 1993

Marchesi, S., Eagle, J., Ajello, M., et al. 2024, *ApJ*, 964, 132

Marin, F., Churazov, E., Khabibullin, I., et al. 2023, *Nature*, 619, 41

Markoff, S. 2010, *Proceedings of the National Academy of Science*, 107, 7196

Markoff, S., Falcke, H., Yuan, F., & Biermann, P. L. 2001, *A&A*, 379, L13

Marrone, D. P., Baganoff, F. K., Morris, M. R., et al. 2008, *ApJ*, 682, 373

Marrone, D. P., Moran, J. M., Zhao, J.-H., & Rao, R. 2007, *ApJ*, 654, L57

Mauerhan, J. C., Munoz, M. P., Morris, M. R., Stolovy, S. R., & Cotera, A. 2010, *ApJ*, 710, 706

Mayer-Hasselwander, H. A., Bertsch, D. L., Dingus, B. L., et al. 1998, *A&A*, 335, 161

McCall, B. J., Huneycutt, A. J., Saykally, R. J., et al. 2003, *Nature*, 422, 500

McDermott, S. D., Zhong, Y.-M., & Cholis, I. 2023, *MNRAS*, 522, L21

McKee, C. F. 1989, *ApJ*, 345, 782

Melia, F. & Falcke, H. 2001, *ARA&A*, 39, 309

Melia, F., Fatuzzo, M., Yusef-Zadeh, F., & Markoff, S. 1998, *ApJ*, 508, L65

Mereghetti, S., Pons, J. A., & Melatos, A. 2015, *Space Sci. Rev.*, 191, 315

Mereghetti, S., Sidoli, L., & Israel, G. L. 1998, *A&A*, 331, L77

Merritt, D. 2010, *ApJ*, 718, 739

Michail, J. M., Yusef-Zadeh, F., Wardle, M., et al. 2024, *ApJ*, 971, 52

Miller, S., Tennyson, J., Geballe, T. R., & Stallard, T. 2020, *Reviews of Modern Physics*, 92, 035003

Mirabel, I. F., Rodriguez, L. F., Cordier, B., Paul, J., & Lebrun, F. 1992, *Nature*, 358, 215

Mitsuda, K., Bautz, M., Inoue, H., et al. 2007, *PASJ*, 59, S1

Molinari, S., Bally, J., Noriega-Crespo, A., et al. 2011, *ApJ*, 735, L33

Mori, H., Hyodo, Y., Tsuru, T. G., Nobukawa, M., & Koyama,

K. 2009, PASJ, 61, 687

Mori, K., Gotthelf, E. V., Zhang, S., et al. 2013, ApJ, 770, L23

Mori, K., Hailey, C. J., Krivonos, R., et al. 2015, ApJ, 814, 94

Mori, K., Hailey, C. J., Mandel, S., et al. 2019, ApJ, 885, 142

Mori, K., Hailey, C. J., Schutt, T. Y. E., et al. 2021, ApJ, 921, 148

Morlino, G. & Gabici, S. 2015, MNRAS, 451, L100

Morris, M. 2022, in Active Galactic Nuclei, ed. F. Combes, 65–100

Morris, M., Baganoff, F., Muno, M., et al. 2003, Astronomische Nachrichten Supplement, 324, 167

Morris, M. & Serabyn, E. 1996, ARA&A, 34, 645

Morris, M. R. 2015, in Lessons from the Local Group: A Conference in honor of David Block and Bruce Elmegreen, ed. K. Freeman, B. Elmegreen, D. Block, & M. Woolway, 391

Moskalenko, I. V., Porter, T. A., & Strong, A. W. 2006, ApJ, 640, L155

Mossoux, E. & Grosso, N. 2017, A&A, 604, A85

Mukai, K. 2017, PASP, 129, 062001

Muno, M. P., Baganoff, F. K., Bautz, M. W., et al. 2003, ApJ, 599, 465

Muno, M. P., Baganoff, F. K., Bautz, M. W., et al. 2004, ApJ, 613, 326

Muno, M. P., Baganoff, F. K., Brandt, W. N., Morris, M. R., & Starck, J.-L. 2008, ApJ, 673, 251

Muno, M. P., Bauer, F. E., Baganoff, F. K., et al. 2009, ApJS, 181, 110

Muno, M. P., Bauer, F. E., Bandyopadhyay, R. M., & Wang, Q. D. 2006, ApJS, 165, 173

Muno, M. P., Lu, J. R., Baganoff, F. K., et al. 2005a, ApJ, 633, 228

Muno, M. P., Pfahl, E., Baganoff, F. K., et al. 2005b, ApJ, 622, L113

Murakami, H., Koyama, K., & Maeda, Y. 2001a, ApJ, 558, 687

Murakami, H., Koyama, K., Sakano, M., Tsujimoto, M., & Maeda, Y. 2000, ApJ, 534, 283

Murakami, H., Koyama, K., Tsujimoto, M., Maeda, Y., & Sakano, M. 2001b, ApJ, 550, 297

Murchikova, E. M., Phinney, E. S., Pancoast, A., & Blandford, R. D. 2019, Nature, 570, 83

Murgia, S. 2020, Annual Review of Nuclear and Particle Science, 70, 455

Nakashima, S., Koyama, K., Wang, Q. D., & Enokiya, R. 2019, ApJ, 875, 32

Nakashima, S., Nobukawa, M., Uchida, H., et al. 2013, ApJ, 773, 20

Narayan, R. & Quataert, E. 2023, Nature, 615, 597

Narayan, R. & Raymond, J. 1999, ApJ, 515, L69

Narayan, R., Yi, I., & Mahadevan, R. 1995, Nature, 374, 623

Nayakshin, S. & Sunyaev, R. 2005, MNRAS, 364, L23

Neilson, J., Markoff, S., Nowak, M. A., et al. 2015, ApJ, 799, 199

Neilson, J., Nowak, M. A., Gammie, C., et al. 2013, ApJ, 774, 42

Nishiyama, S., Yasui, K., Nagata, T., et al. 2013, ApJ, 769, L28

Nobukawa, M., Koyama, K., Tsuru, T. G., Ryu, S. G., & Tatischeff, V. 2010, PASJ, 62, 423

Nobukawa, M., Ryu, S. G., Tsuru, T. G., & Koyama, K. 2011, ApJ, 739, L52

Nobukawa, M., Uchiyama, H., Nobukawa, K. K., Yamauchi, S., & Koyama, K. 2016, ApJ, 833, 268

Nowak, M. A., Neilsen, J., Markoff, S. B., et al. 2012, ApJ, 759, 95

Nynka, M., Hailey, C. J., Mori, K., et al. 2013, ApJ, 778, L31

Nynka, M., Hailey, C. J., Zhang, S., et al. 2015, ApJ, 800, 119

Odaka, H., Aharonian, F., Watanabe, S., et al. 2011, ApJ, 740, 103

Oka, T. 2006, Proceedings of the National Academy of Science, 103, 12235

Oka, T., Geballe, T. R., Goto, M., et al. 2019, ApJ, 883, 54

Oka, T., Geballe, T. R., Goto, M., Usuda, T., & McCall, B. J. 2005, ApJ, 632, 882

Ono, A., Uchiyama, H., Yamauchi, S., et al. 2019, PASJ, 71, 52

Padovani, M., Ivlev, A. V., Galli, D., et al. 2020, Space Sci. Rev., 216, 29

Paré, D. M., Chuss, D. T., Karpovich, K., et al. 2025, ApJ, 978, 28

Park, S., Muno, M. P., Baganoff, F. K., et al. 2005, ApJ, 631, 964

Paumard, T., Genzel, R., Martins, F., et al. 2006, ApJ, 643, 1011

Pavlinsky, M. N., Grebenev, S. A., & Sunyaev, R. A. 1994, ApJ, 425, 110

Peille, P., Barret, D., Cucchietti, E., et al. 2025, Experimental Astronomy, 59, 18

Perez, K., Hailey, C. J., Bauer, F. E., et al. 2015, Nature, 520, 646

Perez, K., Krivonos, R., & Wik, D. R. 2019, ApJ, 884, 153

Petropoulou, M., Ponti, G., Stel, G., & Mastichiadis, A. 2024, A&A, 691, A314

Pfahl, E. & Loeb, A. 2004, ApJ, 615, 253

Phan, V. H. M., Morlino, G., & Gabici, S. 2018, MNRAS, 480, 5167

Pohl, M. 2005, ApJ, 626, 174

Ponti, G., De Marco, B., Morris, M. R., et al. 2015a, MNRAS, 454, 1525

Ponti, G., George, E., Scaringi, S., et al. 2017, MNRAS, 468, 2447

Ponti, G., Hofmann, F., Churazov, E., et al. 2019, Nature, 567, 347

Ponti, G., Morris, M. R., Churazov, E., Heywood, I., & Fender, R. P. 2021, A&A, 646, A66

Ponti, G., Morris, M. R., Terrier, R., et al. 2015b, MNRAS, 453, 172

Ponti, G., Terrier, R., Goldwurm, A., Belanger, G., & Trap, G. 2010, ApJ, 714, 732

Porquet, D., Decourchelle, A., & Warwick, R. S. 2003a, A&A, 401, 197

Porquet, D., Predehl, P., Aschenbach, B., et al. 2003b, A&A, 407, L17

Possenti, A., Cerutti, R., Colpi, M., & Mereghetti, S. 2002, A&A, 387, 993

Pothast, M., Gaggero, D., Storm, E., & Weniger, C. 2018, J. Cosmology Astropart. Phys., 2018, 045

Prantzos, N., Boehm, C., Bykov, A. M., et al. 2011, Reviews of Modern Physics, 83, 1001

Predehl, P., Andritschke, R., Arefiev, V., et al. 2021, A&A, 647, A1

Predehl, P., Sunyaev, R. A., Becker, W., et al. 2020, Nature, 588, 227

Predehl, P. & Truemper, J. 1994, A&A, 290, L29

Proctor, R. J., Skinner, G. K., & Willmore, A. P. 1978, MNRAS, 185, 745

Purcell, W. R., Cheng, L.-X., Dixon, D. D., et al. 1997, ApJ, 491, 725

Quataert, E. 2002, ApJ, 575, 855

Ramaty, R., Kozlovsky, B., & Lingenfelter, R. E. 1979, ApJS, 40, 487

Rauw, G. & Nazé, Y. 2016, Advances in Space Research, 58, 761

Ravikularaman, S., Recchia, S., Phan, V. H. M., & Gabici, S. 2025, A&A, 694, A114

Rea, N., Coti Zelati, F., Viganò, D., et al. 2020, ApJ, 894, 159

Rea, N., Esposito, P., Pons, J. A., et al. 2013, ApJ, 775, L34

Recchia, S., Gabici, S., Aharonian, F. A., & Niro, V. 2021, ApJ, 914, 135

Recchia, S., Phan, V. H. M., Biswas, S., & Gabici, S. 2019, MNRAS, 485, 2276

Reid, M. J. & Brunthaler, A. 2020, ApJ, 892, 39

Reis, R. C., Wheatley, P. J., Gänsicke, B. T., & Osborne, J. P. 2013, MNRAS, 430, 1994

Ressler, S. M., Quataert, E., & Stone, J. M. 2018, MNRAS, 478, 3544

Ressler, S. M., White, C. J., Quataert, E., & Stone, J. M. 2020, ApJ, 896, L6

Revnivtsev, M., Molkov, S., & Sazonov, S. 2006, MNRAS, 373, L11

Revnivtsev, M., Sazonov, S., Churazov, E., et al. 2009, Nature, 458, 1142

Revnivtsev, M. G., Churazov, E. M., Sazonov, S. Y., et al. 2004, A&A, 425, L49

Riegler, G. R., Ling, J. C., Mahoney, W. A., et al. 1981, ApJ, 248, L13

Rockefeller, G., Fryer, C. L., Baganoff, F. K., & Melia, F. 2005, ApJ, 635, L141

Rockefeller, G., Fryer, C. L., Melia, F., & Warren, M. S. 2004, ApJ, 604, 662

Rodríguez-Fernández, N. J., Martín-Pintado, J., & de Vicente, P. 2001, A&A, 377, 631

Rodríguez-Ramírez, J. C., de Gouveia Dal Pino, E. M., & Alves Batista, R. 2019, ApJ, 879, 6

Rogers, F., Zhang, S., Perez, K., Clavel, M., & Taylor, A. 2022, ApJ, 934, 19

Russell, C. M. P., Wang, Q. D., & Cuadra, J. 2017, MNRAS, 464, 4958

Ryu, S. G., Koyama, K., Nobukawa, M., Fukuoka, R., & Tsuru, T. G. 2009, PASJ, 61, 751

Ryu, S. G., Nobukawa, M., Nakashima, S., et al. 2013, PASJ, 65, 33

Sacchi, A. & Lodato, G. 2019, MNRAS, 486, 1833

Sakano, M., Warwick, R. S., & Decourchelle, A. 2003, in Workshop on Galaxies and Clusters of Galaxies, 9

Sakano, M., Warwick, R. S., Decourchelle, A., & Predehl, P. 2004, MNRAS, 350, 129

Sanna, A., Riggio, A., Burderi, L., et al. 2017, MNRAS, 469, 2

Sarkar, K. C. 2024, A&A Rev., 32, 1

Sazonov, S., Paizis, A., Bazzano, A., et al. 2020, New A Rev., 88, 101536

Sazonov, S., Sunyaev, R., & Revnivtsev, M. 2012, MNRAS, 420, 388

Scherer, A. & Cuadra, J. 2024, A&A, 690, L14

Shakura, N. I. & Sunyaev, R. A. 1973, A&A, 24, 337

Shannon, R. M. & Johnston, S. 2013, MNRAS, 435, L29

Sidoli, L. & Mereghetti, S. 1999, A&A, 349, L49

Sidoli, L., Mereghetti, S., Israel, G. L., & Bocchino, F. 2000, A&A, 361, 719

Sieger, T. 2023, Ap&SS, 368, 27

Sieger, T., Diehl, R., Khachatryan, G., et al. 2016, A&A, 586, A84

Sieger, T., Horan, D., & Kanbach, G. 2022, in Handbook of X-ray and Gamma-ray Astrophysics, ed. C. Bambi & A. Sangangelo, 80

Simpson, J. P., Colgan, S. W. J., Cotera, A. S., et al. 2007, ApJ, 670, 1115

Skilling, J. & Strong, A. W. 1976, A&A, 53, 253

Skinner, G. K., Willmore, A. P., Eyles, C. J., Bertram, D., & Church, M. J. 1987, Nature, 330, 544

Snow, T. P. & McCall, B. J. 2006, ARA&A, 44, 367

Sofue, Y. 1995, PASJ, 47, 551

Sofue, Y. & Handa, T. 1984, Nature, 310, 568

Sofue, Y., Oka, T., Longmore, S. N., et al. 2025, PASJ, 77, 687

Solanki, S., Ressler, S. M., Murchikova, L., Stone, J. M., & Morris, M. R. 2023, ApJ, 953, 22

Spitler, L. G., Lee, K. J., Eatough, R. P., et al. 2014, ApJ, 780, L3

Stel, G., Ponti, G., Haardt, F., & Sormani, M. 2025, A&A, 695, A52

Strong, A. W., Porter, T. A., Digel, S. W., et al. 2010, ApJ, 722, L58

Su, M., Slatyer, T. R., & Finkbeiner, D. P. 2010, ApJ, 724, 1044

Su, Y., Zhang, S., Sun, Y., et al. 2024, ApJ, 971, L6

Sunyaev, R. & Churazov, E. 1998, MNRAS, 297, 1279

Sunyaev, R. A., Markevitch, M., & Pavlinsky, M. 1993, ApJ, 407, 606

Suzuki, H., Bamba, A., Enokiya, R., et al. 2020, ApJ, 893, 147

Tashiro, M., Maejima, H., Toda, K., et al. 2021, in Society of Photo-Optical Instrumentation Engineers (SPIE) Conference Series, Vol. 11444, Society of Photo-Optical Instrumentation Engineers (SPIE) Conference Series, ed. J.-W. A. den Herder, S. Nikzad, & K. Nakazawa, 1144422

Tatischeff, V., Decourchelle, A., & Maurin, G. 2012, A&A, 546, A88

Terrier, R., Clavel, M., Soldi, S., et al. 2018, A&A, 612, A102

Terrier, R., Ponti, G., Bélanger, G., et al. 2010, ApJ, 719, 143

Tielens, A. G. G. M. 2013, Reviews of Modern Physics, 85, 1021

Tomsick, J., Boggs, S., Zoglauer, A., et al. 2024, in 38th International Cosmic Ray Conference, 745

Totani, T. 2006, PASJ, 58, 965

Trap, G., Goldwurm, A., Dodds-Eden, K., et al. 2011, A&A, 528, A140

Trap, G., Goldwurm, A., Terrier, R., et al. 2010, Advances in Space Research, 45, 507

Tsuboi, M., Handa, T., & Ukita, N. 1999, ApJS, 120, 1

Tsuboi, M., Tsutsumi, T., Kitamura, Y., et al. 2020, PASJ, 72, L10

Tsuchiya, K., Enomoto, R., Ksenofontov, L. T., et al. 2004, ApJ, 606, L115

Tsujimoto, M., Hyodo, Y., & Koyama, K. 2007, PASJ, 59, 229

Tsuru, T. G., Nobukawa, M., Nakajima, H., et al. 2009, PASJ, 61, S219

Uchiyama, H., Nobukawa, M., Tsuru, T. G., & Koyama, K. 2013, PASJ, 65, 19

Uchiyama, H., Nobukawa, M., Tsuru, T. G., Koyama, K., & Matsumoto, H. 2011, PASJ, 63, S903

van der Laan, H. 1966, Nature, 211, 1131

van der Tak, F. F. S., Belloche, A., Schilke, P., et al. 2006, A&A, 454, L99

Viana, A. & Moulin, E. 2013, in International Cosmic Ray Conference, Vol. 33, International Cosmic Ray Conference, 995

Viana, A., Ventura, S., Gaggero, D., et al. 2019, in International Cosmic Ray Conference, Vol. 36, 36th International Cosmic Ray Conference (ICRC2019), 817

von Fellenberg, S. D., Roychowdhury, T., Michail, J. M., et al. 2025, ApJ, 979, L20

Walker, D. L., Battersby, C., Lipman, D., et al. 2025, ApJ, 984, 158

Walls, M., Chernyakova, M., Terrier, R., & Goldwurm, A. 2016, MNRAS, 463, 2893

Wang, Q. D. 2021, MNRAS, 504, 1609

Wang, Q. D., Dong, H., & Lang, C. 2006a, MNRAS, 371, 38

Wang, Q. D., Gotthelf, E. V., & Lang, C. C. 2002a, Nature, 415, 148

Wang, Q. D., Lu, F., & Lang, C. C. 2002b, ApJ, 581, 1148

Wang, Q. D., Lu, F. J., & Gotthelf, E. V. 2006b, MNRAS, 367, 937

Wang, Q. D., Nowak, M. A., Markoff, S. B., et al. 2013, Science, 341, 981

Warwick, R. S., Turner, M. J. L., Watson, M. G., & Willingale, R. 1985, Nature, 317, 218

Watson, M. G., Willingale, R., Grindlay, J. E., & Hertz, P. 1981, ApJ, 250, 142

Weisskopf, M. C., Brinkman, B., Canizares, C., et al. 2002, PASP, 114, 1

Weisskopf, M. C., Soffitta, P., Baldini, L., et al. 2022, Journal of Astronomical Telescopes, Instruments, and Systems, 8, 026002

Weldon, G. C., Do, T., Witzel, G., et al. 2023, ApJ, 954, L33

Wharton, R. S., Chatterjee, S., Cordes, J. M., Deneva, J. S., & Lazio, T. J. W. 2012, ApJ, 753, 108

Wielgus, M., Moscibrodzka, M., Vos, J., et al. 2022, A&A, 665, L6

Winkler, C., Courvoisier, T. J.-L., Di Cocco, G., et al. 2003, A&A, 411, L1

Witzel, G., Martinez, G., Hora, J., et al. 2018, ApJ, 863, 15

Witzel, G., Martinez, G., Willner, S. P., et al. 2021, ApJ, 917, 73

Wommer, E., Melia, F., & Fatuzzo, M. 2008, MNRAS, 387, 987

Wongphechauxsorn, J., Champion, D. J., Bailes, M., et al. 2024, MNRAS, 527, 3208

Worrall, D. M., Marshall, F. E., Boldt, E. A., & Swank, J. H. 1982, ApJ, 255, 111

XRISM Collaboration, Audard, M., Awaki, H., et al. 2025, PASJ, 77, L1

Xu, X.-j., Li, Z., Zhu, Z., et al. 2019, ApJ, 882, 164

Xu, X.-j., Wang, Q. D., & Li, X.-D. 2016, ApJ, 818, 136

Xu, Y.-D., Narayan, R., Quataert, E., Yuan, F., & Baganoff, F. K. 2006, ApJ, 640, 319

Yalinewich, A., Piran, T., & Sari, R. 2017, ApJ, 838, 12

Yamauchi, S., Ebisawa, K., Tanaka, Y., et al. 2009, PASJ, 61, S225

Yamauchi, S., Kaneda, H., Koyama, K., et al. 1996, PASJ, 48, L15

Yamauchi, S., Nobukawa, K. K., Nobukawa, M., Uchiyama, H., & Koyama, K. 2016, PASJ, 68, 59

Yamauchi, S., Shimizu, M., Nobukawa, M., et al. 2018, PASJ, 70, 82

Yan, Q.-Z., Walsh, A. J., Dawson, J. R., et al. 2017, MNRAS, 471, 2523

Yang, R., Aharonian, F., & Evoli, C. 2016, Phys. Rev. D, 93, 123007

Yao, J. M., Manchester, R. N., & Wang, N. 2017, ApJ, 835, 29

Yasui, K., Nishiyama, S., Yoshikawa, T., et al. 2015, PASJ, 67, 123

Yoast-Hull, T. M., Gallagher, III, J. S., & Zweibel, E. G. 2014, ApJ, 790, 86

Yu, Y.-W., Cheng, K. S., Chernyshov, D. O., & Dogiel, V. A. 2011, MNRAS, 411, 2002

Yuan, F., Markoff, S., & Falcke, H. 2002, A&A, 383, 854

Yuan, F. & Narayan, R. 2014, ARA&A, 52, 529

Yuan, F., Quataert, E., & Narayan, R. 2003, ApJ, 598, 301

Yuan, Q. & Wang, Q. D. 2016, MNRAS, 456, 1438

Yuasa, T., Makishima, K., & Nakazawa, K. 2012, ApJ, 753, 129

Yusef-Zadeh, F., Arendt, R. G., Wardle, M., & Heywood, I. 2023, ApJ, 949, L31

Yusef-Zadeh, F., Arendt, R. G., Wardle, M., et al. 2022, ApJ, 925, L18

Yusef-Zadeh, F., Bushouse, H., Dowell, C. D., et al. 2006, ApJ, 644, 198

Yusef-Zadeh, F., Hewitt, J. W., Wardle, M., et al. 2013, ApJ, 762, 33

Yusef-Zadeh, F., Law, C., & Wardle, M. 2002a, ApJ, 568, L121

Yusef-Zadeh, F., Law, C., Wardle, M., et al. 2002b, ApJ, 570, 665

Yusef-Zadeh, F., Munoz, M., Wardle, M., & Lis, D. C. 2007, ApJ, 656, 847

Yusef-Zadeh, F., Wardle, M., Dodds-Eden, K., et al. 2012, AJ, 144, 1

Zhang, M., Li, Z., Hua, Z., & Morris, M. R. 2023, MNRAS, 522, 3568

Zhang, M., Li, Z., & Morris, M. R. 2021, ApJ, 913, 68

Zhang, S., Baganoff, F. K., Ponti, G., et al. 2017, ApJ, 843, 96

Zhang, S., Hailey, C. J., Baganoff, F. K., et al. 2014, ApJ, 784, 6

Zhang, S., Hailey, C. J., Mori, K., et al. 2015, ApJ, 815, 132

Zhang, S., Zhu, Z., Li, H., et al. 2020, ApJ, 893, 3

Zhang, Y., Comparat, J., Ponti, G., et al. 2024, A&A, 690, A267

Zhao, J.-H., Morris, M. R., & Goss, W. M. 2016, ApJ, 817, 171

Zhou, P., Leung, S.-C., Li, Z., et al. 2021, ApJ, 908, 31

Zhu, Z., Li, Z., & Morris, M. R. 2018, ApJS, 235, 26

Zhu, Z., Li, Z., Morris, M. R., Zhang, S., & Liu, S. 2019, ApJ, 875, 44

Zorotovic, M., Schreiber, M. R., & Gänsicke, B. T. 2011, A&A, 536, A42

Zubovas, K., Nayakshin, S., & Markoff, S. 2012, MNRAS, 421, 1315